DOCTORAL (PhD) DISSERTATION

MWCNTS BASED NANOCOMPOSITES FOR THE REMOVAL OF HYDROCARBONS AND ORGANIC DYES FROM WATER

Compiled within the framework of the
University of Pannonia
Doctoral School of Chemical Engineering and Material Sciences

DOI:10.18136/PE.2022.816

Written by:
Thamer Adnan Abdullah
MSc in Chemical Engineering

Supervisor:
Dr. habil. Tatjána Juzsakova
Associate professor

Sustainability Solutions Research Lab
Research Centre for Biochemical, Environmental and Chemical Engineering
Faculty of Engineering
University of Pannonia

Veszprém, Hungary
2022

MWCNTs Based Nanocomposites for the Removal of Hydrocarbons and Organic dyes from Water

Thesis for obtaining a PhD degree in the Doktoral School of Chemical Engineering and Material Science of the University of Pannonia

in the branch of Bio, Environmental and Chemical Engineering Sciences

Written by Thamer Adnan Abdullah

Supervisor(s): Tatjána Juzsakova

propose acceptance (yes / no) …….
(supervisor/s)

As reviewer, I propose acceptance of the thesis:

Name of Reviewer: …..... …..... yes / no
……
(reviewer)

Name of Reviewer: …..... …..... yes / no
……
(reviewer)

The PhD-candidate has achieved ….....% at the public discussion.

Veszprém

…….
(Chairman of the Committee)

The grade of the PhD Diploma …..... (…….. %)

Veszprém

……
(Chairman of UDHC)

ABSTRACT

The application of solid adsorbents for the removal of hydrocarbons and dyes from water has gained attention in recent years. This is due to the potential of this technology to minimize the detrimental impact of water pollution. However, this requires the development of novel solid adsorbent materials that can achieve significant selectivity, have a large adsorption capacity as well as offer fast adsorption coupled with excellent mechanical strength and the ability to regenerate.

In this work, the application of metal oxides and multi-walled carbon nanotubes (MWCNTs) based on metal oxides and/or polymer nanocomposites as adsorbents for the removal of hydrocarbons and dyes from water was investigated.

Thermal pre-treatment was used to produce V_2O_5 nanoparticle adsorbents by increasing the temperature to between 90 and 750°C. Functionalized MWCNTs were obtained by chemical oxidation using concentrated sulfuric and nitric acids. TiO_2, V_2O_5, CeO_2, V_2O_5:CeO_2 and V_2O_5:CeO_2:TiO_2 nanocomposites were prepared using hydrothermal synthesis method followed by the deposition of these oxides over MWCNTs. The polymer-modified (polyethylene (PE), polystyrene (PS) or poly-n-isopropylacrylamide-co-butylacrylate (PNIPAM)) magnetite/MWCNTs were prepared using a solution mixing method.

Fresh MWCNTs, individual and mixed metal oxides, metal oxide nanoparticle-doped MWCNTs and polymer-modified Fe/MWCNTs using different analytical techniques were characterized. XRD, TEM, SEM-EDX, AFM, FTIR, Raman, TG/DTA and BET techniques were used to determine the structure as well as chemical and morphological properties of the newly prepared adsorbents. The removal efficiencies of hydrocarbons and dyes over fresh and modified MWCNT adsorbents were examined by using GC, UV-Vis and HPLC techniques. Hydrocarbons such as kerosene, toluene and methylene blue (MB) dye were used as model compounds for adsorption tests.

Fresh, oxidized and metal oxide-doped MWCNTs as well as PE- and PNIPAM-modified Fe/MWCNTs were applied for the removal of kerosene and MB from a model solution of water. Fresh, oxidized iron oxide doped MWCNTs as well as PS-modified Fe/MWCNTs were applied for the removal of toluene from water.

The results illustrated that V_2O_5 annealing at 500°C as well as the modification of MWCNTs with V_2O_5:CeO_2 and polymers enhanced the adsorption properties of carbon nanotubes.

To analyse the kinetic data of adsorption experiments pseudo first and second order equations and rate equations for intera-particle diffusion were used. The isotherm obtained for equilibrium was analyzed by Freundlich and Langmuir isotherm models.

Keywords: V_2O_5 nanoparticles; metal oxide-doped MWCNTs; polymer-modified Fe_3O_4/MWCNTs; nanoadsorbents; hydrocarbons and methylene blue removal from water

الملخص

زاد الاهتمام في السنوات الأخيرة باستخدام الممتزات الصلبة لإزالة الهيدروكربونات والأصباغ من الماء. ويرجع ذلك إلى قدرتها على تقليل التأثير الضار لتلوث المياه. ومع ذلك ، فإن هذا يتطلب الى تطوير مواد ماصة صلبة جديدة يمكنها ان تحقيق انتقائية كبيرة ولديها قدرة امتصاص كبيرة بالإضافة إلى امكانية لامتصاص السريع المقترن بقوة ميكانيكية ممتازة وقدرتها على التجديد. في هذا العمل، تم دراسة استخدام أكاسيد المعادن والأنابيب الكربون النانوية متعددة الجدران (MWCNTs) باعتبار ان أكاسيد المعادن و/ أو المركبات البوليمرية النانوية هي مواد ماصة لإزالة الهيدروكربونات والأصباغ من الماء.

تم استخدام الطريقة الحرارية (التصعيد) لإنتاج المادة الاولية الماصة من جزيئات خماسي أوكسيد الفناديوم متناهية الصغر باعتبارها مواد مازة وتحضير نماذج منه مسخنه بدرجات حرارية مابين 90 الى 750 درجة مئوية. والحصول على الكاربون نانو تيوب المؤكسد عن طريق الأكسدة الكيميائية باستخدام حامضي الكبريتيك والنتريك المركزين, ثم تحضير مركبات متناهية الصغرمن الاكاسيد (TiO_2 ,CeO_2) باستخدام الطريقة الحرارية/ المائية (autoclave) والمتراكبان (V_2O_5:CeO_2:TiO_2وV_2O_5:CeO_2) متبوعًا بترسيب الأكاسيد المحضرة ومتراكباتها فوق الكاربون نانو تيوب طريقة خلط المحاليل وتم تحضر (Fe_3O_4) المغناطيسي بطريقة التسحيح. تم تتشخسص الاكاسيد المحضرة والمتراكبات والكاربون نانو تيوب المؤكسد والكاربون نانو تيوب المشوب بألاكاسيد النانوية والكاربون نانو تيوب المشوب باوكسيد الحديد الممغنط مع البوليمر باستخدام تقنيات تحليلية مختلفة مثل تقنيات XRD و TEM و SEM و EDX و AFM و FTIR و Raman و TG / DTA و BET لتحديد البنية بالإضافة إلى الخصائص الكيميائية والمورفولوجية للمواد المازة المعدة حديثًا. تم فحص كفاءة إزالة الهيدروكربونات والأصباغ على ممتزات الكاربون نانو تيوب المحضرة والمشوبة باستخدام تقنيات GC و UV-Vis و HPLC. تم استخدام الهيدروكربونات مثل الكيروسين والتولوين وصبغة الميثيلين الزرقاء (MB) كمركبات نموذجية (ملوثات) لاختبارات الامتزاز.

تم اختبار الكاربون نانو تيوب الجاهز والمؤكسدة والمشوب بالاكاسيد المحضرة وكذلك المشوب باوكسيد الحديد المغناطيسي والبولي إيثيلين والبوليمر الطويل السلسلة المضافة على الكاربون نانو تيوب لإزالة الكيروسين و MB من محلول مائي نموذجي قياسي. تم استخدام الكاربون نانو تيوب الممغنط وكذلك البوليسترين المعدل لإزالة التولوين من الماء.

أوضحت النتائج أن التلدين V_2O_5 عند 500 درجة مئوية وكذلك تشويب الكاربون نانو تيوب مع V_2O_5: CeO_2 والبوليمرات عززت خصائص الامتزاز للأنابيب النانوية الكربونية. لتحليل البيانات الحركية لتجارب الامتزاز، تم استخدام معادلات الدرجة الأولى والثانية الكاذبة ومعادلات معدل الانتشار بين الجسيمات. تم التحليل بثبوت الحرارة الذي تم الحصول عليه للتوازن بواسطة نماذج لانكمور و فرندلويج -

الكلمات الدالة: الجسيمات النانوية V_2O_5 ؛ MWCNTs ممشوب بأكسيد نانوية؛ Fe_3O_4 / MWCNTs المشوب بالبوليمر ؛ مواد ماصة نانوية. الهيدروكربونات. إزالة الميثيلين الأزرق من الماء.

LIST OF CONTENT

List of Tables

List of Figures

LIST OF SYMBOLS

C_o	Concentrations of adsorbate at the initial time	mg/L
C_t	Concentrations of adsorbate at time t	mg/L
D_{av}	Average pore diameter	nm
k_1	Adsorption rate constant of the first-order model	1/min
k_2	Rate constant of second-order model	mg/g. min
k_p	Intraparticle diffusion rate constant	$mg/g.min^{0.5}$
q_{max}	Maximum amount of the pollutant per unit weight of sorbent	mg/g
b	Langmuir adsorption equilibrium constant	-
C_e	residual concentration of pollutant in solution	mg/L
K_f	Freundlich adsorption constant	mg/g
n	Frindluich adsorption intensity	-
m	Weight of the adsorbent	mg
R^2	Value of the liner regression	-
RE	Removal efficiency	%
q_e	Equilibrium adsorption capacity	g/g
q_t	Adsorption capacity at time t	g/g
V	Volume of solution	L
$S_{1.7-300}$	Pore volume having a diameter between 1.7 and 300 nm	cm^3/g
S_{BET}	Specific surface area	m^2/g
S_{micro}	Specific surface area of micropores (< 2 nm)	m^2/g
V_{micro}	Volume of micropores (< 2 nm)	cm^3/g
λ	Absorbance wavelength	nm

LIST OF ABBREVIATIONS AND ACRONYMS

AFM	Atomic force microscopy
MWCNTs	Multiwalled carbon nanotubes
BET	Brunauer-Emmett-Teller surface area determination method
BJH	Barret–Joyner–Halenda pore size distribution determination
Ce/MWCNTs	CeO_2 doped multiwalled carbon nanotubes
EDX	Energy dispersive X-ray elemental analysis
Fe/MWCNTs	Fe_3O_4 doped multiwalled carbon nanotubes
FTIR	Fourier transform infrared spectrometry
ox-MWCNTs	Oxidized multiwalled carbon nanotubes
PE:Fe/MWCNTs	Polyethylene-magnetite doped multiwalled carbon nanotubes
PS:Fe/MWCNTs	Polystyrene-magnetite doped multiwalled carbon nanotubes
P-NIPAM	Poly-n-isopropylacrylamide-co-butylacrylate
P-NIPAM:Fe/MWCNTs	Poly-n-isopropylacrylamide-co-butylacrylate and magnetite doped multiwalled carbon nanotubes
SEM	Scanning electron microscopy
Ti/MWCNTs	TiO_2 doped multiwalled carbon nanotubes
TGA	Thermogravimetric analysis
TEM	Transmission electron microscopy
V/MWCNTs	V_2O_5 doped multiwalled carbon nanotubes
V:Ti/MWCNTs	V_2O_5:TiO_2 doped multiwalled carbon nanotubes
V:Ce/MWCNTs	V_2O_5:CeO_2 doped multiwalled carbon nanotubes
V:Ce:Ti/MWCNTs	V_2O_5:CeO_2:TiO_2 doped multiwalled carbon nanotubes
V:Ce	V_2O_5 and CeO_2 mixed oxides
V:Ti	V_2O_5 and TiO_2 mixed oxides
V:Ce:Ti	V_2O_5, CeO_2 and TiO_2 mixed oxides

Acknowledgement

This work is carried out as a part of the research activities in Sustainability Solutions Research Lab, Research Centre for Biochemical, Environmental and Chemical Engineering. I would like to express and sorrily convey my deepest thankfulness to the soul of my previous supervisor (Mr. Prof. Ákos Rédey) and my supervisor Dr. Tatjána Juzsakova, all which I achieve is belong to her, the laboratory director and my thesis director for entrusting me with this subject, as well as for her encouragement, invaluable advice, motivation and regular monitoring. Thank you for all the time you have given me, your guidance and your encouragement during these four years. So I would like to express my deep gratitude to to her and to Professor Rédey.

I owe special thanks to Dr. Balázs Zsirka and Dr. Viktor Sebestyén, for their kindness, availability, and support. I owe also a debt of gratitude to Prof. Dr. Rashid Talib Rasheed from University of Technology, Baghdad, Iraq, for his support, help and approachability and without his counsel, the work will be not easy, special thank to him.

Additionally, I would like to thank Dr. Endre Domokos, the head of Research Centre for Biochemical, Environmental and Chemical Engineering, for his help and support. Also I would like to praise all the research fellows (Dr. M. Al Asadi, Mr. Ali Dawood Salman, Dr. Viola Somogyi, Mr. János Láko, Mr. Bali, Mrs. Ruqaia Rizk, Ms. Katalin Győrfi, Ms Kinga Berta, Mr. Béla Varga, Ms. Gvendolin Kulcsar, Mr. Yahiea Al-Naimy, Mr. Ramy Saad, Mr. Ali Umara, and Ms. Rebeka Borsfai), whom I had the opportunity to exchange ideas and knowledge. I would have to thank them for their patience and assistance.

It is impossible to extend enough thanks to my family, especially my parents, brothets and sisters who gave me the encouragement I needed throughout this process.

Finally, this work would have been a much more difficult feat without my caring mother, lovely wife, and my uncle Prof. Dr. Hussein Al Goburi.

Thank you all for your unwavering support and for reminding me to take breaks and have fun when I've been stressed out.

1. Introduction

Although the global economy continues to expand rapidly as a result of the exploitation and production of crude oil, its transportation and derivatives potentially remain a serious threat to the environment [1]. Among many other challenges, oil spills remain major ecological and environmental concerns [2]. Dubansky et al. has reported that the contamination of sensitive estuaries with crude oil along the Gulf Coast impacts populations as a result of consuming toxic fish [3]. Major oil-spill incidents around the globe over recent years such as the Rayong oil spill in the Gulf of Thailand in 2013, the series of Tianjin explosions in China in 2015 as well as the sinkings of the tankers Agia Zoni II and Sanchi in the Saronic Gulf in Greece 2017 and in the East China Sea in 2018, respectively, have affected not only marine life but also resulted in fatalities and will continue to affect ecosystems for decades to come [4]. Only one large and four medium oil-tanker spills were reported in 2021 totalling about 10,000 tonnes (ITOPF, 2021).

Oil spills release volatile organic compounds (VOCs) and heavy hydrocarbons into the aquatic environment causing severe damage to the ecosystem [5]. Petroleum hydrocarbons, heavy metals and other compounds also fall within the category of primary pollutants which have severe impacts on living organisms due to their neurotoxic and carcinogenic effects [6]. Numerous research studies have extensively assessed these pollutants and found that their toxicity levels have exceeded upper limits set according to international standards [7]. Water pollution is a threat since it affects hundreds of millions of people within a short period of time. Due to the polar structure of the water molecule, it dissolves chemical and biological contaminants which affect the water supply system making it hazardous for aquatic life and public health alike [8]. The gravity of the situation has rendered the treatment of oil spills an emerging as well as contemporary problem and drawn the attention of researchers working to remove organic contaminants and floating oil by developing novel cleanup methods using environmentally friendly materials.

The intensive development of the pharmaceutical, agricultural and chemical industries has resulted in the release of a diverse range of chemical compounds such as antibiotics, plastics, pesticides and dyes into aquatic environments [9]. These industries serve as major contributors towards the contamination of aquatic environments since manifold chemicals are discharged directly and very frequently into the environment [10]. As a

result, discharging dyes into the aquatic environment makes the colour of water undesirable and increases its toxicity affecting both human and aquatic species [11].

Hence, this has necessitated urgent and concerted efforts to develop modern methods for the remediation of water bodies contaminated by organic matter, hydrocarbons or toxic metals. Several traditional decontamination methods for cleaning up oil spills exist based on physical, chemical and biological treatments. Furthermore, certain methods involve the mechanical recovery of oil present in areas with natural or artificial barriers by the processes of filtration, diffusion, strippin, skimming, in-situ burning, gravity separation and emulsification or using gelling agents, membrane bioreactors, dispersants and solidifiers. These physical methods for cleaning up oil spills suffer from many disadvantages such as being time-consuming, inefficient and generating a significant amount of waste.

In the case of non-mechanical recovery methods, numerous techniques have been applied, including chemical and some biological decontamination methods such as adsorption, chemical coagulation, dispersion, burning, phytoremediation or bioremediation. From among these methods, adsorption is a top choice globally in industries as well as research laboratories owing to its simplicity, safety and remarkable efficiency with regard to cleaning up oil spills as it does not involve any other potential risks [12].

Three categories of adsorbents are employed to cleanup oil spills such as natural organic, mineral and synthetic organic adsorbents. The capacity and functionality of each category of adsorbents is different but limited in the case of cleaning up oil spills. Although the first category of natural adsorbents consists of biodegradable materials, they must be avoided in the event of a fire. Since the second category of mineral adsorbents exhibits a lower level of hydrophobicity, their capacity to adsorb oil is less, while the third category of synthetic organic adsorbents has exhibited a high level of hydrophobicity, thereby rendering them suitable [13]. Previously used adsorbents like activated carbon, propylene, zeolites etc. have some limitations due to their poor selectivity, low adsorption capacity, higher manufacturing coast and limited recyclability [14].

1.1 Context and Aims

Over the previous decade, the field of nanotechnology has greatly revolutionized the methods of environmental remediation because nanoparticles hold manifold benefits such as their large surface area, more active adsorption sites, high reactivity and small size [15]. Carbon nanotubes (CNTs) can simply be defined as a group of carboneous nanomaterials which have a tubular structure and consist of hexagonal rings of carbon atoms bonded covalently. CNTs, in comparison with other nanoparticles, exhibit a relatively higher adsorption affinity for the removal of volatile organic compounds [14] as well as are suitable for water treatment including the removal of oil and toxic organic compounds [16] in addition to heavy metal ions [17]. Likewise, most recently, CNTs are applied as potential adsorbents in a variety of remediation techniques in almost all environmental fields, including the removal of organic pollutants [1], heavy metals from aqueous media [2], antibiotics [18] and nitrates [19]. This has attributed to several of their characteristic features [20] such as their low density, electrical conductivity, large specific surface area, high inherent strength, higher adsorption capacity, good degree of hydrophobicity, thermal and chemical stability, high aspect ratio, fast adsorption rate, oleophilic characteristics and hydrogen-storage capacity [21].

To reduce the poor mechanical strength of metal oxide nanomaterials, nanocomposites are increasingly used to purify wastewater by removing unwanted species [22]-[23]. The combination of nanoadsorbents with metal oxide nanoparticles has been the first choice of researchers to generate adsorbent materials. The preparation of nanosized metal oxides and their characterization have been studied by many researchers [24]–[28]. Recently, researchers have utilized numerous metal oxide nanoparticles for the treatment of wastewaters such as titanium dioxide (TiO_2), manganese dioxide (MnO_2), cerium oxide (CeO_2), zinc oxide (ZnO), vanadium pentoxide (V_2O_5), iron oxide (Fe_2O_3) and copper oxide (CuO). The discovery of CNTs has provided several advantages in removing unwanted and hazardous organic pollutants from water. The controlled pore size and wide distribution of surface active sites leads to higher adsorption efficiencies compared to those of sorbents [7] [29]-[30]. Composite materials are extensively applied to remove inorganic pollutants such as metal ions and metal oxides [31] as well as organic pollutants like dyes, pesticides, antibiotics and hydrocarbons.

Nanoadsorbents offer multiple advantages such as having multiple sorption sites, huge surface areas, short intraparticle diffusion coefficients, tunable pore sizes and being

modifiable at low temperatures. The surface modification of magnetic nanosorbents is instrumental in achieving the characteristic features of high adsorption capacity, superparamagnetism, biocompatibility, high magnetic saturation and reusability [32]. Although magnetic nanosorbents are functionalized by surface modification using a wide variety of materials, the smart materials among them are polymers which are nontoxic, biodegradable and biocompatible polymeric materials [33]. Since microporous polymer-coated nanosorbents possess a high degree of surface roughness and elasticity, the unique properties of superhydrophobicity and superoleophilicity in terms of oil removal are achieved [34].

These adsorbents have been selected solely as a result of a comprehensive literature review of existing oil adsorbents that are highly efficient and environmentally friendly. All adsorbents such as metal oxide nanocomposites as well as polymer- and metal oxide-modified MWCNTs have a unique structure and relatively high specific surface area in addition to exceptional mechanical properties, rapid sorption rates, high sorption capacities and engineered surface chemistry [35]–[38].

1.2 The worldwide problem of water pollution

Even though three-fourths of the Earth is covered in water, less than 1% of it is safe for human consumption, therefore, much of its population does not have access to sufficient drinking water [39]. Naturally occurring fresh water is regularly contaminated by a number of anthropogenic activities and industrial processes. The significant growth in the global population has led towards enormous industrial applications which have resulted in the release of organic pollutants, especially from manufacturing industries [40]. The most frequently encountered organic pollutants include toluene, dyes, kerosene, antibiotics and oil spills.

1.2.1 Water pollution by oil spills

Incessant oil spills cause irreparable environmental and ecological damage in both the short- and long-term [29] [41]. Contaminants transmitted into bodies of water via oil spills include kerosene, gasoline, petrol, diesel as well as heavy and lubricating oils [42].

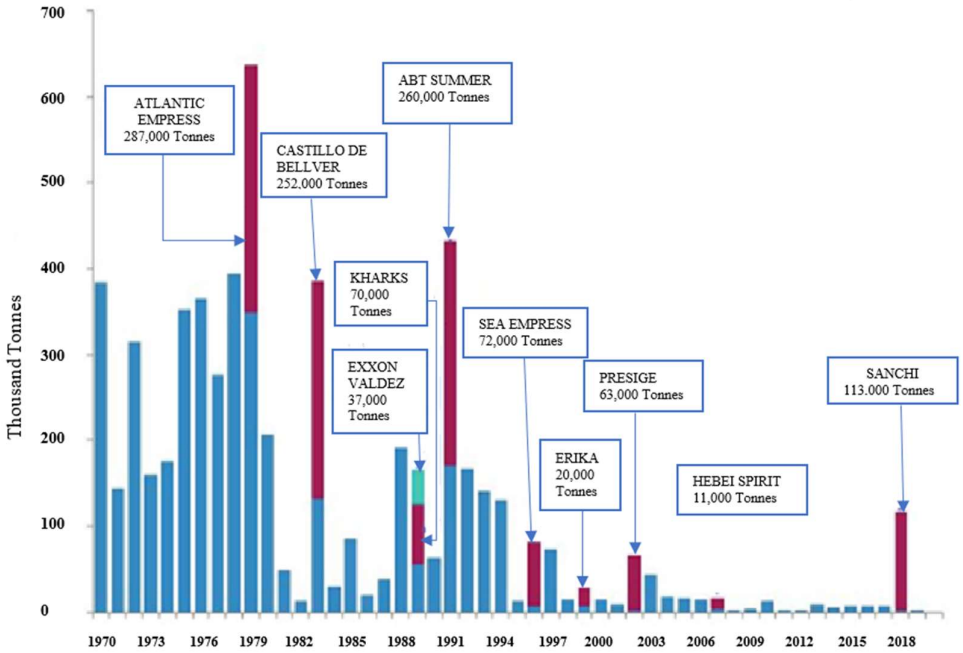

Figure 1. The seven major oil spills that occurred between 1970 and 2020

Moreover oil tanker spills are considered to be the primary source of water contamination as over the previous 50 years, statistics concerning the frequency of oil spills of greater than seven tons from oil tankers show a marked downward trend as illustrated in Figures1 and 2 (ITOPF Limited, 2019) [43]. The number of large oil spills (>700 tons) has decreased significantly over recent decades. On average, 1.8 spills were recorded on an annual basis in the 2010s which is less than a tenth of the average recorded in the 1970s. No large oil spills were recorded in 2020. Similarly, a significant decrease has been observed in the quantity of oil spilled over recent decades. In the 2010s, altogether approximately 164,000 tons of oil was spilt from tankers and on average, at least 7 tonnes of oil was released per spill, equating to a 95% reduction since the 1970s.

Kerosene is a distillate of petroleum and one of the major pollutants found in the environment, especially in water, as it consists of numerous aliphatic and aromatic hydrocarbons such as alkanes, cycloalkanes, toluene, benzene and olefins. It causes multiple health complications in humans, for example, cardiac arrhythmias, ventricular fibrillation, lacrimation and ocular irritation depending on how abundant the various components of kerosene are [44]-[45].

The gravity of the situation has motivated quite a large number of researchers to determine the most efficient decontamination and cleanup strategy to remove an oil slick resulting from an oil spill [46]. Conventional decontamination methods such as physical,

biological and chemical methods are inefficient for the separation of emulsified oil from water and sometimes may even result in secondary pollution.

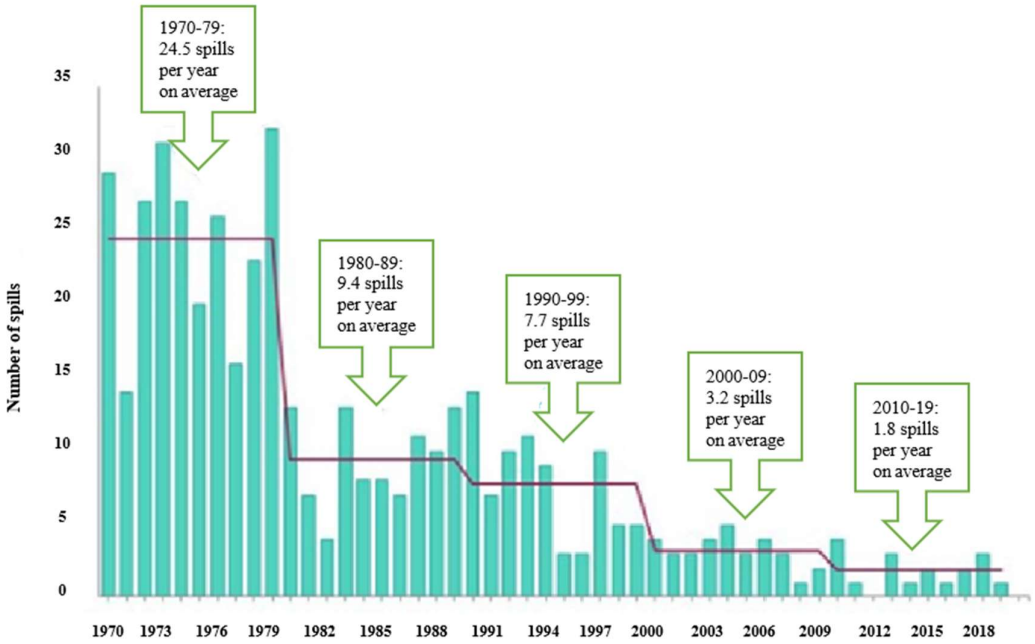

Figure 2. Gradual decrease in the frequency of oil spills between 1970 and 2020

Being simple and rapid, the physical adsorption method has been extensively applied but due to its low adsorption capacity and limited reusability, its applicability has been suppressed [46]. As a result, the fabrication of new absorbents has paved the way for the extensive use of nanomaterials. The application of nanocomposites has been exceptional with regard to the removal of oil components from contaminated water because of their high adsorption capacity stability and recyclability as well as being environmentally friendly, exhibiting low levels of cytotoxicity and offering facile synthesis routes [48]-[49].

1.2.2 Water pollution by organic dyes

Although the increase in industrial development has improved our quality of life, it has equally posed a constant threat to human health as well as the environment because of the enormous quantity of waste generated and wastewater effluents discharged into aquatic environments [49]. Wastewater effluents from industries-predominantly from the chemical, cosmetics, textile, leather, printing and paper industries-contain significant amounts of toxic, carcinogenic and harmful substances, including heavy metals dyes and other chromophoric groups [51]-[52]. Due to the presence of numerous dyes in water, the

penetration of sunlight is reduced causing irreparable damage in aquatic environments, moreover, changes in the taste and color of water is commonly observed [52]. Dyes polluted with water can cause multiple health problems for human beings, including breathing difficulties nausea skin irritation allergic contact dermatitis, vomiting and mental confusion, moreover, can even lead to cancer [53].

Methylene blue (MB) is amongst the most widely used cationic organic dyes on an industrial scale in disinfectants and colouring agents in varnishes leather pesticides and pharmaceuticals as well as in the printing and rubber industries amongst others. It has been extensively applied in the dyestuff industry [54]. MB is thermally stable heat-resistant and non-biodegradable with an aromatic molecular structure which hinders photosynthesis in aquatic plants by hampering the transmission of sunlight [55]. Given that the use of dyes is necessary in many industries researchers around the globe have been motivated since the development of highly efficient cost-effective and environmentally friendly techniques for the degradation and removal of these noxious substances from the aquatic environment is time-consuming [57]-[58].

1.3 Adsorption technology for water treatment

One of the commonly used surface phenomena for the removal of pollutants from the waste water is adsorption. The process have two basic components; adsorbate (solute in the solution) and adsorbent (porous solid) as explained in Figure 3. In the case of dye or hydrocarbon removal from water the pollutant molecule is an adsorbate which adsorbed on the surface of adsorbent which can be any compatible solid with high surface area and surface binding compatibility. The adsorbent can make weak bonds (dipole-dipole interactions, hydrogen bonding) or strong bonds (ionic, metallic, and covalent) with the adsorbate molecule depending upon the type of functionality present on the adsorbent [58].

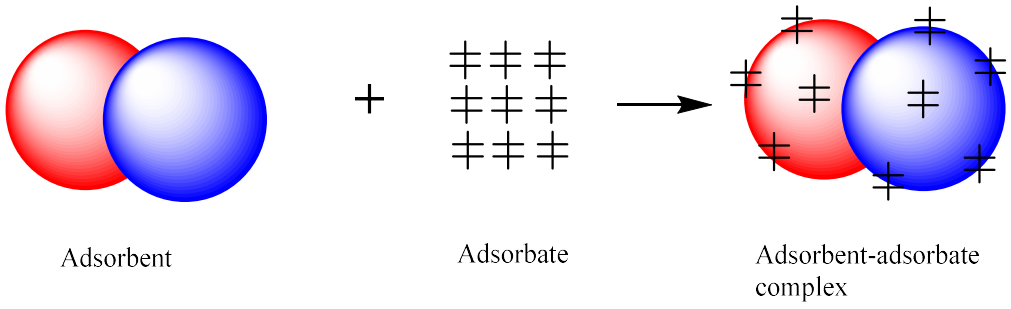

Figure 3. Mechanism of the adsorption process

1.3.1. Treatment techniques for the removal of hydrocarbons

The treatment of oil spills and contamination is poorly understood and a major problem faced by researchers [59]. Existing strategies that have been applied to remove oil from water are air flotation, centrifugation, electrochemical and photocatalytic treatments, adsorption as well as gravity separation [60]. Unfortunately these techniques have limitations including large carbon footprints, their energy-intensive nature, poor separation efficiency and sometimes resultant secondary pollution [61]. Therefore, they are unsuitable for the removal of oil from water. The other separation technique considered to remove oil is membrane technology which has advantages, including a low carbon footprint, low energy consumption and high efficacy [62]. Membrane technologies that have commonly been used in oil-water separation are reverse osmosis, nanofiltration and ultrafiltration.

However, the cleaning of membranes is costly since it requires chemicals, is energy-intensive and results in longer downtimes, therefore, is unsuitable for oil-water separation [63]. Apparently, studies have shown that researchers are switching their attention to nanotechnology since this field has impacted the revolution in materials science. Nanomaterials have exhibited impeccable properties (e.g. higher sorption performance, superhydrophobicity, mechanical properties and superoleophobicity) that can be effective in terms of oil-water separation [64]. Furthermore, nanomaterials can remove insoluble oil as well as soluble dyes via various mechanisms, including photodegradation, sieving and adsorption [65]. As a result, nanocomposites are potential materials to bring about the removal of oil from water. Nanomaterials are normally common, high-performance materials with enhanced properties that have recently been developed. Moreover, they may consist of many types of materials (e.g. metals, polymers and ceramics) as well as include semiconductors, nanoengineered materials and biomaterials. The most successful adsorbents are nanomaterials due their higher surface area and compatibility for functionalization. Numerous polymer nanocomposites with higher sorption capacities have been reported. Nanomaterials used to remove oil from water are illustrated in Figure 4.

The numerous adsorbents recently reported by researchers for the treatment of oily wastewater are summarized in Table 1. Which contains comprehensive data about the types of adsorbents used to adsorb various components of oil along with their maximum sorption capacities. Of all these methods for the successful removal of oil from water, the

surface modifications of polymer nanocomposites with organic functionalities have remained a distinguished technique, including the use of a variety of functional groups like hydroxyls, amides, carboxylates, phosphates and sulphates.

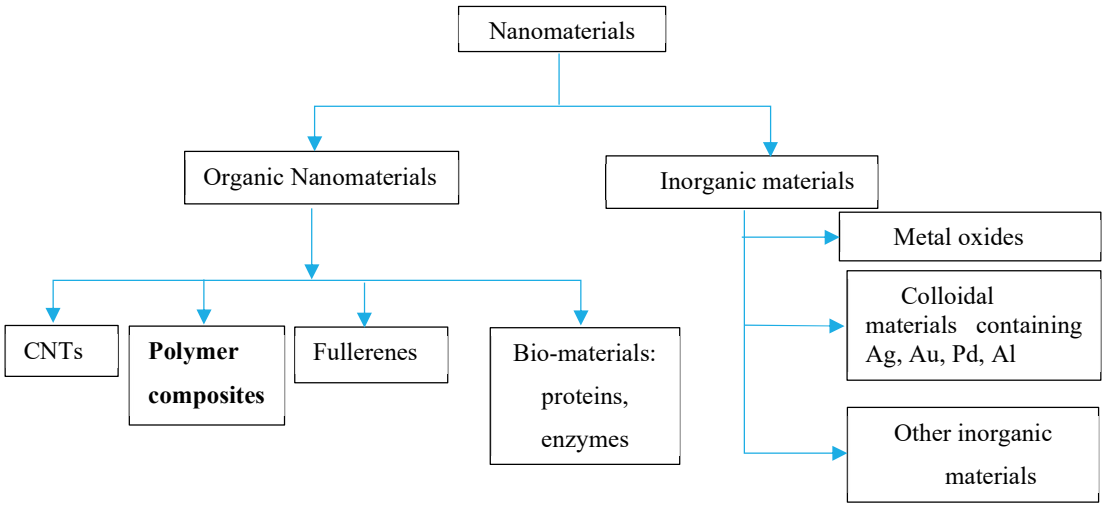

Figure 4. Nanomaterials used to remove oil from water by adsorption

Table 1. Applications of different nanocomposites to remove oil from water

Adsorbent-based material	oil/hydrocarbon pollutants	Sorption capacity (g/g)	Ref.
Polyester loaded with ground coffee powder and maghemite	Petroleum	25.1	[66]
Polyester	Diesel and petrol	6.9	[67]
Magnetic polystyrene–palygorskite nanocomposite	Crude oil	0.5	[68]
Acetylated corn cob	Crude oil	4.3	[69]
Polyurethane foams and rice straw	Gasoline	12.0	[70]
$CuFe_2O_4$-doped graphene	Petrol	14.5	[71]
Chitosan	Petrol	48.2	[72]
Acrylate terpolymer	Diesel	12.0	[73]
Nylon 6	Crude oil	11.1	[74]
Magnetic nanocomposites	Pump oil	8.0	[75]
Lignin	Gasoline	25.0	[76]
Silicon dioxide	Crude oil	21.1	[77]
Magnetic zeolite	Gasoline	20.0	[78]
Poly(styrene-co-divinylbenzene)	Crude oil	11.0	[79]
CNTs	Gasoline	18.0	[63]
Photothermal CNTs	Crude oil	16.3	[80]
Polystyrene doped Fe_3O_4	Diesel	9.6	[81]
UIO-66-F4@rGO composites	Diesel	15.2	[82]
Polymer-nanoparticle-fluorosurfactant complex	Gasoline	26.3	[83]
Fe_3O_4 polymeric nanoparticles	Crude oil	30.2	[84]
Polyether block amide	Paraffin	12.0	[85]
Ferrite-magnetic fibrous composites	Crude oil	11.0	[86]
Polyethylenimine-modified graphene	Seed and sunflower oil	8.0	[75]

1.3.2. Treatment techniques for the removal of dyes

The organic dye molecules normally consists of two parts; colour bearing part called chromophore and auxochrome which is responsible for interaction of dye with fibres and its solubility [87]. Dyes if present in the wastewater can greatly affect the aquatic environment. It is very important to remove dyes from the waste water. There are different methods in practice for the removal dyes from waste water. Some of these methods have high efficiency for the dye removal but are not feasible economically. Some of the economical methods have less efficiency. It's very important to develop some methods which are not only effective economically and safe for the environment as well [88].

Some of the methods are described below:

- ***Physical methods*:** Physical methods for the treatment waste water includes reverse osmosis, membrane treatment, filtration and adsorption. One of the determining factor to choose a viable method is its economic viability. From all these methods adsorption is proved to be the most economical and efficient method [91]-[92]. Some of the most commonly used adsorbents are zeolites, carbon nanotubes, clay particles, multiwalled carbon nanotubes etc. These adsorbent materials have higher surface area for the adsorption of wastes onto the surface [93]-[94].
- ***Chemical treatment*:** Some of the most commonly used chemical agents for the treatment polluted water are coagulants. For the chemical treatment of water aluminium, calcium or ferric ions are added into the polluted water [93]-[94]. Although chemical treatment is effective and economical but one major drawback is the formation of sludge as the reactions are dependent on pH. This by product is concerning due to the problems caused by its disposal [95].
- ***Biological methods*:** Biological treatment is one of the most economical method for the treatment of polluted water. The biological method involves the use of microorganisms like yeast, bacteria, algae or fungi. The process can be aerobic or anaerobic [96]. One of the major drawback for the biological treatment is sensitivity and dependence of microorganisms. Some of the recent researches proved that the biological treatment does not perform satisfactory results for the removal of colour and it's not as efficient as much as it is economical.

Figure 5 shows the effect of some of the important factors like surface area, contact time, temperature, pH etc. on the rate of adsorption of pollutant molecules [100]-[101]. For an adsorbent to be effective, parameters like surface area, porosity, adsorption capacity and mechanical stability should be as high as possible along with the feasibility

of other factors such as cost-effectiveness, facile regeneration, sustainability and selectivity [99].

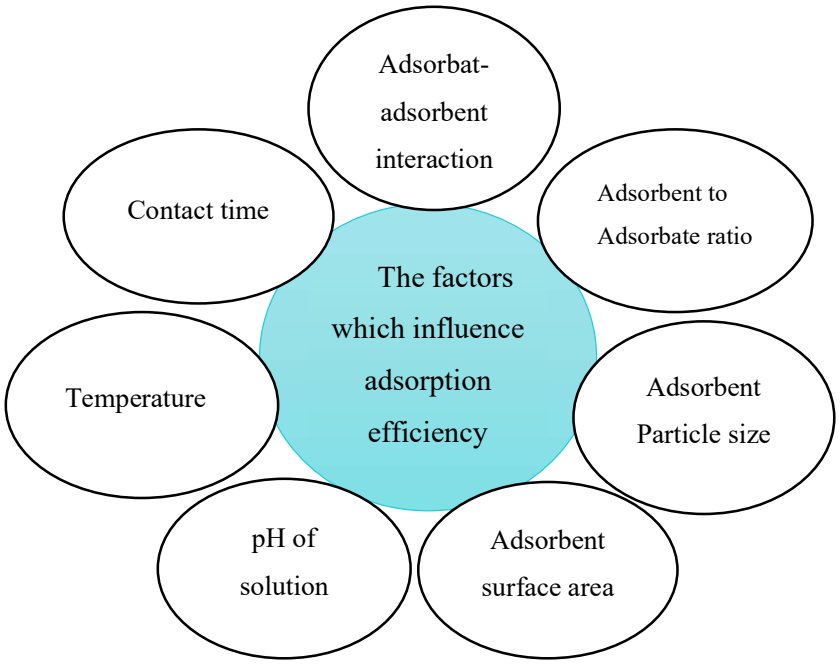

Figure 5. Factors which effect the adsorption efficiency in the adsorption process

Many adsorbents are currently applied for the treatment of wastewater. These adsorbents are derived from agricultural, domestic and industrial waste, polymers as well as organic and inorganic materials. However, in most cases, the adsorbents obtained from the aforementioned inexpensive materials have low adsorption efficiencies. Therefore, it has become necessary to find more advanced, effective and proficient adsorbents for the efficient treatment of polluted wastewater.

1.4. Adsorbent nanomaterials

Nowadays nanoscience and nanotechnology are rapidly growing sectors and drawing an exceptional amount of attention with regard to wastewater treatment. Innumerable nanomaterials have been extensively synthesized and used for the elimination of contaminants from wastewater[103]-[104]. Since nanomaterials are small (approximately 100 nm in diameter), their surface area to volume ratio is exceptionally high which facilitates faster rates of adsorption and much higher removal efficiencies of pollutants present in wastewater. Nanoadsorbents can penetrate deeper, work rapidly, bind strongly to pollutants and treat wastewater more effectively [102]. Nanoadsorbents can be used in many forms like nanotubes, nanoparticles and nanofilms for the wastewater treatment

[103] [104]. Previously, many researches have proved the efficiency of nano-adsorbants due to their higher surface area, highly porous structure, high dispersion ability and cost-effectiveness [105].

Wastewater treatments using nanotechnology are perceived to be favorable initiatives, not only in terms of overcoming the main challenges concerning wastewater treatment but also due to their ability to offer unique treatments that could facilitate the cost-effective utilization of alternative water sources to increase the water supply. The size range of nanoparticles (NPs) is from 1 to 100 nm and are dispersed throughout all types of media, namely gases, liquids and solids. All of the above features make nano-adsorbents the best candidate for wastewater treatment [106].

Nanomaterials can be classified as inorganic NPs [107], polymeric NPs [108], solid lipid NPs [109], liposomal NPs [110], nanocrystals [111], nanotubes and dendrimers [112]. Some nanomaterials that are commonly used as adsorbents are presented in Figure 6

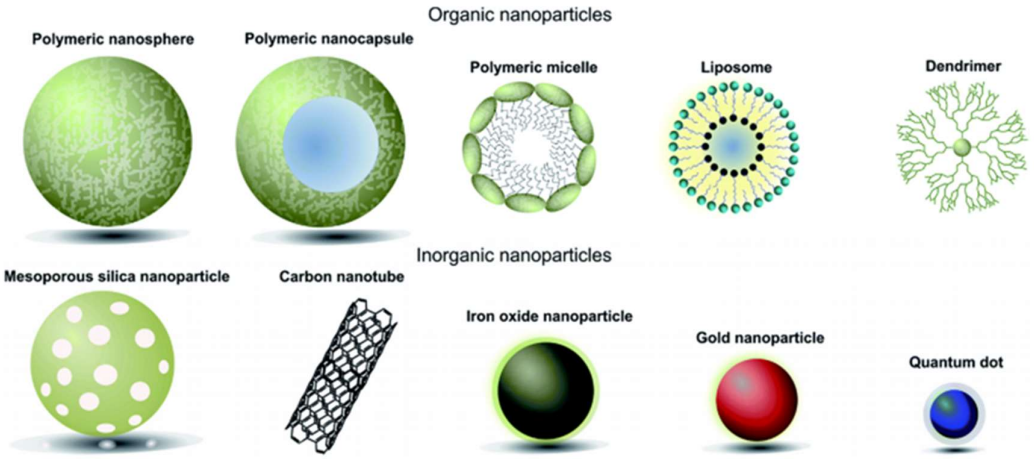

Figure 6. Various types of nanomaterials [106]

1.4.1. Metal oxide nanomaterials as adsorbents

Transition metal oxide nanoparticles such as copper oxide (CuO), iron oxide (Fe_2O_3), zinc oxide (ZnO), manganese dioxide (MnO_2) and vanadium pentoxide (V_2O_5) have been extensively used as photocatalysts for the purpose of water purification. These photocatalytic materials have a large surface area, are chemically stable and efficiently recycled while yield no secondary pollutants [27]. V_2O_5 nanomaterials have been applied in numerous photocatalytic degradation applications because of their nontoxicity, narrow band gap (~2.4-2.8 eV) as well as better chemical and electrical stability. To eliminate

the limitations of V_2O_5, its morphology has been modified. Carbon nanotubes (CNTs) are the best choice since they combine the efficient and effective use of V_2O_5 nanoparticles to remove dyes. V_2O_5 nanostructured materials can be in the form of nanoparticles, nanowires, nanorods, nanobelts, nanoribbons and nanosheets of desired size and morphology with their distinct geometry as well as new physical and chemical properties [23].

Combining nanoadsorbents with metal oxide nanoparticles is the first choice for researchers producing adsorbent materials. The preparation of nanosized metal oxides and their characterization has been studied by many researchers [25]. The use of nano-sized metal oxides for the removal of water pollutants, including hydrocarbons, has been reported by [113]. A nanostructured zinc oxide adsorbent was developed, characterized and efficiently used to remove methyl orange (MO) dyes and amaranth (AM) from water [114]. The mechanism for the separation is given in Figure 7.

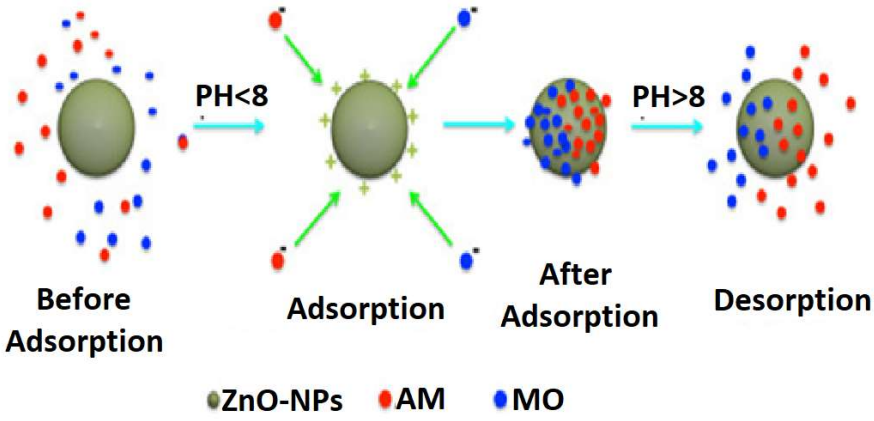

Figure 7. The interaction between dyes and zinc oxide nanoparticles [114]

1.4.2. Carbon nanotubes: synthesis, structure and properties

Carbon nanotubes (CNTs) were discovered by Iijima in 1991 [115], [116]. After the discovery of carbon nanotubes no one can get enough of their uses due to their versatility. Carbon nanotubes can be divided in to two major types: i) SWCNTs (single walled carbon nanotubes) and ii) MWCNTs (multiwalled carbon nanotubes) are presented in Figure 8 [117], [118]. MWCNTs are considered as fullerenes [119]. First ever CNTs were prepared by the pyrolysis of ferrocene and benzene at higher temperatures of around 1000 °C [120]. Due to their wide application in many industries carbon nanotubes are given the title of the material of 21st century [121] The mechanical, functional and thermal properties of

CNTs depends upon the arrangement of their atoms which are rolled to form sheets of graphite [122].

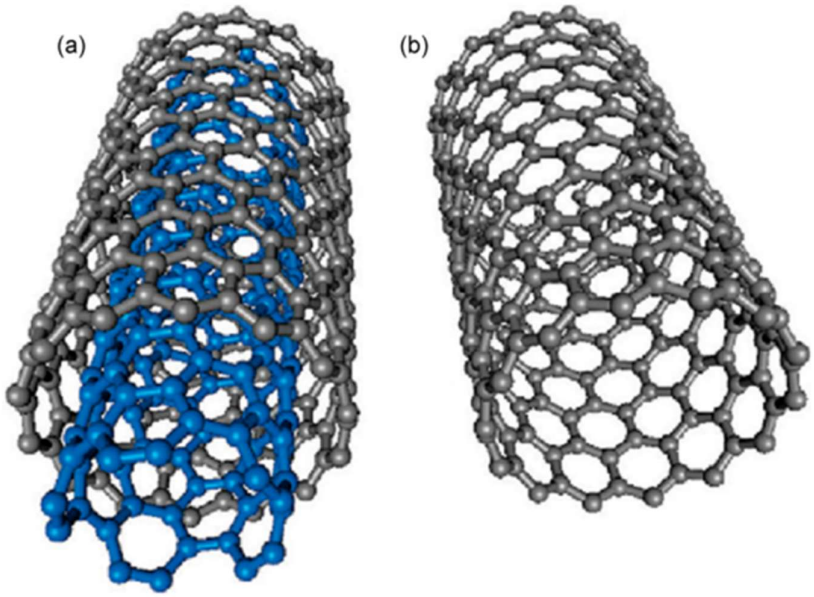

Figure 8. Structure of (a) MWCNTs and (b) SWCNTs [118]

At present, theoretical and experimental investigations of the properties and applications of CNTs in multidisciplinary areas are increasing exponentially. As a result of the current and increasing investment as well as their potential widespread use, CNTs have quickly become commonplace in the environment. Several studies suggest that they are toxic to human beings as well as other organisms and their presence in the environment affects the physicochemical behaviour of common environmental pollutants such as heavy metal ions [123] and organic compounds [124]. CNTs have the ability to react with metals as well with non-metals due to the presence of functional groups onto the surface.

Carbon nanotubes as adsorbents have got considerable attention due to their efficiency for adoption as compared to other carbon base adsorbents. The major advantage of CNTs is their higher surface area and their porous structure [125]–[129]. The adsorption efficiency of multi-walled carbon nanotubes can be increased by modification by heavy metal ions [130], [131], radionuclides [132] and organic chemicals [133]-[134].

Numerous techniques and methods have been devised as well as used to synthesize MWCNTs for a variety of applications in a wide range of fields. Two approaches can be followed for the synthesis of CNTs, namely the bottom-up and top-down approaches. The methods involved in both approaches are presented in Figure 9. The most common of

these methods include laser ablation, arc discharge and chemical vapor deposition (CVD) [135].

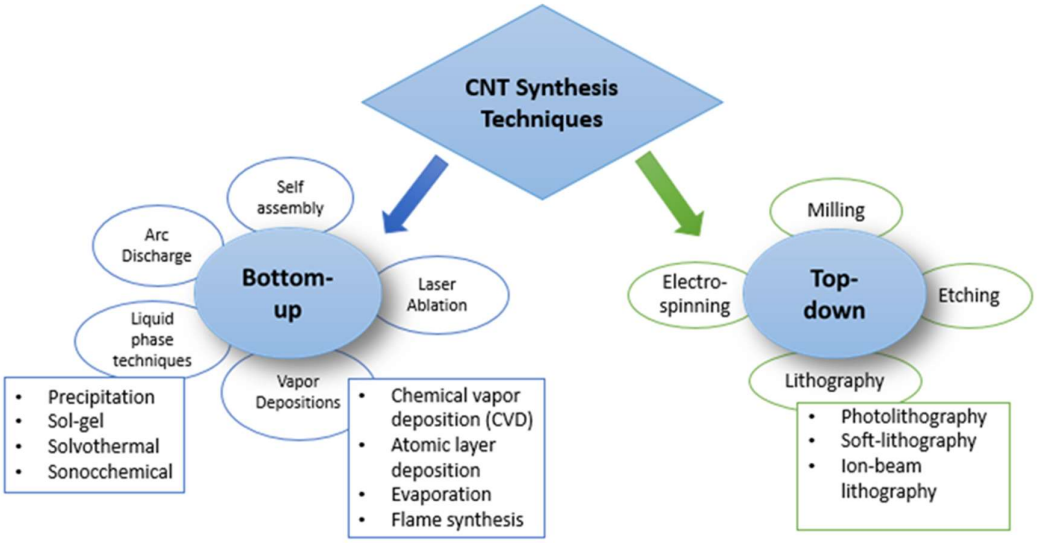

Figure 9. Various methods used for the synthesis of CNTs [135]

The most commonly used method for the functionalization of CNTs is oxidization which can be photooxidation, acidic oxidation as well as gas-phase and oxygen plasma treatments [136]. Acidic oxidation is one of the most widely used methods where HNO_3, H_2SO_4 and air are applied. Carboxylic functional groups are formed in CNTs when treated with nitric acid which can help to enhance their solubility and reactivity [137]-[138].

Various possible mechanisms to modify carbon nanotubes are represented in Figure 10, which presents the different methods used to add functionalities to CNTs.

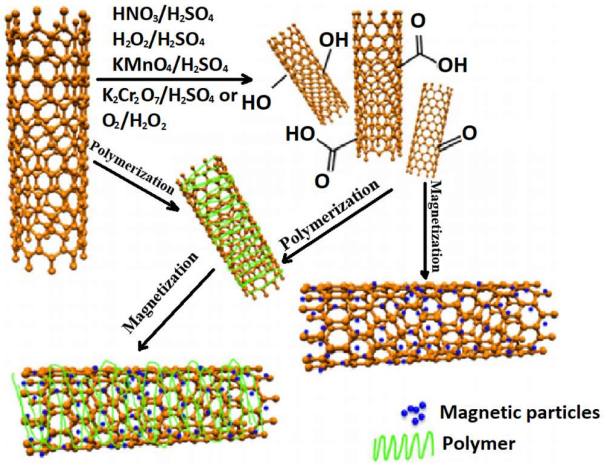

Figure 10. Common functionalization routes of carbon nanotubes [139]

Many research studies have provided evidence of the enhanced removal of dyes from wastewater by modifying carbon nanotube adsorbents with functional groups [140]–

[142]. These functionalization of CNTs increase the selectivity for aromatic pollutants in aqueous media as well as the adsorption capacity and decreases hydrophobicity and aggregation of CNTs [139]-[140]. Functionalized CNTs can be widely applied as adsorbents for removing organic pollutants from water due to their ability to form π-π interactions and hydrogen bonding. The lower manufacturing cost, larger surface area and hydrophopic character of CNTs make them ideal adsorbents for the removal of organic pollutants like aromatic compounds, oil, heavy metals and organic dyes from water. There are many factors that determine the functionalization efficiency of CNTs [144]. The presence of reactive functional groups like -OH and -COOH increases the adsorption capacity of CNTs [123] [142]-[143].

Mechanism of adsorption can be understood by studying the adsorption properties of carbon nanotubes [147]. Firstly, the contribution of individual adsorption sites. Through temperature programmed desorption studies of various alkanes on carbon nanotube bundles, it can be observed that different groups of adsorption sites are present in the bundles [148].

Different pollutants can be adsorbed at four possible sites (Figure 11) in CNT bundles [149]: (i) “internal sites” the hollow interior of individual nanotubes (only accessible if their caps are removed and their open ends unblocked); (ii) “interstitial channels (ICs)” between individual nanotubes in the bundles; (iii) “grooves” inside the grooves one dimensional chain are formed by open ended nanotubes; (iv) the remaining axial sites of CNTs are filled to complete the quasi-hexagonal layer which is present on the outer side of bundles [150].

It is interesting to note that the adsorption reaches equilibrium much faster at external sites (grooves and outer surfaces) than at the internal sites (interstitial channels and inside the tube) under the same pressure and temperature conditions.

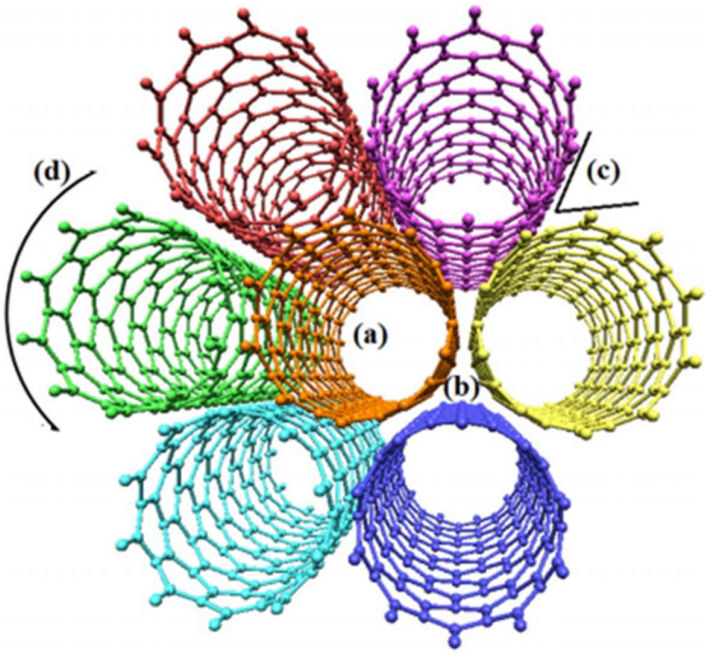

Figure 11. Possible adsorption sites for the interaction between contaminants and carbon nanotubes: (a) internal sites, (b) interstitial channels, (c) external grooves and (d) exposed surface sites [151]

Adsorption technology with regard to MWCNTs is promising for the removal of pollutants due to its efficiency, simplicity, inexpensive nature and insensitivity to toxicity. To date, numerous models have been formulated to describe the adsorption of organic molecules on CNTs in the aqueous phase, e.g. the Freundlich and Langmuir isotherms amongst others. Organic chemical adsorption on MWCNTs is equivalent to or even more effective than that on activated carbon. Therefore, the surface area may not be suitable for forecasting organic chemical-MWCNT interactions. Su and Lu related the higher degree of adsorption of organic materials on CNTs to the larger average pore diameter and volume, morphology as well as functional groups [152]. It is worthwhile mentioning that adsorption on CNTs is of paramount importance [124] due to the existence of high-energy adsorption sites such as functional groups and interstitial, grooved regions between the graphene bundles [153]. Since these adsorption sites mainly exist on CNTs, adsorption seems to be a general feature. The second is the condensation phenomena in which the pores and capillaries of CNTs become filled with liquid condensed from vapour. While the organic chemicals adsorb on the surfaces of CNTs, multilayer adsorption might occur. In this process, the first couple of layers interact with the surface, while the molecules in deeper layers interact with each other. This process is known as

surface condensation [124].The outer surface of separate CNTs facilitates the even distribution of hydrophobic sites in organic chemicals. If this hydrophobic interaction is the only mechanism between organic chemicals and CNTs, adsorption via chemical bonds may be expected to occur. However, hydrophobic interactions cannot entirely describe the interaction between organic chemicals and CNTs [143]. Other mechanisms comprised of π–π interactions (between bulk π systems on the surfaces of CNTs and organic molecules with carbon-carbon double bonds or benzene rings), hydrogen bonds (resulting from functional groups on the surfaces of CNTs) and electrostatic interactions (given the charged surface of CNTs).

1.4.3. Metal oxide-doped CNTs

Researchers have utilized numerous metal oxide nanoparticles and metal oxide-modified MWCNTs for the treatment of wastewater [154]. Tan et al. has pointed out that oil spills can seriously threaten the environment and managed to successfully develop an environmentally friendly adsorbent for the removal of spilled oil on raw corn straw after the deposition of ZnO/SiO_2 nanocomposite particles with excellent superoleophilic and superhydrophobic characteristics [155]. Based on their research, Qiming et al. reported that the titania-modified carbon nanotube composite exhibited enhanced adsorption of organic pollutants for the purpose of their removal in comparison to pure TiO_2 nanoparticles [156]. Similarly, it was reported that functionalized silica-coated magnetic nanocomposites are efficient for the removal of organic pollutants from aqueous solutions [157]. Kirti et al. exploited the functionality of biomass in iron nanocomposites for the potential removal of four dyes, including both anionic and cationic dyes [158]. Similarly, Hassan et al. used SnO_2/CeO_2 nanocomposites to remove dyes [159]. Al-Jammal et al. reported a microemulsion technique for the functionalization of MWCNTs with a hydrocarbon tail to remove numerous hydrocarbons from water contaminated by oil [29].

TiO_2 nanostructures are usually prepared using a hydrothermal method where $TiCl_4$ is used as a precursor along with mixing deionized water and ethanol as starting materials in the ratio of 3:7 in an ice bath [160]. Another method for the preparation of titania-doped MWCNTs is wet impregnation [161]. The photocatalytic performance of these composites was tested with regard to the degradation of methyl orange (MO). The results indicated that modified nanocomposites exhibited higher efficiencies of MO degradation than pure TiO_2 nanoparticles [162]. As is presented in Figure 12, the improved catalytic activity of titania-modified MWCNTs may be due to the dominant contribution of

nanotubes in MWCNTs/TiO_2 composites, leading to an increase in the recombination rate of photogenerated electron-hole pairs.

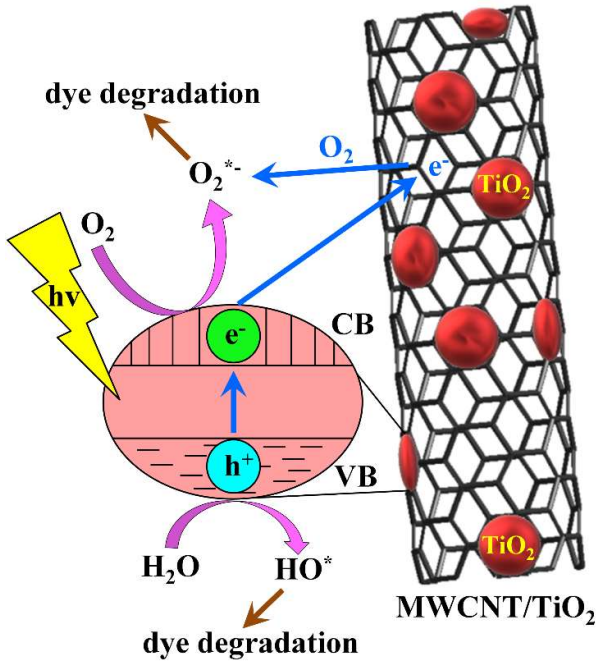

Figure 12. Mechanism of the photocatalytic degradation of dye with titanium dioxide-modified MWCNTs [162]

It is also evident from the delocalized π-structure characteristic of MWCNTs that this promotes electron transfer causing the separation of electron-hole pairs. TiO_2@LDH (layered double hydroxide) clay nanocomposites along with the deposition of anatase seeds onto the LDH clays have been successfully developed by Sefetl et al. for photo-degradation of aromatic pollutant (methylene blue, phenol) in water. Since the results indicate that this nanocomposite is more efficient in terms of the degradation of phenol, polymer-coated magnetic nanocomposite materials in complex networks constitute ideal and advanced absorbents for the remediation of components of oil from water. Titanium dioxide-modified MWCNTs composites are much more stable and non-toxic with an enhanced capability for the photooxidative destruction of hydrocarbons [163].

Iron(III) oxide, usually magnetite (Fe_3O_4), being ferromagnetic (hematite has a low iron content, moreover, is a component of rust and is paramagnetic), is also known as magnetic iron oxide. It is combined with MWCNTs through both physical and chemical methods. One of its most prominent features is the combination of magnetite with MWCNTs to produce superparamagnetic properties [164]. It is considered to be one of the most attractive magnetic metal oxides and has received widespread attention due to its unique physical and chemical properties as well as various advantages such as high

reversible capacity, rich abundance, low-cost and eco-friendliness [165]. This composite material, made by combining MWCNTs with magnetite, has a large specific surface area, hollow structure, is highly porous and exhibits strong interactions with adsorbed pollutants [166].

1.4.4. Polymer-modified CNTs

Polymer nanocomposites along with MWCNTs, graphene and magnetite have been applied as sorbents given their excellent efficiency of and remarkable ability to remove components of oil from contaminated water. Akinpelu et al. have extensively reviewed the applications of numerous CNTs in different forms for the removal of polycyclic aromatic hydrocarbons from wastewater [167]. Elmobarak and Almomani have reported an innovative magnetic demulsifier where magnetite nanoparticles grafted onto silica were applied to recover oil from oil-in-water emulsions [168]. Yamashita et al. developed composites (vinyltrimethoxysilane silica doped magnetite) for separation of oil from water by using sol-gel method under alkaline conditions [169]. Furthermore, a number of nanocomposite applications have been reported using polymers such as polyethylene [169]-[170] and magnetite [171]-[172] in a variety of fields including oil-water separation.

The rapid cost-effective and almost complete removal of oil by hydrophilic polyvinylpyrrolidone-coated magnetite nanoparticles under optimized conditions. Another advantage of this method is that both PVP and magnetite exhibit low levels of toxicity [174]. Huggias et al. synthesized silver and platinum nanoparticles supported on polyurethane as well as adsorbed on S-layer protein particles and reported catalytic activity during the reduction of the pollutant *p*-nitrophenol. The developed platinum and silver bio-nanocatalysts exhibited conversions of 100% and 97%, respectively [175].

1.5. Aim and scope

This study aims to develop an effective, flexible, sustainable and environmentally friendly adsorbent as well as decrease the amount of MWCNTs used for adsorption by adding polymers and metal oxides which make MWCNTs cost-effective and increase their removal efficiency of hydrocarbons and dyes. The efficiency of all the adsorbents with regard to the removal of model hydrocarbons, including kerosene, toluene and methylene blue an organic dye, was further investigated by studying the physicochemical characteristics of the proposed adsorbents.

The main parameters that influence their ability to adsorb pollutants are considered. Therefore, the main aims of this thesis are as follows:

- To develop new nanoadsorbent-based MWCNTs for the removal of pollutants from water by different functionalization techniques: metal oxide nanoparticles prepared at different annealing temperatures, metal oxide-doped MWCNTs and different polymer-modified MWCNTs.
- Characterize both raw and modified MWCNT adsorbents to determine if the selectivity or adsorption capacity of the selected treatment is better than those of adsorbents currently used.
- Study the sorption models to determine the mechanism for the sorption of hydrocarbons and organic dye.
- Identify different parameters (temperature, contact time, dose, pH) that affect the performance of adsorbents and determine their optimum values to maximize the rate of adsorption.
- Investigate different pseudo first-order and pseudo second-order kinetic models as well as intraparticle diffusion isotherms, moreover, estimate the parameters characterizing the performance of batch processing for the purpose of adsorption.

2. Experimental

2.1 Materials

The reagents used for the synthesis of nanosorbents in this work are ammonium metavanadate (NH_4VO_3, 99.99%), nitric acid (HNO_3, 99%), cetrimonium bromide (CTAB, $C_{19}H_{42}BrN$, 99%), ethanol (CH_3CH_2OH, 99.8%), cerium(IV) sulfate tetrahydrate ($Ce(SO_4)_2 \cdot 4H_2O$, 99%), urea (NH_2CONH_2, 99%), polystyrene (99%), polyethylene (99%), iron trichloride ($FeCl_3.6H_2O$, 99%), iron sulfate ($FeSO_4.7H_2O$, 99.7%), n-hexane (99%), toluene (99%) and poly-n-isopropylacrylamide-co-butylacrylate (PNIPAM, 99%) were purchased from Merck Kft., Budapest; titanium tetrachloride ($TiCl_4$, 99.8%) from Sigma-Aldrich Kft., Hungary; hydrochloric acid (HCl, 99.7%), sodium hydroxide (NaOH, 99.0%) and sulfuric acid (H_2SO_4, 99.7%) from VWR International Kft., Debrecen, Hungary and kerosene (EU number: 649-423-00-8) was obtained from Servind Budapest–Hungary Kft. Commercial MWCNTs (TNNF-6 type, Timesnano, Chengdu, China) made by chemical vapor deposition (CVD) were used in this research.

2.2 Preparation of nanoadsorbents

2.2.1 Synthesis of the metal oxide nanoparticles of V_2O_5 at different annealing temperatures and the preparation of TiO_2 and CeO_2 nanoparticles

Vanadium pentoxide (V_2O_5) was prepared by hydrothermal methods (reflux) [176] using ammonium metavanadate, ethanol (EtOH), nitric acid, cetyltrimethylammonium bromide (CTAB) and distilled water according to the reported method. At first, 0.1 g of NH_4VO_3 and 0.1 g of CTAB were dissolved in a mixture of distilled water and ethanol (100 mL) in the ratio of 7:3, respectively before HNO_3 was added very slowly whilst continuously being stirred until the pH value became 2.5. The mixture above was heated under reflux for 6 h at 80 °C. The precipitate was washed with distilled water 10 times before being washed with ethanol before being dried in an oven at 90 °C for 60 min and annealed at 250, 500 and 750 °C for 4 h each. Equations 1 and 2 describe the chemical reactions used to prepare vanadium pentoxide. The hydrothermal method used to prepare metal oxide nanoparticles is presented in Figure 13.

$$2NH_4VO_3 + 2HNO_3 + nH_2O \xrightarrow[\text{CTAB}]{CH_3CH_2OH} V_2O_5nH_2O + 2NH_4NO_3 + H_2O \quad (1)$$

$$V_2O_5nH_2O \xrightarrow{\Delta} V_2O_5 + nH_2O \quad (2)$$

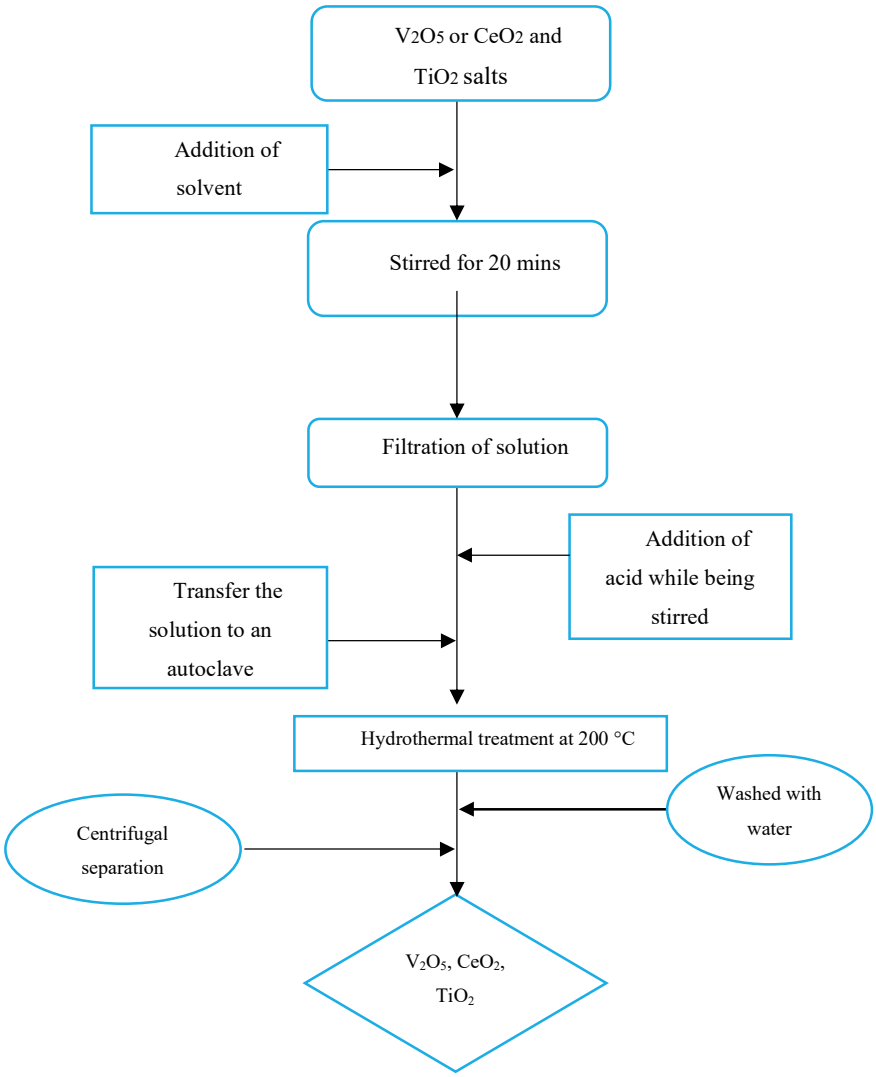

Figure 13. Hydrothermal method for the preparation of metal oxide nanoparticles

TiO_2 nanoparticles were prepared using titanium tetrachloride, potassium hydroxide, ethanol and distilled water [160]. 5 mL of titanium tetrachloride was poured into a round-bottom flask in a cold water bath and 75 mL of ethanol was added whilst being stirred until the reaction stabilized before 25 mL of water was added while stirring continued. 3 g of potassium hydroxide was added until the pH of the solution became 1.5. The solution was placed into an autoclave and maintained at 200 °C for 9h before the sample was annealed at 500 °C. The reactions are presented in Equations 3 and 4:

$$TiCl_4 + 3CH_3CH_2OH/H_2O \xrightarrow{\text{KOH / Autoclave}} 4HCl + Ti(OH)_4 + 3CH_2CH_2 \quad (3)$$

$$Ti(OH)_4 \xrightarrow{\Delta} TiO_2 + 2H_2O \quad (4)$$

Cerium dioxide (CeO_2) was prepared by a hydrothermal method [177] using an autoclave as well as cerium(IV) sulfate tetrahydrate, urea, CTAB and distilled water. At first, 2.34 g of $Ce(SO_4)_2 \cdot 4H_2O$, 1.39 g of NH_2CONH_2 and 2.1 g of CTAB were dissolved in 50 mL of distilled water before being mixed on a magnetic stirrer for 30 min. The materials were put into a 50 mL autoclave and maintained at 200 °C for 12h. Following this, the autoclave was left to cool down to room temperature. The $Ce(OH)_4$ obtained was washed with distilled water several times before being centrifuged and then washed again with ethanol. The sample was dried at 90 °C for 60 min and then annealed at 500 °C for 4 h. The chemical reactions used to prepare cerium dioxide are shown in Equations 5-7:

$$NH_2CONH_2 + 3H_2O \rightarrow 2NH_4OH + CO_2 \quad (5)$$

$$Ce(SO_4)_2H_2O + 4NH_4OH \rightarrow Ce(OH)_4 + 2(NH_4)_2SO_4 + 4H_2O \quad (6)$$

$$Ce(OH)_4 \rightarrow CeO_2 + 2H_2O \quad (7)$$

The composites V_2O_5:CeO_2 (V:Ce) and V_2O_5:TiO_2 (V:Ti) were prepared using thermal method [177]. By mixing V_2O_5 with CeO_2 and TiO_2 in the mole ratio of 3:1, respectively, while the composite V_2O_5:CeO_2:TiO_2 (V:Ce:Ti) was prepared by mixing V_2O_5, TiO_2 and CeO_2 in the mole ratio of 3: 0.5: 0.5, respectively. Metal oxides were mixed in a beaker with ethanol for 6h on a magnetic stirrer before the mixture was placed into a furnace and annealed for 2h at 500 °C.

2.2.2 Synthesis of metal oxide-based MWCNTs nanoparticles

MWCNTs were functionalized using the concentrated acids H_2SO_4 and HNO_3 in a ratio of 2:1, respectively [177]. The process of modification was carried out using the strong oxidizing agents HNO_3 and H_2SO_4 to introduce carboxylate groups onto the MWCNTs. The mixture of concentrated acids was placed into a beaker and 2 g of MWCNTs was added before being ultrasonicated for 30 min. Following this, the mixture was transferred to a round-bottom flask to be heated under reflux for 8h at 180 °C before being diluted 15 times with distilled water, filtered by a membrane filter and washed until the pH became 7. The addition of functionality onto the surface of the nanotubes was carried out in research by metal oxides and their composite nanoparticles. 2 wt% of the prepared metal oxides TiO_2, CeO_2 and V_2O_5 as well as their mixed nanocomposites were added to MWCNTs in 70 mL of ethanol. The solution was stirred at 40 °C for 4h using a

magnetic stirrer and ultrasonicated for 30 min before being heated under reflux at 90 °C for 4h. The solution was transferred to an autoclave reactor and maintained at 200 °C for 4h. Finally, the samples were dried by evaporating off the ethanol at 85 °C. The preparation steps of metal oxide nanoparticle-modified MWCNTs are presented in Figure 14.

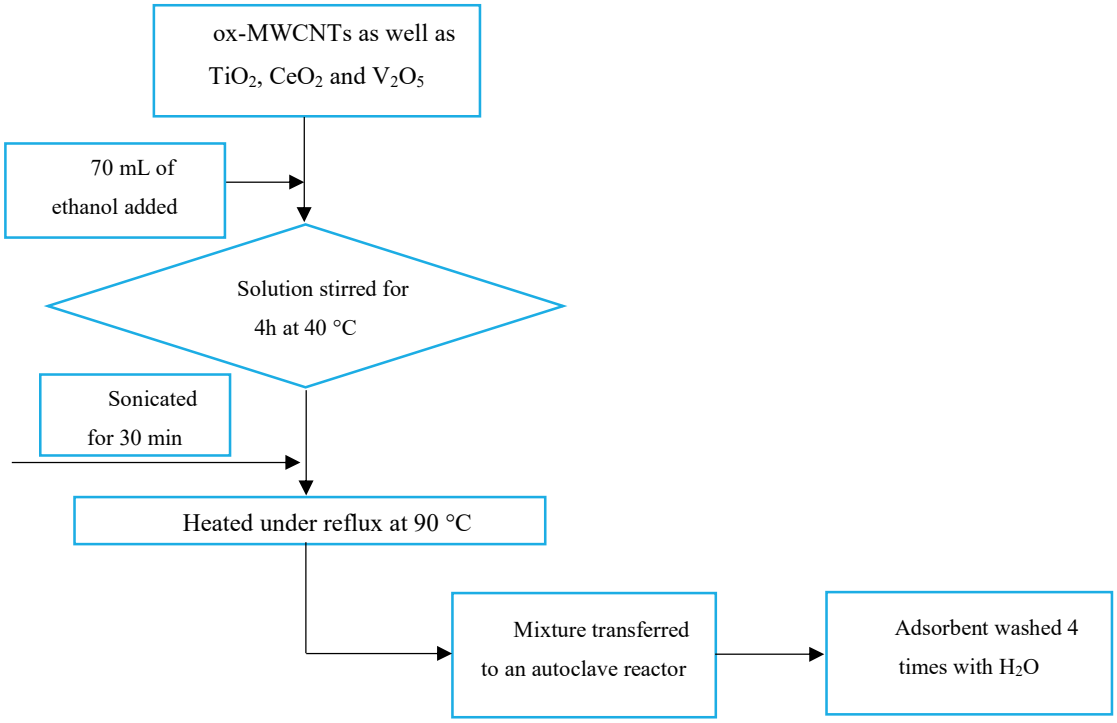

Figure 14. Preparation of CeO_2 or TiO_2 or V_2O_5 or their composites doped MWCNTs by the hydrothermal method

2.2.3 Preparation of polymer-modified Fe_3O_4/MWCNTs

Fe_3O_4 doped MWCNTs (Fe/MWCNTs) nanocomposites were prepared by using the following process: two solutions, Fe^{3+}: $FeCl_3.6H_2O$ and Fe^{2+}: $FeSO_4.7H_2O$, having a molar ratio of 2:1, respectively, were mixed. To prevent the magnetite from agglomerating, CTAB was added to the mixture of iron salts. MWCNTs were added to the mixture while continuously being stirred at 40 °C until the solution resembled that of clay. Nitrogen gas was pumped through during the process to prevent the oxidation of Fe^{2+} to Fe^{3+}. A solution of ammonium hydroxide was added to the mixture drop by drop until the pH of the solution reached 10. The resultant Fe/MWCNTs were washed and dried at 50 °C using a vacuum oven for 12h [178]. The formation of Fe/MWCNTs composites is presented by Equation 8.

$$2FeCl_3.6H_2O + FeSO_4.7H_2O + 8NH_4OH + MWCNTs \xrightarrow{\Delta} MWCNTs{:}Fe_3O_4 + 6NH_4Cl + (NH_4)_2SO_4 + 23H_2O \quad (8)$$

Chloroform, xylene and water were used to dissolve polystyrene (PS), polyethylene (PE) and poly-n-isopropylacrylamide-co-butyl acrylate (PNIPAM), respectively. At first, 100 mg of Fe/MWCNTs per litre of solution was sonicated at 50 °C for 1h before polymers were added to the mixture in a 1:3 polymers:Fe/MWCNTs weight ratio. The mixtures were sonicated for a further 3 h before being mixed by a magnetic stirrer for 24h at 40 °C using a hot plate [179]. Finally, PS:Fe/MWCNTs, PE:Fe/MWCNTs and PNIPAM:Fe/MWCNTs nanocomposites were formed. The samples were separated, washed and then dried at 50 °C overnight. The magnetic property of the prepared nanoadsorbent was successfully achieved. Figure 15 presents a schematic flow diagram showing the preparation of the PS:Fe/MWCNTs nanocomposites. The mechanisms for the synthesis of polymer-modified Fe/MWCNTs is presented in Figure 16.

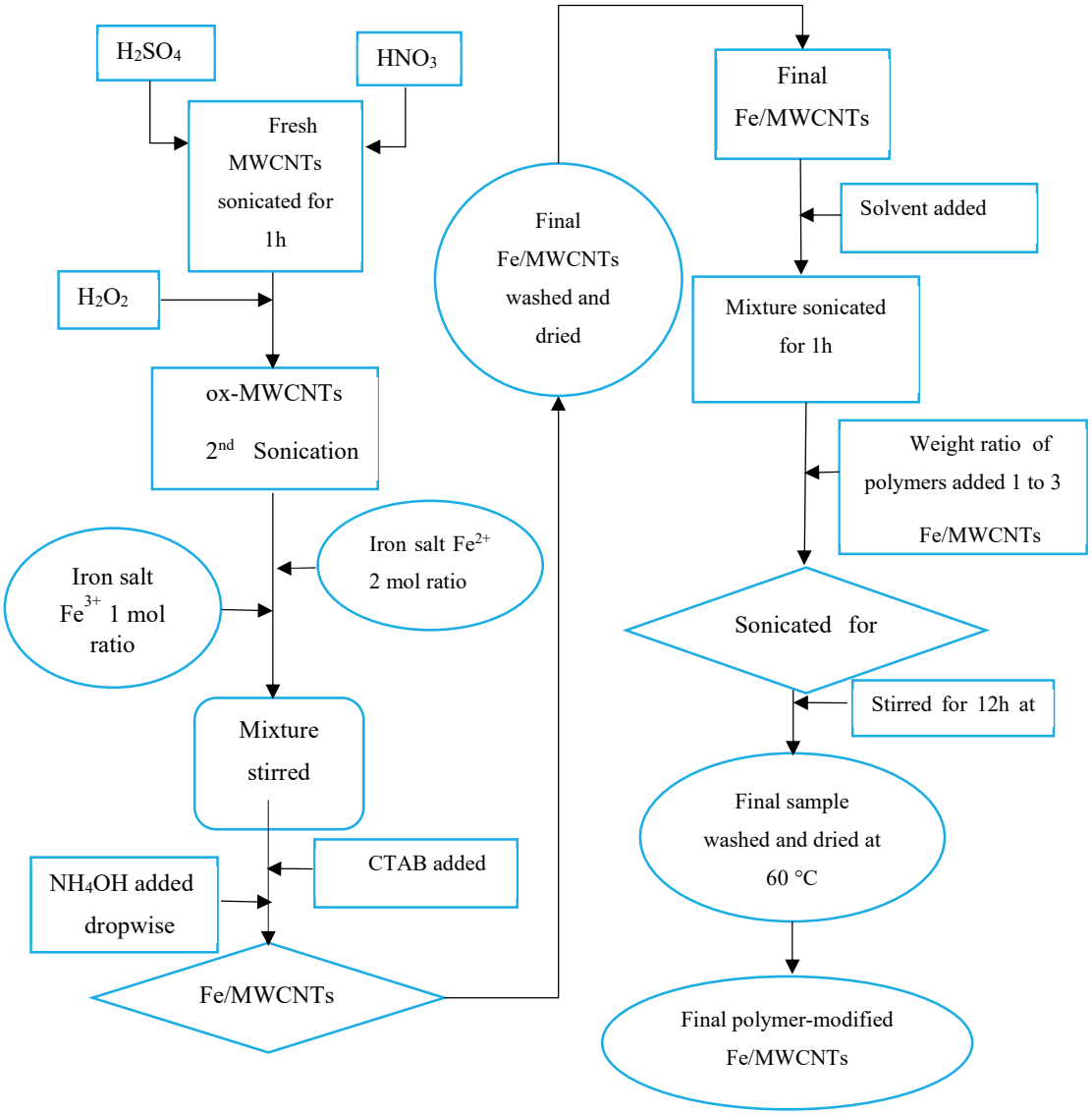

Figure 15. Schematic flow diagram showing the synthesis of polymer-modified Fe/MWCNTs

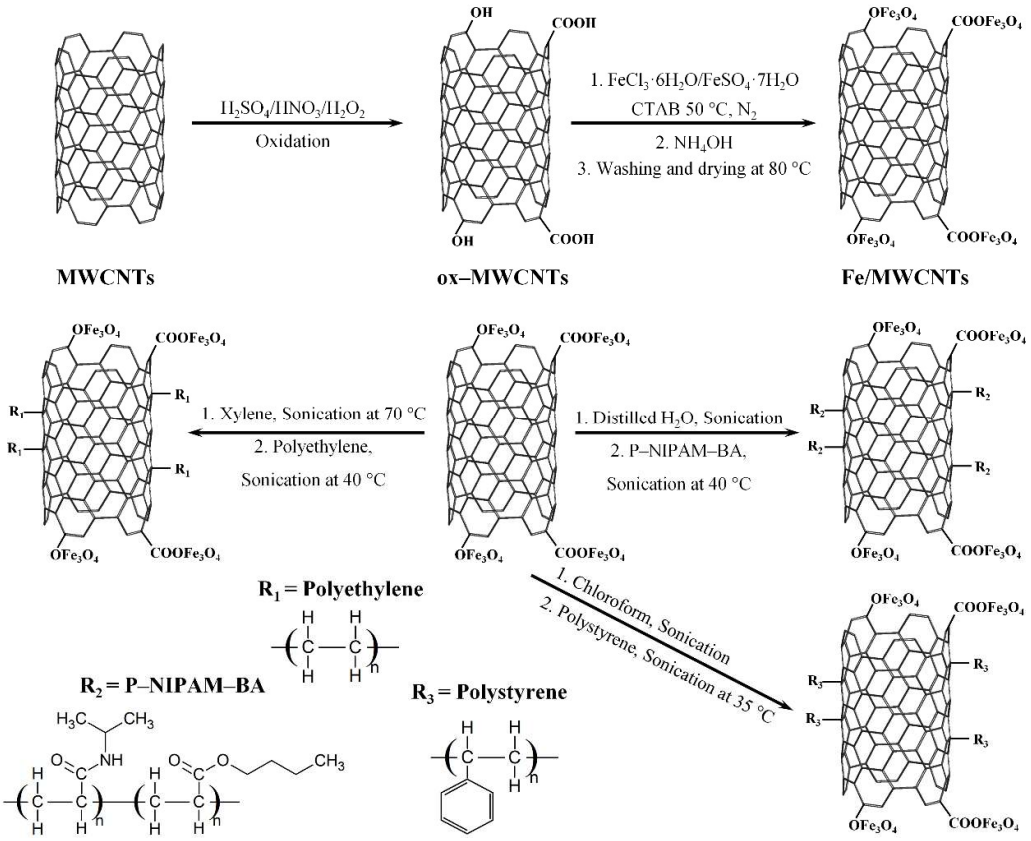

Figure 16. Mechanism for the synthesis of polymer (polyethylene, polystyrene and PNIPAM)-modified Fe/MWCNTs

2.3 Characterization methods

The physicochemical properties of the adsorbents were examined using several characterization techniques to obtain information about the structural, chemical and surface properties of the prepared adsorbents such as X-ray diffraction (XRD), Fourier transform infrared spectroscopy (FTIR), Raman spectroscopy, Brunauer–Emmett–Teller (BET) method, scanning electron microscopy (SEM), transmission electron microscopy (TEM), energy-dispersive X-ray spectroscopy (EDX), atomic force microscopy (AFM) and thermogravimetric analysis (TGA).

2.3.1 X-ray diffraction measurements

Identification of the solid crystalline phases in the samples was determined by X-ray diffraction analysis (XRD) using a Philips PW3710 X-ray diffractometer equipped with

Cu-Kα radiation (λ = 0.1541 nm) and recorded at room temperature over an angular range (2θ) of 4–70° with a scanning acquisition speed of 0.02 °/s.

2.3.2 Atomic force microscopy measurements

Atomic Force Microscopy (AFM) analysis was carried out using a SPM-AA (scanning probe microscopy) 3000-type instrument. AFM was used to probe the sample surface on the nanometer scale in order to investigate its roughness and particle size distribution. The samples were dissolved in ethanol and transferred onto a glass plate 0.5 mm × 0.5 mm in size for analysis.

2.3.3 Fourier transform infrared spectroscopy measurements

Fourier transform infrared (FTIR) spectroscopic measurements were carried out by a Bruker VERTEX 70v spectrometer with a Bruker Platinum ATR adapter on the surface of the samples without additional manipulation of the sample. The spectra were recorded within the range of 400 to 4000 cm^{-1} at a resolution of 2 cm^{-1} and at room temperature with a DTGS detector by averaging 512 scans.

2.3.4 Raman spectroscopy measurements

Raman spectra were recorded using a Bruker RFS 100/S FT Raman spectrometer with a Nd:YAG laser source (1064 nm, 30 mW) and a liquid N_2-cooled Ge detector. The signal-to-noise ratio was improved by the coaddition of 2048 spectra with a resolution of 4 cm^{-1}. The spectral deconvolution of the baseline corrected Raman spectra was achieved by fitting a mixture of Gaussian and Lorentzian line shapes using PeakFit software (v4.12, Seasolve, Systat Software Inc., San Jose, CA, USA).

2.3.5 Low-temperature nitrogen gas adsorption

The specific surface area, pore volume and pore-size distribution within various ranges of diameters micropores (1.7–2.0 nm), mesopores (2–50 nm) and macropores (50–100 nm) - were determined by nitrogen adsorption/desorption isotherms at −196 °C using an ASAP 2000 analyzer manufactured by Micromeritics, Norcross, GA, USA. The specific surface areas of the samples were determined by the BET (Brunauer–Emmett–Teller) method from the corresponding nitrogen adsorption isotherms. The pore-size distribution and pore volumes were calculated from the nitrogen desorption isotherms using the BJH (Barret– Joyner–Halenda) model.

2.3.6 Scanning, transmission electron microscopy and energy-dispersive X-ray spectroscopy measurements

The morphology of the surface of the nanocomposites was studied using transmission electron microscopy (TEM) and scanning electron microscopy (SEM) techniques. The nanocomposites for TEM were prepared by depositing a drop of nanocomposites suspended in ethanol on copper grids covered by an amorphous lacey carbon support film. SEM and TEM analyses were performed using a Thermo Fisher Scientific Apreo S LoVac SEM in the Czech Republic operated at 2.0 kV for backscattered electron imaging and at 30.0 kV for transmission electron imaging, equipped with an AMETEK Octane Elect Plus energy-dispersive X-ray spectrometer (EDX) (Berwyn, PA, USA).

2.3.7 Thermogravimetric analysis measurements

Thermoanalytical measurements (TG/DTG) were carried out using a NETZSCH TG 209-type thermobalance. Samples were measured in ceramic crucibles. The TG/DTG curves were recorded while heating the samples to 1000 °C (at a heating rate of 10 °C/min) in a dynamic argon gas flow (99.998%).

2.4 Adsorption experiments

2.4.1 Methylene blue adsorption study by UV-Visible spectroscopy

Metal oxide nanoparticles (V_2O_5) were prepared at different annealing temperatures using fresh MWCNTs, Ce/MWCNTs, V/MWCNTs, V:Ti/MWCNTs, V:Ti:Ce/MWCNTs and V:Ce/MWCNTs for the removal of MB by adsorption from water. The maximum absorbance of a MB solution in water (MB concentration: 20 mg/L) was monitored by a NANOCOLOR UV-Vis spectrophotometer (MACHEREY-NAGEL, Germany) within the range of 400 to 700 nm. The maximum absorbance was observed at λ_{max} = 665 nm as shown in Figure 17a. A stock solution was used to prepare the calibration solution for UV–Vis spectroscopy at different MB concentrations (4, 8, 12, 16, 18 and 20 mg/L) to prepare the plot of the MB absorbance as a function of MB concentration as shown in Figure 17b.

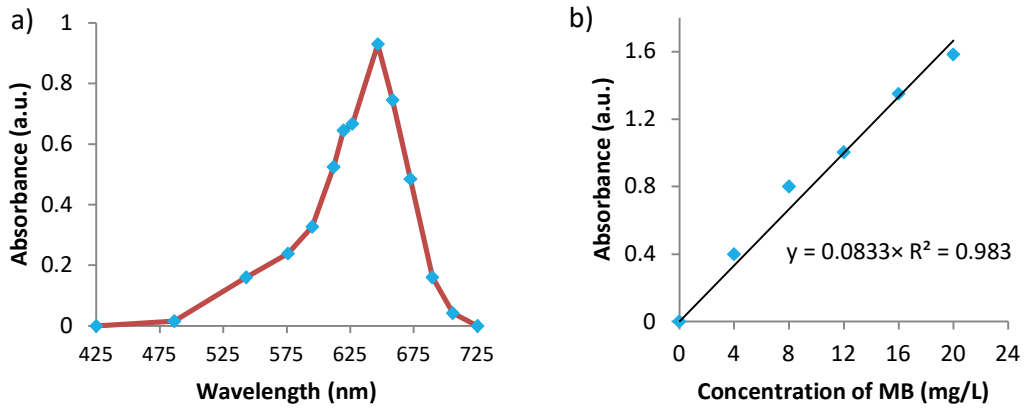

Figure 17. UV-Vis absorption spectrum of the (a) MB solution and (b) standard calibration curve of MB solutions at different concentrations at 665 nm

MB stock solutions were diluted with distilled water. The pH of the dye solution was set at the desired pH of 7 using 0.1 M NaOH or 0.1 M HCl. For each experiment, 30 mL of MB solution (20 mg/L) was extracted and 20 mg of metal oxide was added to the solution. The removal efficiency of MB was studied as a function of contact time, adsorbent dosage and temperature in order to determine the optimum conditions for the removal of MB from water. Once the reaction had finished, the samples were stockpiled and taken for separation. The dye concentration in the supernatant was checked using the UV-Vis spectrometer at 665 nm [180].

2.4.2 Kerosene adsorption study by gas chromatography

The adsorption tests over fresh MWCNTs, Ce/MWCNTs, V/MWCNTs, V:Ce/MWCNTs, Fe/MWCNTs and PNIPAM:Fe/MWCNTs nanoadsorbents were carried out with kerosene cut to study the efficiencies with regard to the removal of hydrocarbons from samples of water. Adsorption experiments were carried out in batch mode at room temperature. The model contaminated stock solution was made in a laboratory using a kerosene concentration of 500 mg/L in distilled water. The 50 mL of model solutions were mixed for 20 min using a magnetic stirrer before 5 mg of the adsorbent was added. Then each solution was shaken for between 15 and 60 min at room temperature. The adsorbent was separated from the solution by filtration. The filtered aqueous solution was used for the extraction step to prepare the sample for gas chromatography (GC) for the purpose of determining its hydrocarbon content. The aqueous kerosene solution was extracted with 20 mL of hexane and shaken at a rotational speed of 240 rpm for 30 min. The hexane fraction was dried with Na_2SO_4 powder. The blank solution was prepared by

the same method without adding any adsorbent. The kerosene-hexane samples were analyzed by an Agilent 7890A Gas Chromatograph with a J&W HP-5 capillary column (30 m × 0.320 mm, 0.25 µm film thickness). A flame ionization detector (FID) was used for the analysis [177].

After each experiment, the magnetic separation of adsorbents from aqueous solutions was achieved by placing a magnet near the vessels containing samples contaminated with Fe_3O_4 components. The aforementioned separated aqueous solution collected from the adsorbent during the extraction step was used to prepare the sample for the purpose of determining the hydrocarbon content by GC.

2.4.3 Kerosene and toluene adsorption study by high performance liquid chromatography

Adsorption experiments were performed in batch mode. A stock solution of aqueous kerosene and toluene mixtures was prepared by adding kerosene or toluene to deionized distilled water. Kerosene or toluene mixtures of different concentrations were prepared to obtain a calibration curve as presented in Figures 18a and 18b.

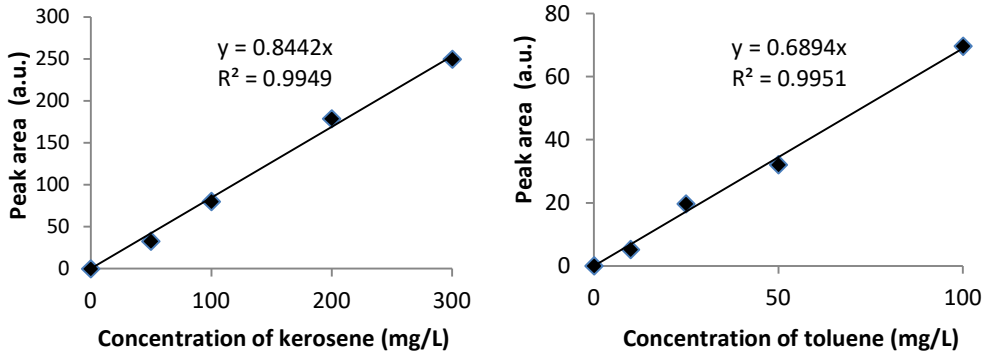

(a) **(b)**

Figure 18. Standard calibration curve for (a) kerosene solutions and (b) toluene solutions subjected to HPLC

The stock mixtures were ultrasonicated for 60 min, then stirred for 24h at 25 °C and ultrasonicated for 30 min prior to the batch adsorption experiments. For each batch experiment, 50 mL of stock mixture and 2 mg of adsorbents (fresh MWCNTs, ox-MWCNTs, Fe/MWCNTs, PE:Fe/MWCNTs or PS:Fe/MWCNTs) for kerosene or toluene adsorption were added to a 120 mL glass bottle, which was subsequently sealed with a stopper. Next, the bottles were transferred to a shaker and were shaken at 240 rpm for 120

min. The effects of several parameters, namely time, adsorbent dose, kerosene or toluene concentration, pH and solution temperature, on the adsorption process were evaluated. After the batch experiments, each glass bottle was allowed to rest for 2 min before being placed on an iron boron permanent magnet block to separate the hydrocarbon-containing adsorbent particles.

The residual mixtures were transferred to a high-performance liquid chromatography (HPLC) system (KNAUER, Germany) with a 3 μm C18 column (25 cm × 4.6 mm) using a water : methanol 30:70 v/v mobile phase with a flow rate of 1 mL/min [181]. A blank experiment without an adsorbent was also performed to ensure that the decrease in kerosene or toluene concentrations was not related to the reduction in the concentration of hydrocarbons as a result of being adsorbed on the glass walls or vapourising due to their high volatility.

The removal efficiency of kerosene, toluene and MB (RE%) as well as the quantity of pollutants adsorbed (q_t) were calculated by Equations (9) and (10), respectively:

$$RE = \left(\frac{C_0 - C_t}{C_0}\right) \cdot 100\ \% \tag{9}$$

$$q_t = \frac{(C_0 - C_t)}{m} \cdot V \tag{10}$$

where C_0 denotes the initial pollutant concentration, mg/L; C_t stands for the final pollutant concentration at time t, mg/L; q_t represents the adsorption capacity at time t, mg/g; V refers to the volume of pollutant solution, L; and m is the mass of the adsorbent, g. Each experiment was performed in triplicate under identical conditions and the mean values were calculated and reported here.

2.5 Kinetics studies and adsorption isotherms

The interactions between the sorbents and adsorbents are explained by a few theoretical approaches such as equilibrium isotherms and adsorption kinetics. Adsorption equilibria explain the physicochemical processes involved in sorption and kinetic measurements [182]–[184]. Furthermore, they explain the extent of the transport mechanism of wastewater pollutants into the adsorbent which is comprised of the external mass transfer of the sorbate from the bulk solution to the surface of the sorbent, the internal diffusion of the sorbate to the adsorption site and the overall adsorption process [180]-[181]. The kinetic models are relatively efficient when determining the rate at which the adsorbent efficiently removes the adsorbate such as kerosene. In order to ascertain reproducible results, three different kinetic models, namely pseudo first-order,

pseudo second-order and intraparticle diffusion, were applied to study the adsorption kinetics of pollutants on prepared and modified sorbents.

The pseudo first-order reaction rate constant was calculated by Equation (11):

$$log(q_e - q_t) = log\, q_e - k_1 \frac{t}{2.303} \quad (11)$$

where qe and qt denote the amount of kerosene adsorbed (mg/g) at equilibrium and at time t (min), respectively, while k_1 stands for the pseudo first-order rate constant (min^{-1}).

A pseudo second-order reaction rate constant based on the equilibrium capacity of adsorption is given by Equation (12):

$$\frac{t}{q_t} = \frac{1}{k_2 q_e^2} + \frac{t}{q_e} \quad (12)$$

where k_2 denotes the equilibrium rate constant of pseudo second-order adsorption (g/mg min).

The third kinetic model, that is, intraparticle diffusion based on the theory proposed by Weber and Morris, was used to identify the diffusion mechanism. The initial rate of intraparticle diffusion is expressed by Equation (13):

$$q_t = k_d \times t^{\frac{1}{2}} + I \quad (13)$$

where k_d denotes the intraparticle diffusion rate constant (mg/g $min^{1/2}$) and *I* represents the intercept.

To study the equilibrium isotherm, Langmuir and Freundlich isotherm models were used. The Langmuir isotherm model is used to describe monolayer and homogeneous adsorption processes, because it hypothesizes that adsorbents form a one-molecule-thick layer at fixed, identical and equivalent sites on the surface of the adsorbent. The Langmuir model is expressed by Equation (14):

$$\frac{C_e}{q_e} = \frac{1}{q_{max}} C_e + \frac{1}{q_{max}\, b} \quad (14)$$

where Ce (mg/L) and qe (mg/g) denote the residual pollutant concentration in the solution and the amount of the pollutant adsorbed on the sorbent at equilibrium, respectively; q_{max} (mg/g) represents the maximum amount of the pollutant per unit mass of sorbent and b stands for the Langmuir adsorption equilibrium constant related to the affinity between the sorbent and pollutant.

The Freundlich isotherm model is used to describe non-ideal as well as reversible adsorption processes and is not limited to monolayer adsorption. Therefore, the Freundlich isotherm model is used to describe multilayer adsorption processes with a non-uniform distribution of the heat and sites of adsorption at different affinities on

heterogeneous adsorbent surfaces. The Freundlich isotherm model is expressed by Equation (15):

$$ln\, q_e = ln\ K_f + \frac{1}{n}\, ln\, C_e \quad (15)$$

where K_f and n denote the Freundlich adsorption constant (mg/g) and adsorption intensity, respectively.

3. Results and Discussion

3.1 Results of V_2O_5 nanoparticles at different annealing temperatures

3.1.1 FTIR results

FTIR spectra of V_2O_5 samples prepared at 90 ºC and annealed at 250, 500 and 750 ºC were recorded within the wavenumber range of 4000 to 400 cm^{-1} for functional groups and chemical bonds which are presented in Figure 19. The appearance of the FTIR bands at two different wavenumbers (3212 and 1661 cm^{-1}) correspond to O-H stretching and bending vibrations, respectively. The intensity of the bands decreased as the annealing temperature increased. The characteristic peaks at 1020, 827, 615 and 479 cm^{-1} correspond to the stretching vibrations of terminal oxygen bonds (V=O), the vibrations of doubly coordinated oxygen (bridging oxygen) bonds (V-O-V), as well as the asymmetric and symmetric stretching vibrations of triply coordinated oxygen (chain oxygen) bonds, respectively [187].

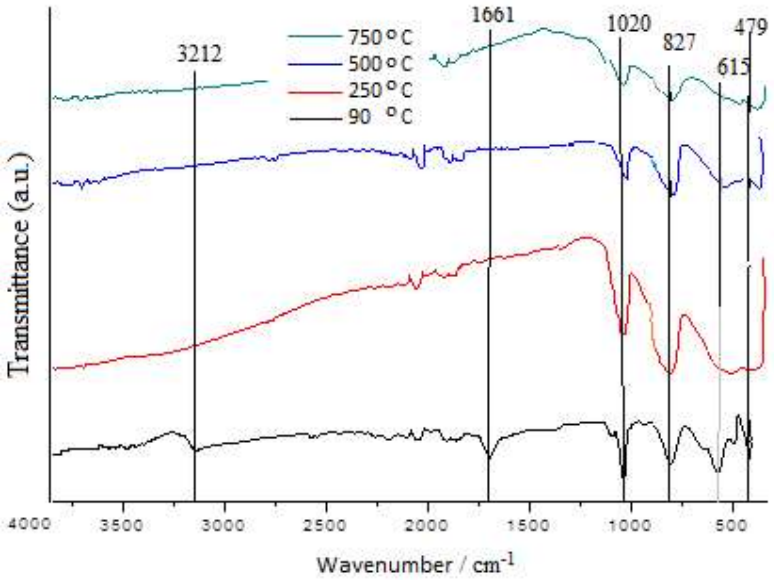

Figure 19. FTIR spectra of V_2O_5 samples prepared at 90 ºC and annealed at 250, 500 and 750 ºC

3.1.2 X-ray diffraction results

XRD techniques were used to investigate the crystallinity of the newly prepared nanomaterials. The XRD patterns of V_2O_5 nanomaterials treated at increasing temperatures of 90, 250, 500 and 750 ºC, respectively are presented in Figure 20. The major diffraction peaks of V_2O_5 appear at 2θ = 15.62º, 20.04º, 21.80º, 31.40º and 40.90º,

which correspond to (200), (010), (101), (301) and (002) reflections, respectively [23], [27]. These peaks relate to the shcherbinaite orthorhombic crystalline structure of vanadium pentoxide (JCPDS Card No. 41-1426). By increasing the pretreatment temperature from 250 to 750 ºC, the intensity of diffraction peaks increased. Based on the Scherrer equation, the mean size of treated V_2O_5 nanomaterials was calculated to be approximately 20 nm.

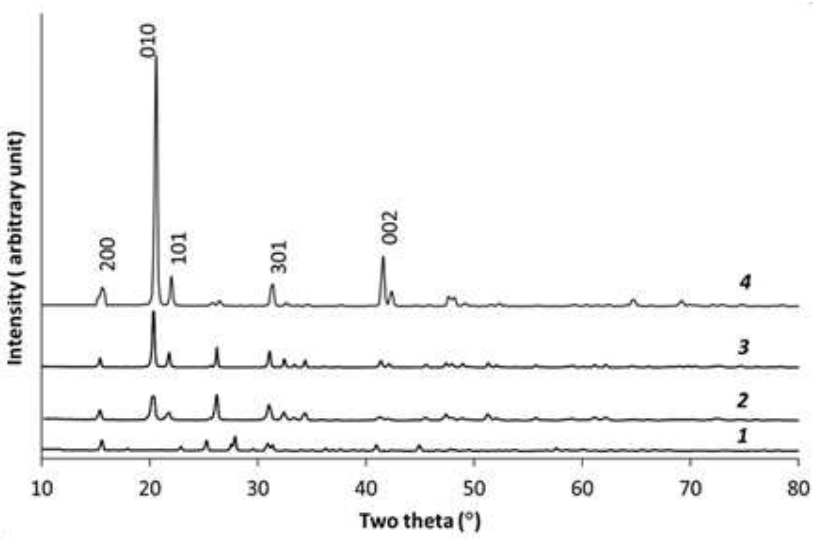

Figure 20. XRD patterns of the V_2O_5 nanoparticles treated at different temperatures: 1 - V_2O_5 as prepared, 2 - V_2O_5 treated at 250 °C, 3 - V_2O_5 treated at 500 °C, 4 - V_2O_5 treated at 750 °C

3.1.3 UV-Visible spectroscopy results

The UV–Vis absorption spectra of V_2O_5 samples were recorded using ethanol as a solvent (0.001 M). UV-Vis optical properties within the range of 200–800 nm at various temperatures (90, 250, 500 and 750 °C) exhibited temperature-dependent absorbance as shown in Figure 21. The absorption peaks of "the prepared sample" of V_2O_5 appear around 486 nm (Eg = 2.55 eV). The energy gap increased to 471 nm (Eg =2.63 eV) when the sample was annealed at 250 °C, while it decreased to 500 nm (Eg =2.48 eV) when annealed at 500 °C. On the other hand, the energy gap also increased to 484 nm (Eg =2.56 eV) when the sample was annealed at 750 °C. All these results were calculated according to the equation in reference [188]. By increasing the annealing temperature, the phase change of the vanadia nanoparticles occurred from amorphous to crystalline. A blue shift of the absorption spectra occurred at annealing temperatures from 250 to 500 °C, while a

red shift was observed between 500 and 750 °C. This phenomenon is the Burstein-Moss effect [184]-[185].

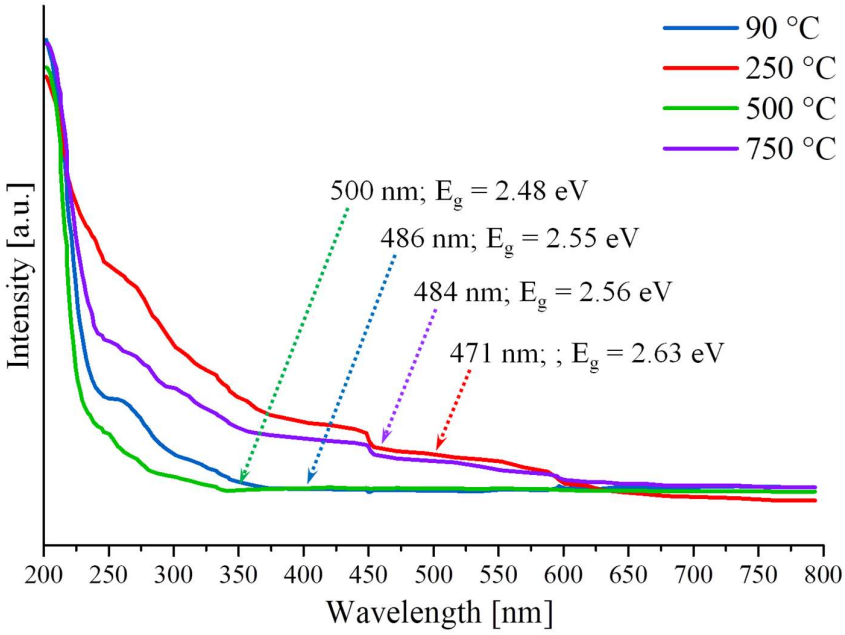

Figure 21. UV-Vis spectra of prepared V_2O_5 nanoparticles at 90 ºC and annealed at 250, 500 and 750 ºC

3.1.4 Scanning electron microscopy results

The Scanning Electron Microscopy results were studied to determine the morphology of the nanoparticles. The SEM images of the V_2O_5 nanoparticles pretreated at 500°C are shown in Figure 22, indicating that V_2O_5 particles appeared in the form of nanoflakes.

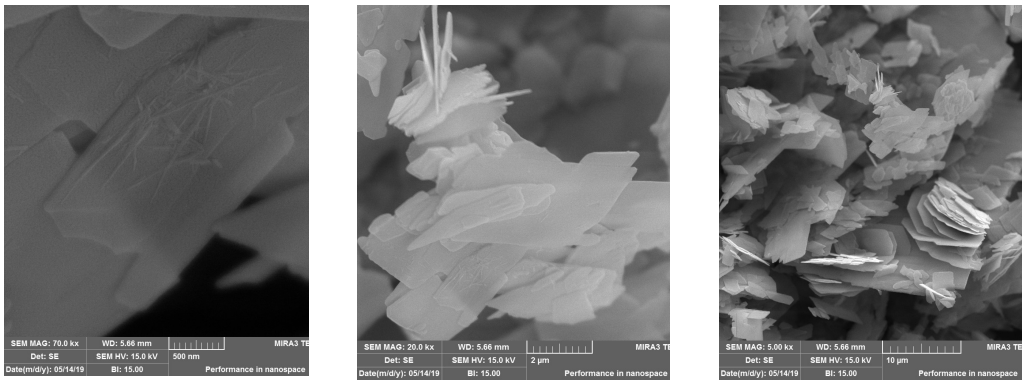

a *b* *c*

Figure 22. SEM images of V_2O_5 nanoparticles annealed at 500 ºC at resolutions of (a) 500 nm, (b) 2 µm and (c) 10 µm

3.1.5 Results of thermogravimetric analysis

The obtained V_2O_5 nanoparticles were studied by thermogravimetric analyses within a temperature range of 23 to 850°C at a heating rate of 5°C/min. The structure of the sample studied was predominantly amorphous with some crystalline phases of $(NH_4)_2V_6O_{16}$ as confirmed by XRD analysis. The mass of the sample at the beginning of the analysis was 62.2 mg. The measurements were taken in a dynamic synthetic airflow to determine the thermal stability and crystallization temperature of the sample. The decomposition curves of V_2O_5 nanoparticles are given in Figure 23, and data concerning the reduction in mass are given in Table 2. According to Figure 23, the thermal analysis of V_2O_5 nanoparticles as well as the TGA and DTG curves indicated five stages from room temperature up to 850 ºC [186]-[187].

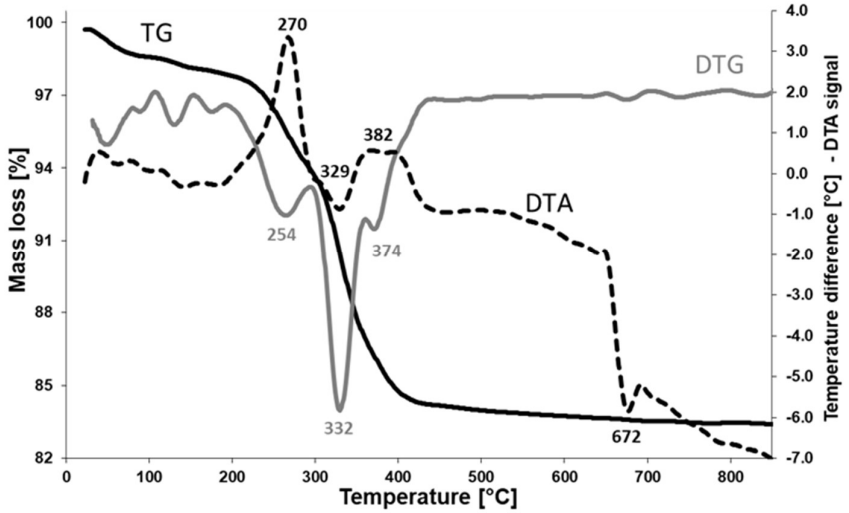

Figure 23. Thermogravimetric curves (TG/DTG/DTA) of vanadium pentoxide

Table 2. Data concerning the reduction in mass from the thermogravimetric measurements

Stage	$T_{initial}$ (°C)	T_{max} (°C)	T_{final} (°C)	Mass loss (m%)	Reduction in mass due to…
1	23	-	200	1.9	Dehydration
2	200	254	293	3.9	removal/oxidation of compounds used during preparation
3	293	332	355	6.6	decomposition of $(NH_4)_2V_6O_{16}$ to V_2O_5
4	355	374	450	3.2	the initiation of crystallization
5	450	-	850	0.8	crystallization and/or decomposition of bulk impurities
	Sample mass: 62.2 mg			**Total reduction in mass: 16.40%**	

3.1.6 Atomic force microscopy results

The AFM results concerning the grain size distribution on the surface of V_2O_5 at various annealing temperatures are presented in Figure 24.

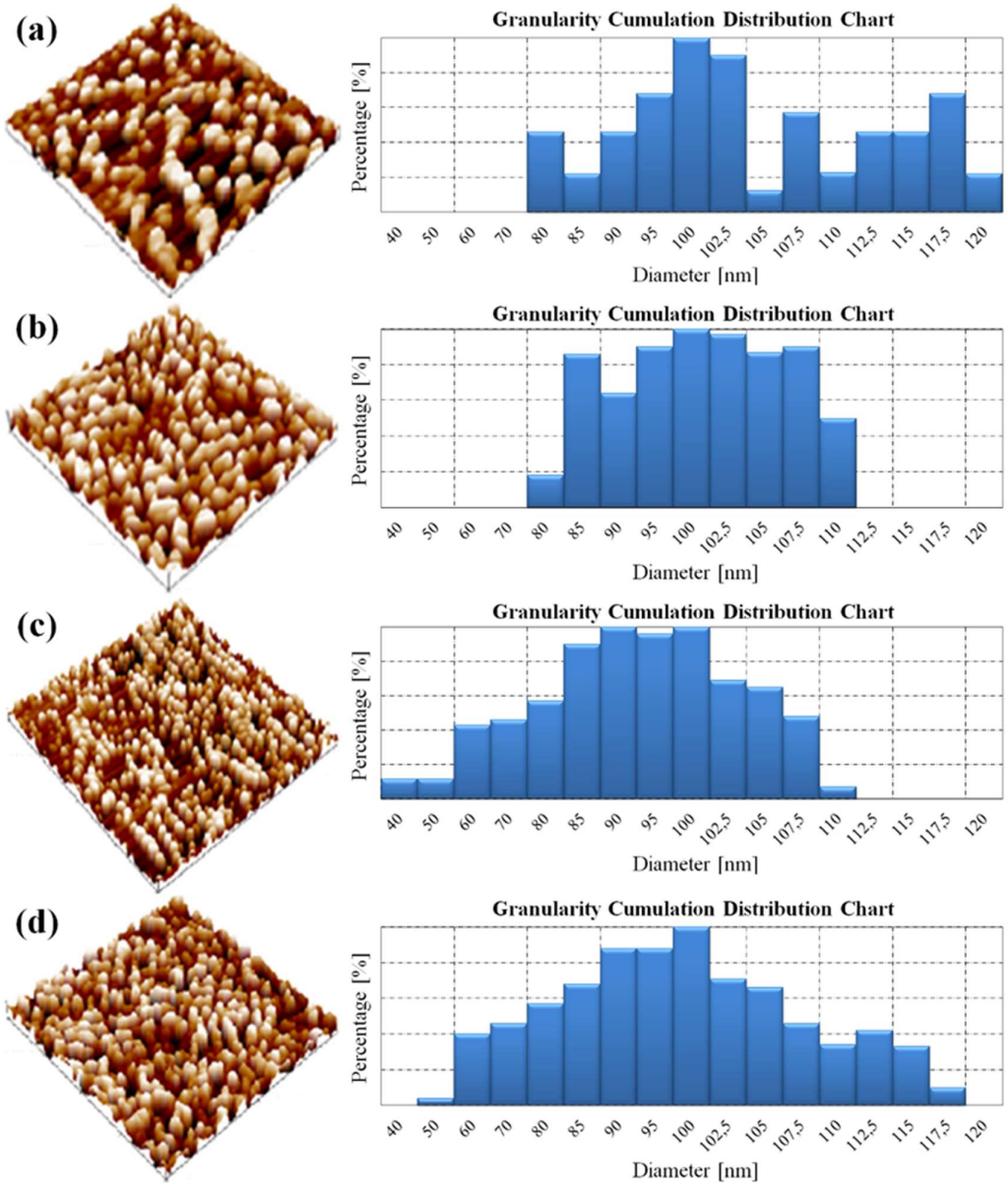

Figure 24. AFM results of V_2O_5 at annealing temperatures of (a) 90 °C, (b) 250 °C, (c) 500 °C and (d) 750 °

The average grain sizes of all samples are on the nanoscale and vary from 70 to 86 nm as shown in Table 3. It was observed that the grain size tends to reduce as the annealing temperature increases.

Table 3. Average diameter of grains found in V_2O_5 samples annealed at different temperatures

Sample	Average diameter, nm
V_2O_5 at 90°C	86.02
V_2O_5 at 250°C	78.96
V_2O_5 at 500°C	70.34
V_2O_5 at 750°C	76.17

3.1.7 Methylene blue adsorption UV-Vis results

A study was carried out on vanadium pentoxide nanoparticles that were prepared and pretreated at 250, 500 and 750 °C with contact times of between 0 and 50 min. The UV-Vis analyses were conducted at 10 min intervals. The initial MB concentration, volume of the MB solution and mass of the samples were 20 mg/L, 30 mL and 20 mg, respectively. The experiments were run at room temperature. The results are summarized in Figures 25 and 26 as well as in Table 4. The minimum MB concentration was measured following the adsorption experiment using V_2O_5 nanomaterials treated at 500 °C compared to the other samples which are shown in Figure 26.

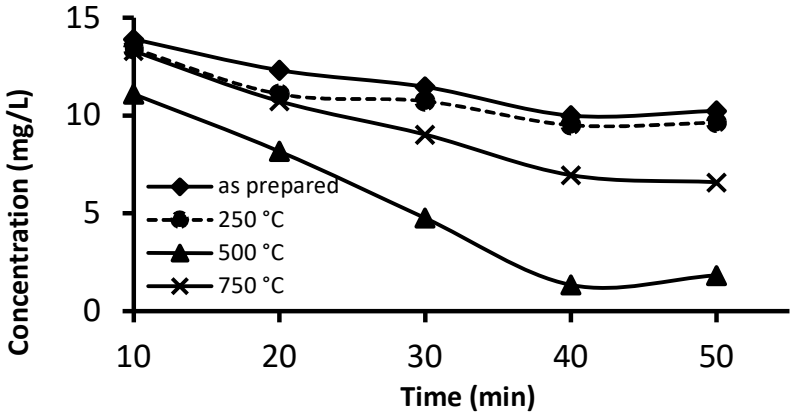

Figure 25. Change in MB concentration against time over prepared V_2O_5 nanoparticles and those annealed at different temperatures

Hence, the removal efficiency as well as adsorption capacity were also higher for V_2O_5 nanoparticles annealed at 500 °C, as is presented in Figure 26 and Table 4. In Figure 26, it can be observed that the rise in the MB removal efficiency of the studied samples was significant up to a contact time of 40 mins, after which it slowly decreased over the following 10 min.

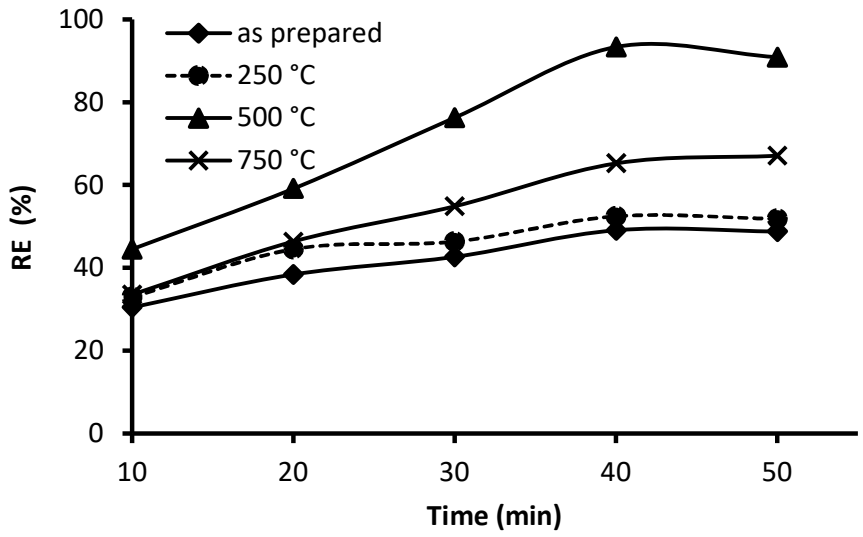

Figure 26. Removal efficiency of MB from water against time over prepared V_2O_5 nanoparticles and those annealed at different temperatures

Table 4. MB removal efficiency and adsorption capacity during MB removal from water over prepared V_2O_5 nanoparticles and annealed at 250, 500 and 750°C after 40 mins of adsorption

Adsorbents	RE (%)	q_t (mg/g)
prepared V_2O_5	49.1	15.1
V_2O_5 250°C	52.4	16.0
V_2O_5 500°C	93.1	27.2
V_2O_5 750°C	65.1	19.8

MB adsorption studied over V_2O_5 nanoparticles annealed at 500 °C exhibited the highest MB removal efficiency using the previously defined optimum contact time presented in Figures 25 and 26. Following this, the adsorption experiment was studied within the dosage range of 15 to 90 mg (Figure 27). It can be concluded that 60 mg of V_2O_5 nanoparticles annealed at 500 °C achieved the highest MB uptake from water using the following parameters: T = 40 min, C_{MB} = 20 mg/L, V = 30 mL and T = RT, which can be observed in Figure 27.

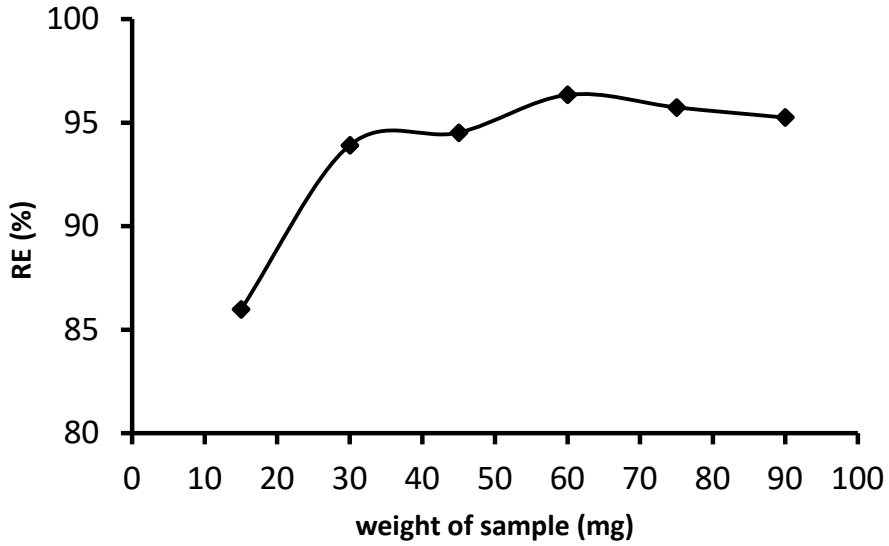

Figure 27. Effect of adsorbent dosage on MB removal over V_2O_5 nanoparticles annealed at 500°C

It was noted that when the temperature increased, the rate of removal of MB also increased and the optimum solution temperature of 45 °C yielded a higher removal efficiency (Figure 28). The optimum parameters concerning water contaminated by MB were as follows: annealing temperature of V_2O_5 = 500 °C, Time = 45 min, $T_{solution}$ =45°C, mads = 60 mg, for V = 30 mL, C = 20 mg/L and $pH_{solution}$ =7.

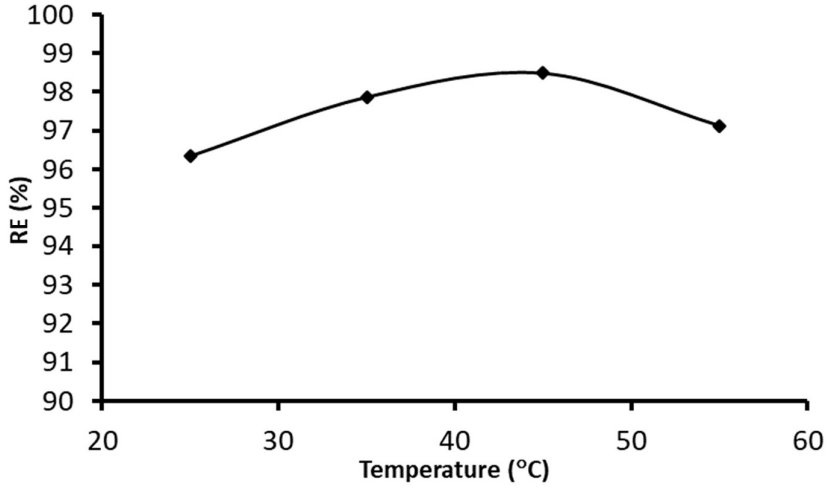

Figure 28. Effect of the solution temperature on MB removal over V_2O_5 nanoparticles annealed at 500 °C

The data given in Table 5 summarize the adsorption capacities of some of the reported adsorbent taken from the literature and compared with prepared vanadia metal oxide

nanosize annealed at 500 °C for MB removal from water. The data show that the prepared nanosorbent can be used for the adsorption of MB dye.

Table 5 Methylene blue adsorption capacities of different adsorbents

Adsorbent used	Capacity (mg/g)	Reference
V_2O_5 nanoparticles	*27.2*	*Current work*
Fe_3O_4 doped MWCNTs	15.8	[193]
Activated carbon/black cumin seeds	16.8	[194]
Activated carbon treated by sulfuric acid	16.4	[195]
Activated carbon/ rice husk	9.8	[196]
Leaginous microalga	7.8	[197]
Magnetic LDH@Fe_3O_4/PVA composites	19.5	[198]
MnO_2 nanoparticles	10.6	[199]
Biogenic ZrO_2 nanoparticles	23.2	[200]
Magnetic MWCNTs nanocomposite	15.9	[141]

3.1.8 Kinetic and isotherm studies of MB removal from water over V_2O_5 nanoparticles

The kinetic models are relatively efficient for the determination of the rate at which the adsorbent efficiently removed the adsorbate such as pollutants, including non-biodegradable dyes from wastewater [201]. Data analysis revealed that the highest adsorption and removal efficiency was achieved using V_2O_5 nanoparticles annealed at 500 °C. In order to determine the rate of removal of MB dye from wastewater, the obtained experimental data from an MB adsorption study was analysed using pseudo first- and pseudo second-order kinetic models [202]. The resulting graphs from the two kinetic models of MB adsorption are shown in Figures 29 and 30. According to Figure 29, R^2 was equal to 0.967 in the pseudo first-order kinetic model.

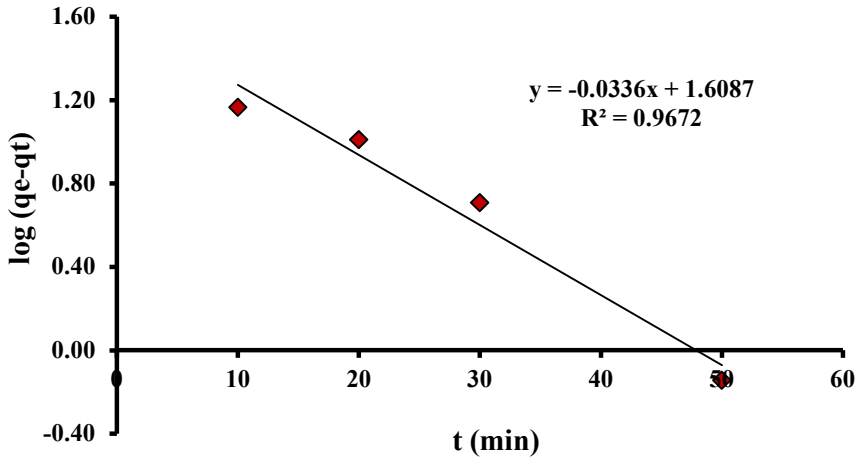

Figure 29. Pseudo-first order plot for MB adsorption onto V_2O_5 annealed at 500 °C

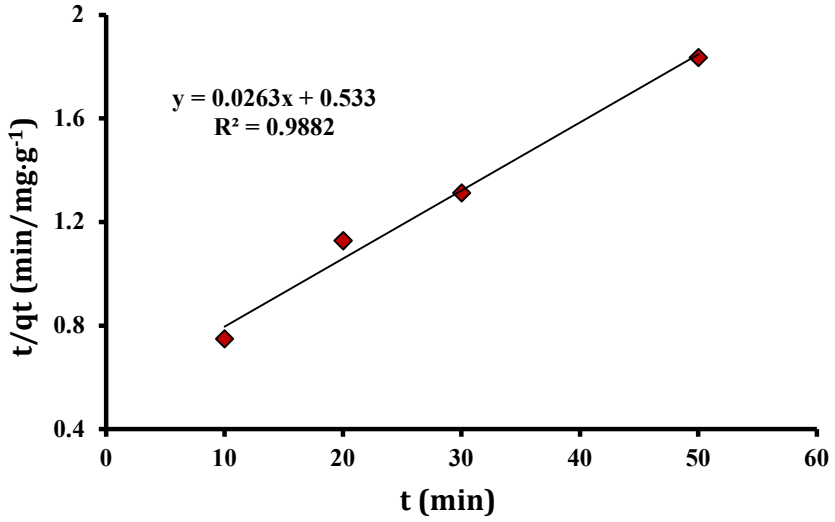

Figure 30. Pseudo-second order plot for MB adsorption onto V_2O_5 annealed at 500 °C

The statistical analysis of the adsorption data confirmed that the pseudo second-order kinetics model is the most suitable at lower solute concentrations [203]. Similarly to in the literature, the plot confirmed that the pseudo second-order kinetics model fits the best to interpret and depict the MB adsorption process with the high correlation coefficient (R^2) of 0.9882 (Figure 30). Linear regression was exhibited between the adsorbent and removal of the MB dye from wastewater as previously reported using various adsorbent materials [204]–[206].

The equilibrium adsorption isotherm was studied to evaluate and understand the behavior of methylene blue adsorption over V_2O_5 nanoparticles annealed at 500 °C. Two equilibrium adsorption models, namely Langmuir and Freundlich, were applied. An adsorption experiment was carried out using different concentrations of methylene blue dye (5.0, 7.5, 10.0, 12.5 and 15.0 mg/L) and water as a solvent at room temperature.

The resulting adsorption isotherm shows that the Freundlich model with a correlation coefficient of 0.8929 fits better as can be seen in Figures 31 and 32.

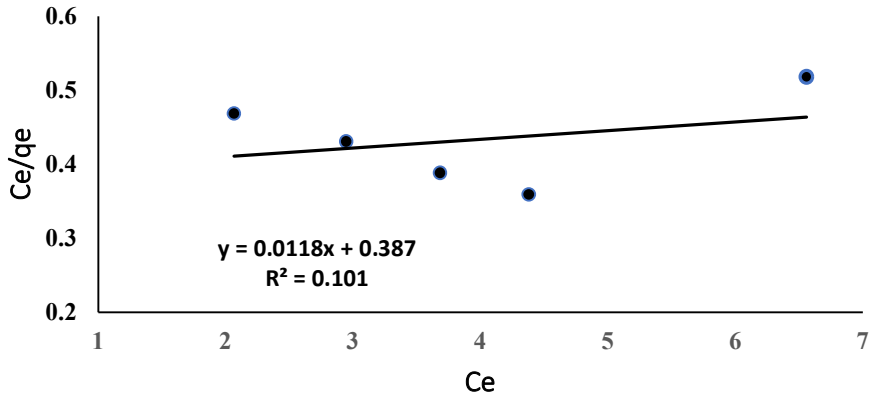

Figure 31. Langmuir isotherm models for MB adsorption onto V_2O_5 annealed at 500 °C

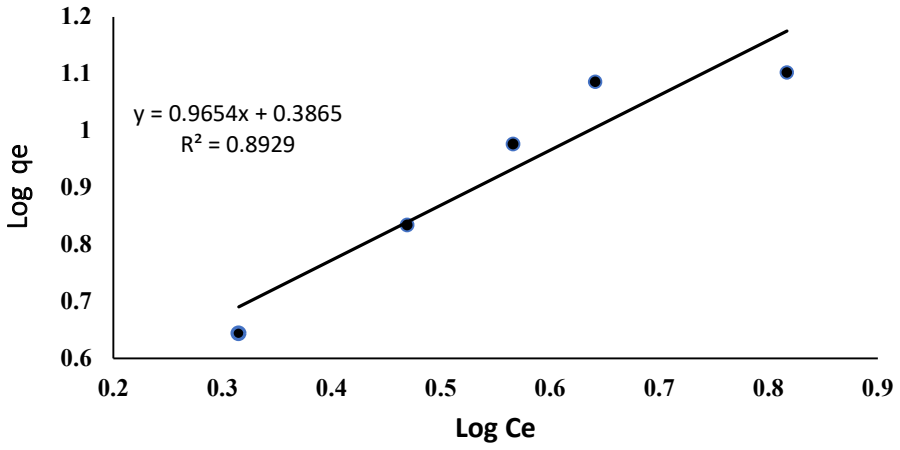

Figure 32. Freundlich isotherm models for MB adsorption onto V_2O_5 annealed at 500 °C

3.1.9. Mechanism of MB adsorption on V_2O_5 nanoparticles

The sorption mechanism of MB over vanadium pentoxide nanoparticles can be understood as follows: an ionic bond forms between the negatively charged oxygen atom of the metal oxide nanomaterial and the positively charged sulfur atom in the MB molecule. This could also be a covalent bond between an electron pair of the nitrogen atom in MB and the metal atom in the metal oxide nanoparticles as represented in Figure 33. Results using metal oxides for the removal of MB from model solution show that the sample annealed at 500 °C exhibited the highest removal efficiency of MB from water. Therefore, V_2O_5, TiO_2 and CeO_2 as well as their nanocomposites prepared and annealed at 500 °C in addition to doped MWCNTs increase the removal efficiency of MB and kerosene from water, as is presented in the following section.

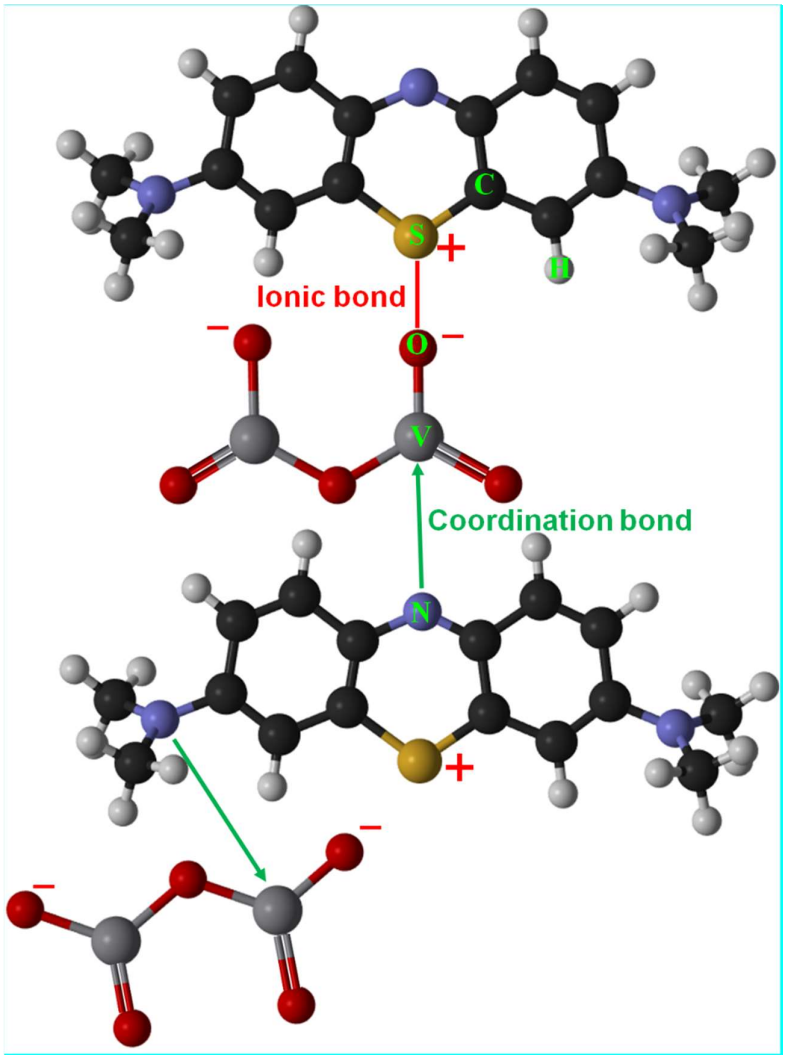

Figure 33. Proposed adsorption mechanism of MB as a result of V_2O_5 nanoparticles

3.2 Results of metal oxide-doped MWCNTs

3.2.1 Characterization of metal oxide-doped MWCNTs

3.2.1.1 FTIR results

FTIR spectra of TiO_2 nanopowders are shown in Figure 34. The spectra represent the FTIR results of the $Ti(OH)_4$ nanopowder prepared and annealed at 500 °C for 2h. A broad weak peak can be observed in the spectrum at a wavelength of approximately 3500 cm^{-1}, which can be assigned to the stretching vibration of the hydroxyl group, that is, Ti-OH of the TiO_2 nanoparticles. The bands between 630 and 532 cm^{-1} can be assigned to Ti-O stretching vibrations [207].

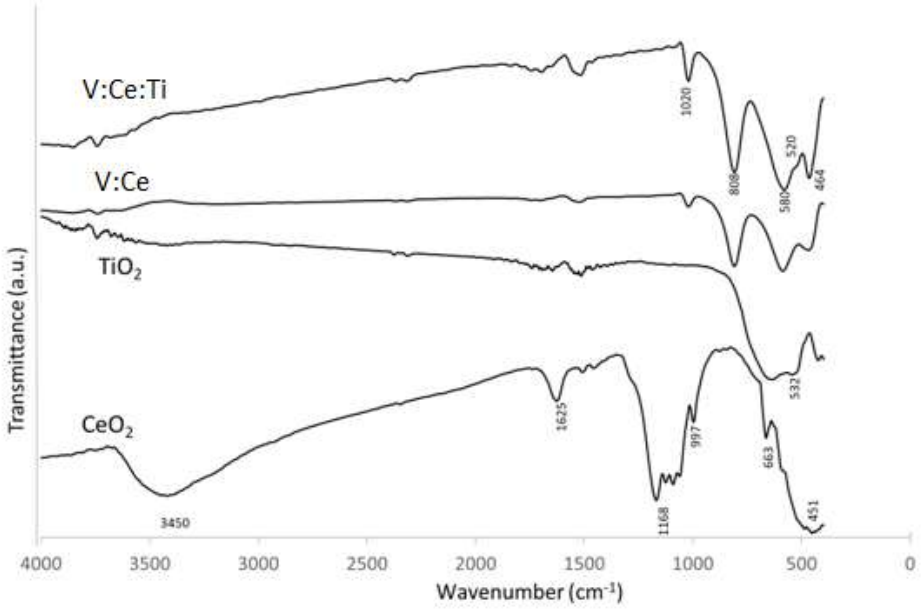

Figure 34. FTIR spectra for CeO_2, TiO_2, V:Ti, V:Ce and V:Ce:Ti composite nanopowders annealed at 500 °C

The FTIR spectra of the synthesized CeO_2 nanopowder and that annealed at 500 °C for 120 min are presented in Figure 34. The absorption bands around 3450 and 1625 cm^{-1} can be attributed to the stretching and bending vibrations of molecular water. The bands at 997 and 1458 cm^{-1} are due to bulk sulphate formation in the CeO_2. The broad band at 1168 cm^{-1} with shoulders at 1124, 1091 and 1060 cm^{-1} is due to sulphate species on the surface [208]. It was suggested that species like $CeOSO_4$ are formed due to the thermal decomposition of $Ce(SO_4)_2$ which was used during the preparation [209]. The bands at 844 and 451 cm^{-1} are related to Ce-O stretching vibrations [197]-[198].

The main peaks for V:Ce and V:Ce:Ti composites can be observed in Figure 34 at about 1020, 808 and 580 cm^{-1} which can be assigned to V=O stretching as well as V-O-V asymmetric and V-O-V symmetric vibration bands, respectively. The triply coordinated oxygen atom between three vanadium atoms contributes to the stretching absorption peak at roughly 464 cm^{-1}. The presence of TiO_2 in the V:Ce:Ti composite resulted in a weak band (shoulder) at 520 cm^{-1} due to a Ti-O stretching vibration.

3.2.1.2 Raman spectroscopy results

The distinctive features of CNTs can be identified by Raman spectroscopy (Figure 35. MWCNTs). The radial breathing mode (RBM) corresponds to the in-phase, radial movement of the carbon atoms within the structure of CNTs, which is usually not present in the Raman spectra of MWCNTs due to the weakening effect of their larger diameters [199]-[200]. However, two separate RBM bands were observed at 121 and 143 cm^{-1}. Since the position of an RBM band is influenced by the diameter of the CNTs, it can be utilized to estimate their average diameter [199] [201]. The bands at 121 and 143 cm^{-1} indicate the presence of two small, slightly different diameters with averages of 2.1 and 1.8 nm, respectively. The band at 1284 cm^{-1} can be assigned to the presence of defect sites in the sp2 carbon structure (D band). The position of the D band depends on the diameter and chirality of the carbon structure as well as the laser wavelength applied [214]. The D band can be deconvoluted into two bands centred on the same wavenumber for small crystallites of CNTs [215]. The peak at 1598 cm^{-1} is attributed to the vibrations of the sp2 carbon structure (G band). Splitting of the G band (G^+-G^-) is not observed, as is expected for MWCNTs [212]. The band at 2561 cm^{-1} (G' band) is the overtone of the D band, however, contrary to the D band, it indicates the long-range order of the structure arising from defect-free sp2 carbon atoms [199]-[200].

As a result of being treated with strong acids, structural defect sites are introduced in the form of carboxyl, carbonyl and hydroxyl groups via oxidation of the carbon structure [203]-[204]. After oxidative treatment, the RBM band at 143 cm^{-1} disappeared, moreover, the G and G‘ bands shifted slightly to higher wavenumbers, that is, 1289 and 2566 cm^{-1}, respectively, indicating successful surface modification (Figure35. ox-MWCNTs). The peak area or intensity ratios of the D and G bands $\left(\frac{I_D}{I_G}, \frac{A_D}{A_G}\right)$ can be used to estimate the quality of the CNT structure and the extent of surface modification via the presence of defect sites [201]-[202]. Alternatively, the G' and D band ratios $(\frac{I_{G'}}{I_D}, \frac{A_{G'}}{A_D})$ can be used to

calculate a more accurate estimation [218]. The calculated intensity ratios follow a similar trend with regard to the peak areas (Table 1 in Appendix-A-). After oxidative treatment, the $\frac{I_D}{I_G}, \frac{A_D}{A_G}$ values decreased, while the $\frac{I_{G\prime}}{I_D}, \frac{A_{G\prime}}{A_D}$ values increased (Table 1 in Appendix-A), indicating a slightly more disordered structure as a result of acid treatment [219]. No major spectral changes were observed once the nanocomposites had been prepared (Table 1 in Appendix-A; Figure 35. Ce/, V/ & V:Ce/MWCNTs). Most probably, due to their low surface concentration, no new peaks were identified in accordance with the Raman scattering of V_2O_5 [219] or CeO_2 [220] polymorphs. However, based on their D- and G'-band ratios, the structural order of the V and Ce nanocomposites surprisingly increased slightly compared to that of the MWCNTs (Table 1 in Appendix-A).

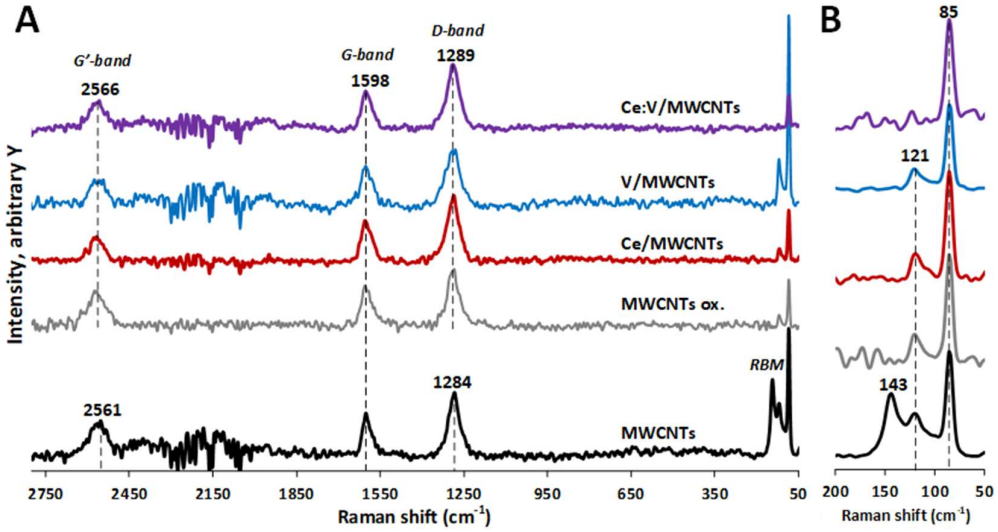

Figure 35. Raman spectra of the MWCNTs samples: (A) normalized to the D-band intensity within the 2750-50 cm^{-1} range and (B) normalized to the RBM bands within the 200-50 cm^{-1} range

3.2.1.3 X-ray diffraction results

In the case of the prepared vanadium pentoxide nanoparticles annealed at 500 °C, the main diffraction peaks of (200), (001), (101), (110), (301), (011), (310), (002), (600) and (020) appear at 2θ = 15.21°, 20.32°, 21.57°, 26.01°, 30.83°, 32.19°, 34.17°, 41.09°, 47.17° and 51.09°, respectively, as is shown in Figure 36. These peaks relate to the orthorhombic Shcherbinaite crystal structure of vanadium pentoxide (JCPDS Card No. 41-1426).

The XRD results of titanium dioxide nanoparticles prepared by the sol-gel hydrothermal method and annealed at 500 °C are shown in Figure 36. The main diffraction peaks of TiO_2 treated at 500 °C are (110), (101), (111), (210), (211), (220) and (002) corresponding to 2θ = 27.41°, 36.03°, 41.25°, 44.01°, 54.11°, 56.07° and 62.81°,

respectively of the rutile form, as indexed in JCPDS Card No. 21-1276 [221]. In addition to the weak diffraction peaks of (101), (112) and (200) corresponding to 2θ = 25.27°, 39.09° and 47.99°, respectively, the anatase form of TiO_2 (JCPDS Card No. 21-1272) is observed.

The XRD results of the cerium dioxide nanoparticles prepared by the hydrothermal method and annealed at 500 °C are shown in Figure 36. The main diffraction peaks of CeO_2 are (111), (200), (220), (311), (222) and (400) which appear at 2θ = 28.60°, 34.03°, 47.43°, 56.35°, 59.10° and 69.42°, respectively of the cerianite form, as indexed in JCPDS Card No. 34-0394 [222].

The X-ray diffraction results for V:Ti, V:Ce and V:Ce:Ti composites annealed at 500 °C for 2h are also presented in Figure 36. In all mixed composites, the constituent orthorhombic crystalline structure of V_2O_5 dominates over the CeO_2 and/or TiO_2 forms of crystals.

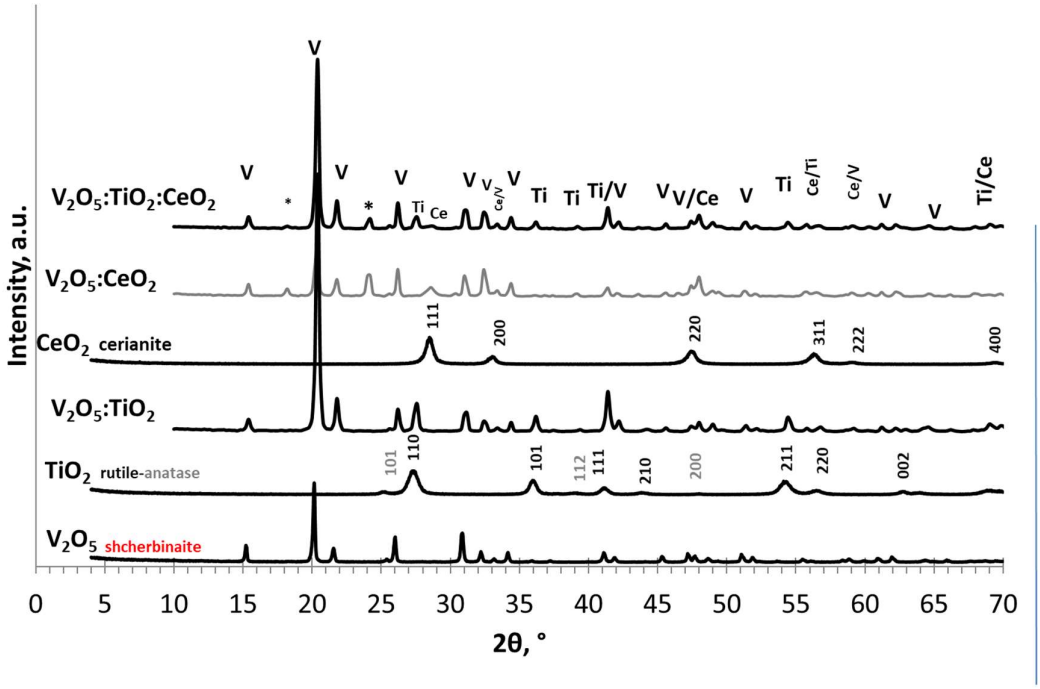

Figure 36. XRD results for V_2O_5, TiO_2 and CeO_2 single metal oxides as well as V_2O_5:CeO_2 and V_2O_5:TiO_2:CeO_2 hybrid nanocomposites annealed at 500 ºC

The XRD results for the samples of fresh V_2O_5:CeO_2 MWCNTs, ox-MWCNTs, V/MWCNTs, Ce/MWCNTs and V:Ce/MWCNTs are presented in Figure 37. V:Ce nanoparticles prepared by the hydrothermal method and annealed at 500 °C showed reflections of both oxides, namely V_2O_5 and CeO_2. In the case of vanadia nanoparticles,

the main diffraction peaks of (200), (010), (110), (101), (310), (011), (301), (020) and (320) appear at 2θ = 15.04°, 20.04°, 21.80°, 26.20°, 31.00°, 32.40°, 34.20°, 41.20° and 48.00°, respectively. These peaks relate to the orthorhombic Shcherbinaite crystalline structure of vanadium pentoxide (JCPDS Card No. 41-1426) [223].

The main diffraction peaks of CeO_2 are (111), (200), (220) and (311) which appear at 2θ = 28.60°, 32.20°, 47.40° and 56.51°, respectively in the form of cerianite, as indexed in JCPDS Card No. 34-0394 [224]. In mixed composites, the constituent V_2O_5 orthorhombic crystalline structure dominates over the CeO_2 equivalent. Furthermore, the presence of some impurities were observed at 2θ = 18.20° and 24.20°, originating from the preparation step.

The XRD results for fresh MWCNTs, ox-MWCNTs, V/MWCNTs, Ce/MWCNTs and V:Ce/MWCNTs samples treated at 200 °C are also shown in Figure 37. On the basis of the XRD results, it can be seen that the graphene layers of MWCNTs are preserved after acid treatment and deposition of metal oxides. The diffraction peaks at 2θ = 25.3° and ~43° of the metal oxide-doped MWCNTs are (002), (100) and (101) reflections of graphite, as indexed in JCPDS Card No. 01-071-4630 [225]. The peaks corresponding to CeO_2 and V_2O_5 in the Ce/MWCNTs and V/MWCNTs could not be detected possibly because of their nominal addition and/or good dispersion of the oxides. The major crystalline phase with regard to the graphene layers of the MWCNTs was recorded for all multi-walled carbon nanotubes. The presence of some crystals of individual oxides was detected for samples of V:Ce/MWCNTs.

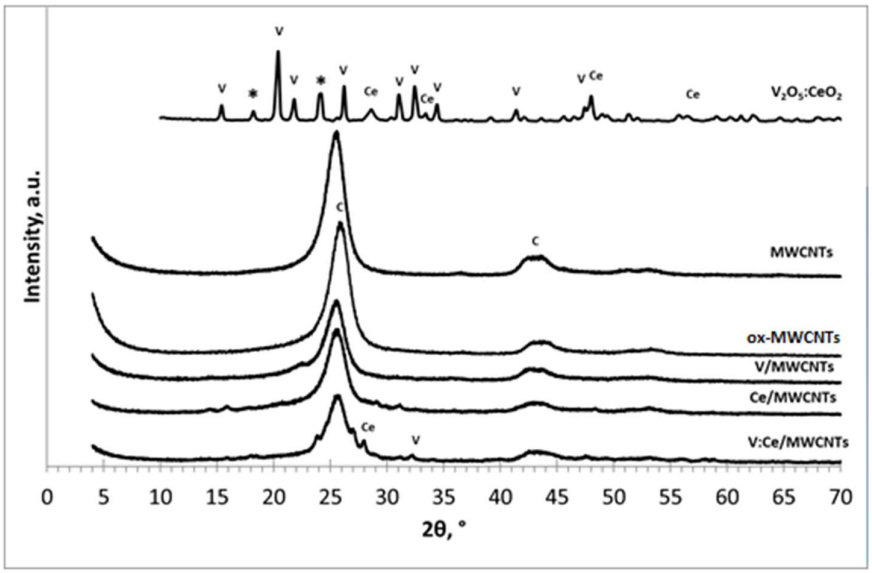

Figure 37. XRD results for fresh and doped MWCNTs, where V, Ce and C denote the V_2O_5, CeO_2 and graphene crystalline phases and * represents impurities

3.2.1.4 Atomic force microscopy results

AFM in three-dimensional images of V_2O_5, CeO_2 and V:Ce nanoparticles after annealing at 500 °C are shown in Figure 38. The morphological images of V_2O_5, CeO_2 and V:Ce nanoparticles clearly depict that the average grain sizes were found to be 70.34, 56.94 and 71.44 nm, respectively (Table 6), as is shown in Figures 38a-c. The addition of cerium dioxide to vanadium pentoxide resulted in a slight increase in the average grain size. The average grain size of TiO_2 was 66.30 nm (Table 6).

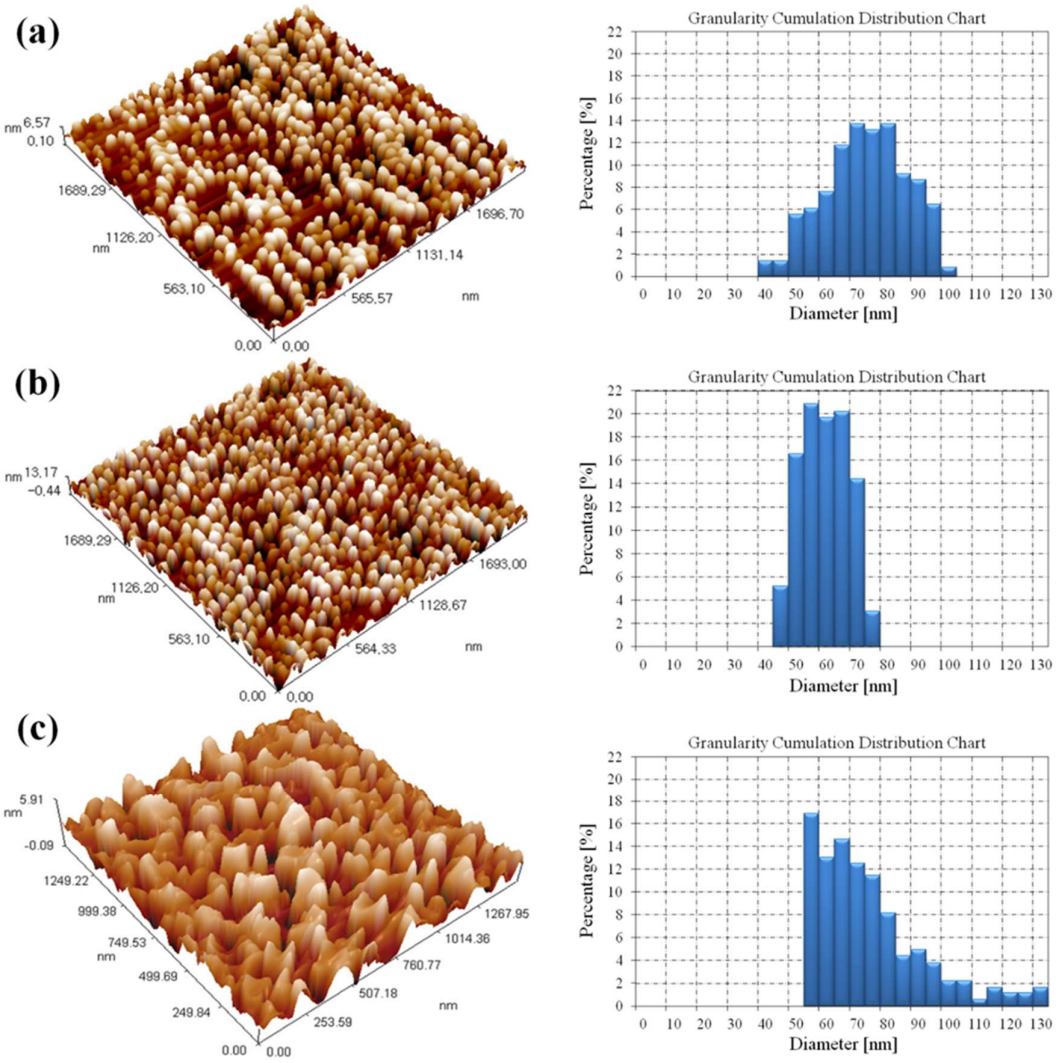

Figure 38. AFM results of (a) V_2O_5, (b) CeO_2 and (c) V:Ce composites at an annealing temperature of 500 °C

Table 6. Average diameter of grains found in nanoparticles sorbents prepared samples

Sample	Average diameter, nm
V_2O_5	70.34
CeO_2	56.94
TiO_2	66.30
V:Ce	71.44

3.2.1.5 Electron and transition spectroscopy results

SEM results for metal oxides are shown in Figures 39a–c. Figure 39a shows the surface morphology of V_2O_5 nanopowder identified in the form of nanoflakes close to 65–80 nm in thickness, which is in agreement with the atomic force microscopy (AFM) results. Figure 39b shows that the surface morphology of the CeO_2 nanopowder adopts a different shape including nanorods, the diameter of which can be seen on the nanoscale (60–70 nm) and is also shown by the AFM analysis. Figure 39c shows the V:Ce nanocomposite in which the vanadium pentoxide is preserved in the form of nanoflakes.

SEM and TEM results for fresh MWCNTs and for metal oxide-doped MWCNTs are shown in Figures 40 and 41. It can be observed that the size of the carbon nanotubes remains within the nanoscale range and their shape was not significantly affected during the thermal modification of MWCNTs in the presence of nanoparticles (Figures 41a–c). MWCNTs under a high magnification were 40 nm in diameter, as is shown in Figure 42a. The shape of the tubes is very clear, as compare with high magnification TEM Figure 42b and 42c, 100nm and 40 nm for V:Ce/MWCNTs, its clear that nanoparticles doped MWCNTs.

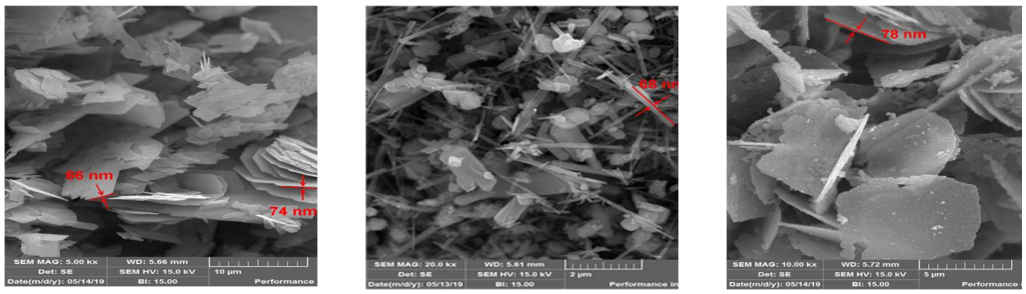

(a) **(b)** **(c)**

Figure 39 SEM images between 2 and 10 µm: (a) V_2O_5, (b) CeO_2, (c) V:Ce

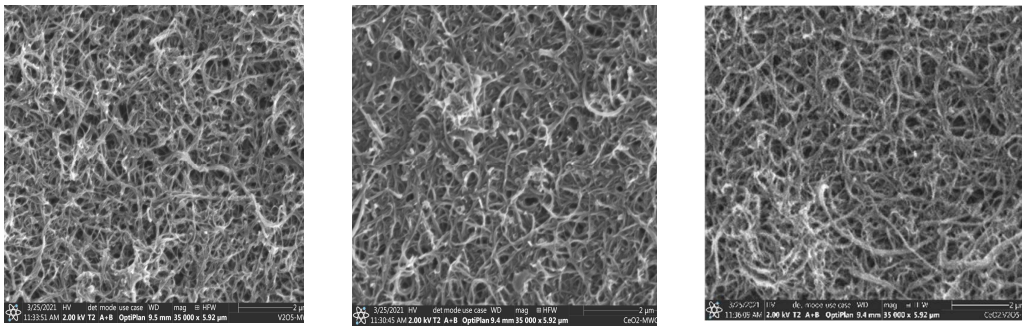

(a) (b) (c)

Figure 40 SEM images on scale of 2 µm: (a) V/MWCNTs, (b) Ce/MWCNTs, (c) V:Ce/MWCNTs

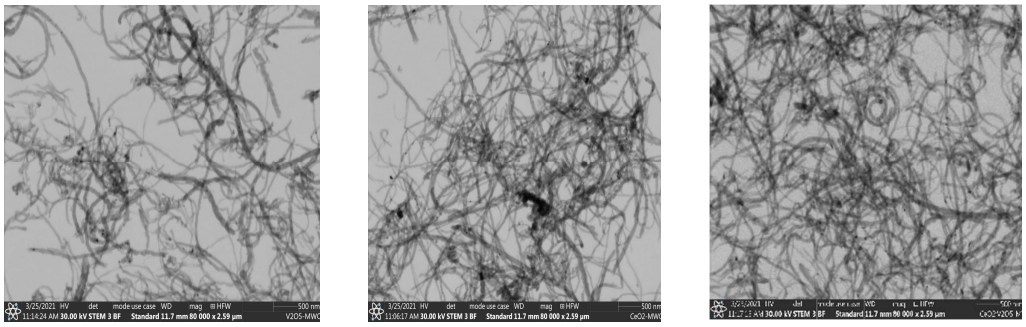

(a) (b) (c)

Figure 41 TEM images on a scale of 500 nm: (a) V/MWCNTs, (b) Ce/MWCNTs, (c) V:Ce/MWCNTs

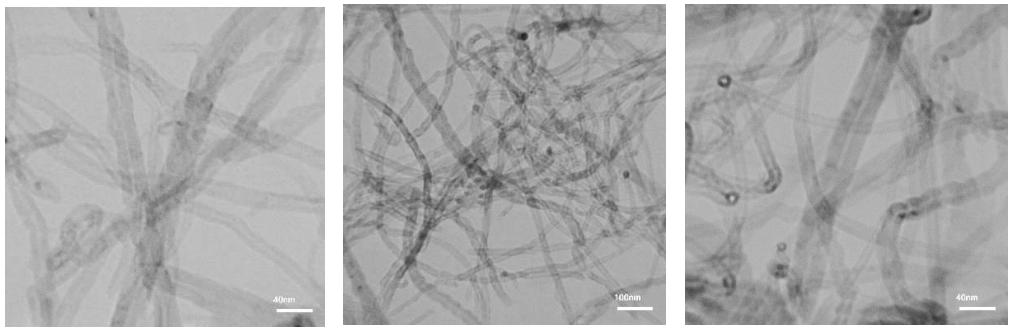

(a) (b) (c)

Figure 42 TEM images on scale 40 nm of MWCNTs, and V:Ce/MWCNTs 100 nm (a), and 40 nm (b) of V:Ce/MWCNTs

3.2.1.6 Energy Dispersive X-ray Spectroscopy (EDX) Results

EDX results were recorded to determine the amount of carbon, vanadium, titanium and/or cerium on the surface of the samples. The analysis was carried out on three areas of the specimens and the average measured compositions of the near-surface layer of the samples are presented in Table 7.

Table 7. Compositions of metal oxide-doped MWCNTs

Samples	Theoretical wt%	wt% measured by EDX
V:Ti	3:1	2.93:1.00
V:Ce	3:1	2.89:1.00
V:Ce:Ti	3:0.5:0.5	1.72:0.62:0.53
V/MWCNTs	2.3/97.7	4.57/95.43
Ce/MWCNTs	7.4/92.6	5.96/94.04
Ti/MWCNTs	2/98	5.18/94.82
V:Ce/MWCNTs	6.0:2.1/91.9	4.16:6.18/89.66
V:Ti/MWCNTs	4.0:1.2/93.7	1.16:0.38/98.47
V:Ce:Ti/MWCNTs	3:0.5:0.5/96	3.31:1.95:1.64/93.20

The compositions of V:Ti and V:Ce mixed samples estimated by EDX analysis were in good agreement with the theoretical values used in their preparation. Higher or lower amounts of metal oxide/s than expected were detected in other samples. The EDX results support the notion that metal oxides were deposited on the surface of the carbon nanotubes.

3.2.1.7 Thermogravimetric analysis results

The untreated MWCNTs sample used for surface modification shows two notable regions (Figure 43. MWCNTs). A minor reduction in mass is observed up to 190 °C as the water adsorbed on the surface is removed, while a major reduction in mass is noted between 440 and 750 °C, indicating the thermal decomposition of the carbon structure (Table 2 in Appendix-A. MWCNTs). After annealing at 1,000 °C, the residual mass indicates the impure nature of the MWCNTs samples (m = 10.4%) due to the presence of catalytic residues from the production of CNTs. The observed amount of catalytic impurities is well within the acceptable range reported in the literature (cc. 6-43%) [205] [213].

As a result of surface treatment using strong acids, the MWCNTs structure is oxidized via the introduction of oxygenated surface functional groups, namely carboxyl, carbonyl and hydroxyl [227]. The improved hydrophilic nature due to the modified surface properties of the acid-treated MWCNTs samples is indicated by the increased amount of adsorbed water (Figure 43. ox-MWCNTs; Table 2 in Appendix-A. ox-MWCNTs between 21 and 155 °C). Oxidation of the carbon backbone results in the presence of defect sites that eventuate in the lower thermal stability of the functionalized CNTs [228].

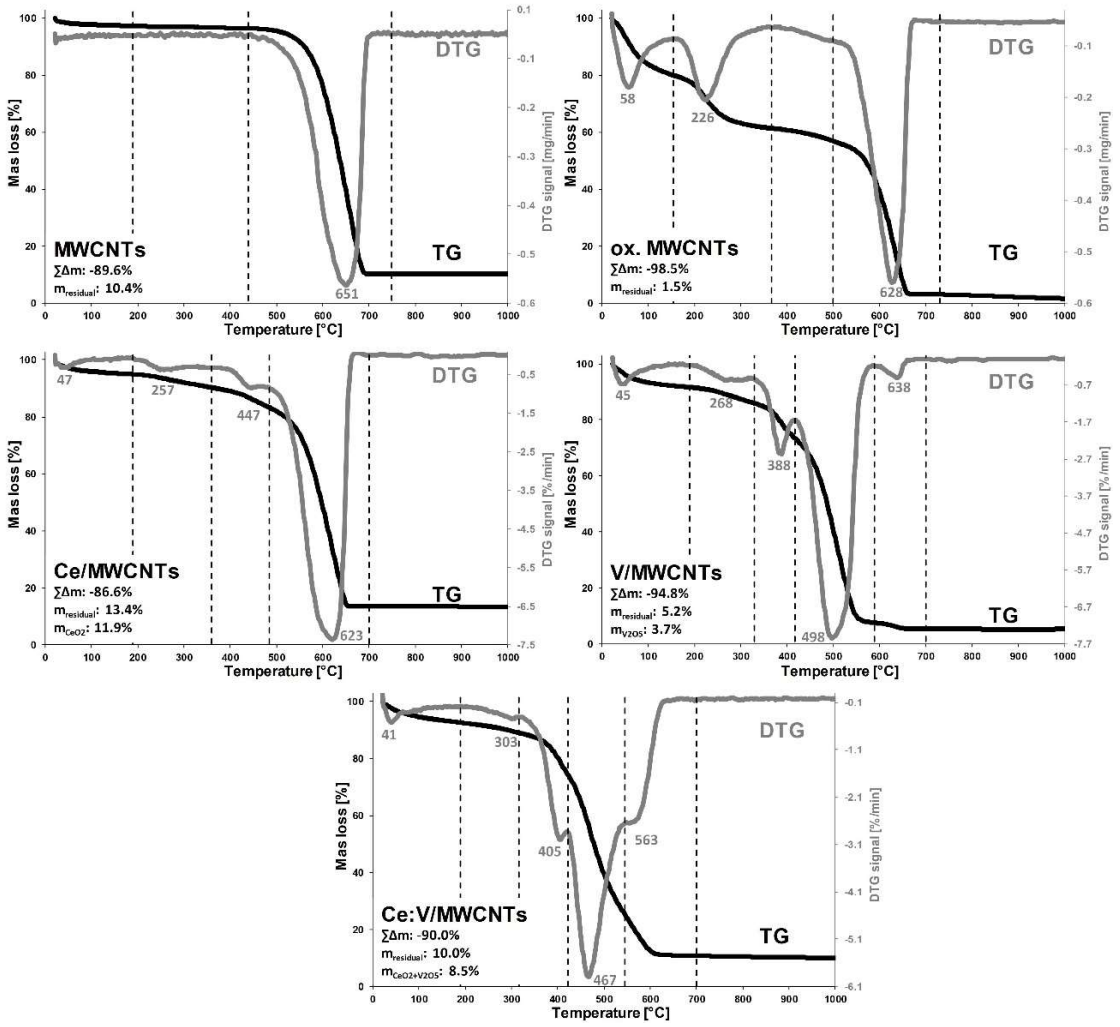

Figure 43. Thermogravimetric curves (TG/DTG) of the MWCNTs samples

The elimination of the introduced surface carboxyl groups is observed in the second step between 155 and 366 °C, while a small reduction in mass between 366 and 500 °C could be attributed to the decomposition of other thermally more stable surface functional groups [227]. Significant decomposition was observed between 500 and 730 °C. Compared to the pristine MWCNTs, the shift towards a higher starting temperature and the narrower decomposition curve indicate the purifying effect of acid treatment, mostly via the removal of carbon impurities. The significantly smaller residual mass (m=1.5%) is due to the removal of catalytic residuals during acid treatment [227]. Consequently, the acid treatment resulted in a purified MWCNTs sample.

Small changes are observed following the addition of CeO_2 to the oxidized MWCNTs (Figure 43. Ce/MWCNTs; Table 2 in Appendix-A. Ce/MWCNTs). Since no thermal decomposition is expected due to the presence of pre-annealed CeO_2 particles [216], the

differences could be related to the interactions between the lanthanide oxide nanoparticles and the carbon nanostructure. The slightly higher maximum temperature (257 °C vs. 226 °C) of the second stage could indicate a possible interaction between the surface carboxyl groups of the CNTs and the introduced CeO_2 resulting in the increased thermal stability of the surface moieties. Although the thermal stability of the MWCNTs backbones did not change considerably (628 °C vs. 623 °C), the increased reduction in mass as a result of the third stage (360-485 °C) could be indicative of the increased ratio of MWCNTs particles having a slightly lower thermal stability. This effect could be related to the thermal activation of the CeO_2 catalyst at elevated temperatures, resulting in the slight enhancement of the pyrolysis of CNTs [229].

Similar changes can be observed following the addition of V_2O_5 nanoparticles (Figure 43. V/MWCNTs; Table 2 in Appendix-A. V/MWCNTs). No additional reduction in mass is expected due to the addition of previously heat treated V_2O_5 particles [228]. The thermal stability of the second stage increased further (Tmax = 268 °C), indicating the slightly stronger interaction of vanadium pentoxide particles with the functionalized surface of the CNTs. Compared to the ox-MWCNTs sample, major changes can be observed in the thermal stability of the CNTs backbone: the reduction in mass ratio of the third stage increased and the maximum shifted to 388 °C, while the prominent decomposition stage also shifted to 498 °C from 628 °C. Only a small reduction in mass at a maximum of 638 °C indicates the presence of MWCNTs particles with their original thermal stability. These changes can be indicative of the thermally activated catalytic properties of V_2O_5 nanoparticles [230], resulting in enhanced pyrolysis and the lower thermal stability of MWCNTs.

The joint presence of CeO_2 and V_2O_5 particles resulted in the further reduction in the thermal stability of MWCNTs (Figure 43. V:Ce/MWCNTs; Table 2 in Appendix-A. V:Ce/MWCNTs). The temperature range resulting in the thermal decomposition of the MWCNTs backbones decreased slightly, where 3 overlapping stages can be identified (316-422 °C, 422-545 °C, 545-700 °C). The observed decrease in thermal stability can be explained by the increased catalytic activity due to the simultaneous presence of CeO_2 and V_2O_5 catalysts [231]. Overall, the addition of V_2O_5 particles significantly decreased the thermal stability of MWCNTs. The residual masses after annealing at 1,000 °C can be utilized to estimate the metal-oxide content of the samples (Table 2 in Appendix-A). Considering the residual mass of the ox-MWCNTs samples (m = 1.5%), the estimated

oxide contents of the Ce/, V/ and V:Ce/MWCNTs samples are 11.9%, 3.7% and 8.5%, respectively, which are slightly greater than the values obtained by EDX (Table 6). These differences can be explained by the higher degree of uncertainty of EDX, since the analytical signal originates from a smaller volume (on the scale of μm^3) so the overall composition is subjected to greater errors due to the possible inhomogeneity of the sample [232]. Overall, the metal-oxide content of the MWCNTs composites were found to be greater than their theoretical values.

3.2.1.8 Low temperature nitrogen adsorption results

Metal-oxide samples calcined at 500 °C with masses of 0.5-1.0 g that had previously been outgassed in a vacuum at 160 °C were used for the low temperature nitrogen adsorption experiments. The total surface area of CeO_2 is relatively high (69 m^2/g). The pore volume and surface area of the micropores of CeO_2 nanoparticles also exhibit the highest values among the pure metal oxides prepared (Table 8). V_2O_5 has the lowest surface area (3 m^2/g) and is the main component of the mixed metal oxide nanocomposites (V:Ce:Ti ratio of 1.72:0.62:0.53).The surface area of mixed metal oxides depends on the amount of individual oxides and interactions between constituent oxides. The surface area is an important factor in the adsorption steps.

Table 8. Surface morphology of metal oxide nanocomposites

Samples	S_{BET} (m^2/g)	S_{micro} (m^2/g)	$V_{1.7\text{-}300\ nm}$ (cm^3/g)	V_{micro} (cm^3/g)	D_{av} (nm)
V_2O_5	3.0	0.0	0.0073	0.0000	13.4
CeO_2	69.4	15.5	0.1676	0.0069	13.4
TiO_2	43.3	0.5	0.0457	0.0001	13.6
V:Ti	7.3	0.3	0.0232	0.0001	12.1
V:Ce	8.8	0.5	0.0368	0.0001	15.0
V:Ce:Ti	6.4	0.2	0.0321	0.0001	18.2

Additional increases in surface area were observed following the deposition of metal oxides onto MWCNTs (Table 9). The reduction in the mass of a sample occurred during outgassing before the BET analysis. The highest reduction in mass was observed in the case of ox-MWCNTs and V:Ti/MWCNTs, 7.9 wt% (Table 9). It is assumed that the presence of some moisture resulted in an acid condensate remaining in the bulk of the sample after acid treatment and deposition of metal oxides which were subsequently dried

at 100 °C. The result of treating MWCNTs with $3H_2SO_4$:$1HNO_3$ could be due to defect sites formed on its surface resulting in the splitting of CNTs [221] leading to the creation of new openings in the channels of tubes and an increase in the total volume (Table 9).

Table 9. Reduction in mass during outgassing; total and micropore surface areas, S_{BET} and S_{micro}; volume of pores between 1.7 and 300 nm in diameter and that of micropores, $V_{1.7–300\ nm}$ and V_{micro}; average pore size of fresh and acid-treated MWCNTs as well as metal oxide-doped MWCNTs, D_{av} values.

Samples	Reduction in mass (wt%)	S_{BET} (m^2/g)	S_{micro} (m^2/g)	$V_{1.7-300}$ (cm^3/g)	V_{micro} (cm^3/g)	D_{av} (nm)
MWCNTs	0.1	156	25.4	0.6577	0.0109	16.1
ox-MWCNTs	7.9	140	13.6	1.0384	0.0052	28.2
Ti/MWCNTs	2.9	156	0.0	1.0015	0.0000	24.5
V/MWCNTs	1.3	135	6.9	0.8439	0.0018	24.5
Ce/MWCNTs	4.5	115	0.0	0.7002	0.0000	24.1
V:Ce/MWCNTs	6.9	129	0.0	0.8545	0.0000	25.8
V:Ti/MWCNTs	7.9	125	8.4	0.7004	0.0027	23.7
V:Ce:Ti/MWCNTs	7.6	126	3.3	0.8108	0.0001	26.0

As can be seen in Table 9, the acidic treatment applied resulted in a significant decrease in the volume of the micropores. The acid treatment of MWCNTs could lead to the formation of carboxyl and hydroxyl functional groups which might block the small pores [222], possibly resulting in a slight decrease in S_{BET} from 156 to 140 m^2/g. This also has an impact on the total pore-size distribution (Figure 44).

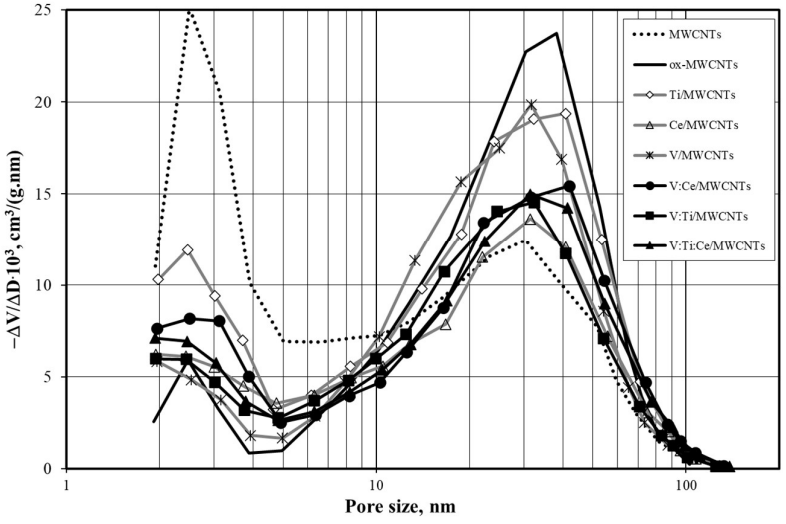

Figure 44. Pore volume distribution of samples of fresh and oxidized MWCNTs as well as metal oxide-doped MWCNTs

The MWCNTs doped with newly prepared TiO_2 have a greater surface area. S_{BET} was calculated to be 43 m^2/g which is similar than that of the commercial Degussa P25 titania calcined at 500 °C (S_{BET} = 52 m^2/g) [233]. At 500 °C, the calcination temperature can result in both the formation of rutile (18 wt%) and anatase (82 wt%) crystalline phases [234]. In our TiO_2 sample, the major crystalline phase was composed of rutile as confirmed by XRD results.

The V_2O_5 sample calcined at 500 °C has an orthorhombic crystal structure with a small surface area of 3 m^2/g. As a result of the deposition of metal oxides over the ox-MWCNTs, the pore volumes and pore diameters of the metal oxide-modified samples decreased (Table 9) in comparison with acid-treated MWCNTs. In addition to this, it was also observed that the micropores were totally blocked and disappeared after the deposition of TiO_2 and CeO_2, as is shown in Table 9. When V_2O_5 was added to the MWCNTs, the surface area of the micropores decreased by 50%. The total surface area of Ti/MWCNTs is similar to that of raw MWCNTs, meanwhile, is higher than for ox-MWCNTs indicating that the titanium dioxide is dispersed and incorporated onto the surface of MWCNTs. Therefore, it contributes to the morphological properties of the samples. The specific surface areas of V/MWCNTs, Ce/MWCNTs and mixed metal-doped MWCNTs were lower than in the case of ox-MWCNTs (140 m^2/g).

The pore size distributions of these preparations are shown in Figure 44. Pores of 2-3 nm and 20-40 nm in diameter are present in higher amounts in the case of fresh MWCNTs. The number of smaller pores (2-3 nm) decreases and that of 20-40 nm in diameter slightly increases during the acid treatment of MWCNTs and in the case of metal oxide-doped MWCNTs samples.

3.2.2 Adsorption test results

3.2.2.1 Methylene blue adsorption over metal oxide-doped MWCNTs

A comparative study was carried out on the five adsorbents, namely fresh MWCNTs, ox-MWCNTs, titanium dioxide-doped MWCNTs (Ti/MWCNTs), vanadium pentoxide-doped MWCNTs (V/MWCNTs) and cerium dioxide-doped MWCNTs (Ce/MWCNTs), in order to study the efficiency of MB removal from aqueous solutions over metal oxide-doped preparations. The removal efficiency of different nanoparticle preparations was studied as a function of time.

V/MWCNTs resulted in the highest degree of MB removal from water. Following this, the vanadium pentoxide nanoparticles were used to prepare different nanoparticle

composites (V:Ti, V:Ce and V:Ce:Ti) and modify the MWCNTs. The removal efficiencies of V/MWCNTs and their nanoparticle composite-doped MWCNTs were studied as a function of various experimental parameters, including contact time, amount of adsorbent and contact temperature, to determine the optimum conditions of MB removal from water.

A study was carried out on single metal oxides, mixed metal oxides as well as raw and metal oxide-doped MWCNTs as a function of time over 35 min. Measurements were taken every 5 min. The initial MB concentration, volume of the MB solution and mass of the samples were 20 mg/L, 20 mL and 4.5 mg, respectively. The MB concentration reached its minimum after being pretreated with V:Ce/MWCNTs in comparison with other nanocomposite samples (Figure 45). As can be seen in Figure 46, the V:Ce/MWCNTs exhibit the highest MB removal efficiency from water in comparison with raw, ox-MWCNTs and single metal oxide-doped MWCNTs.

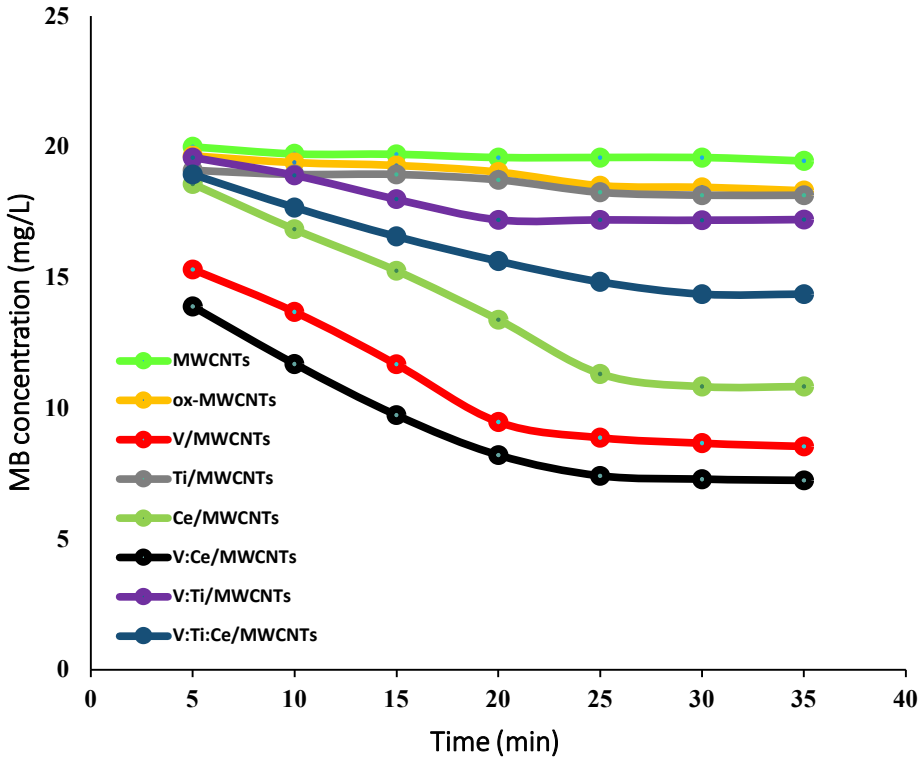

Figure 45. MB concentration against contact time of the studied samples

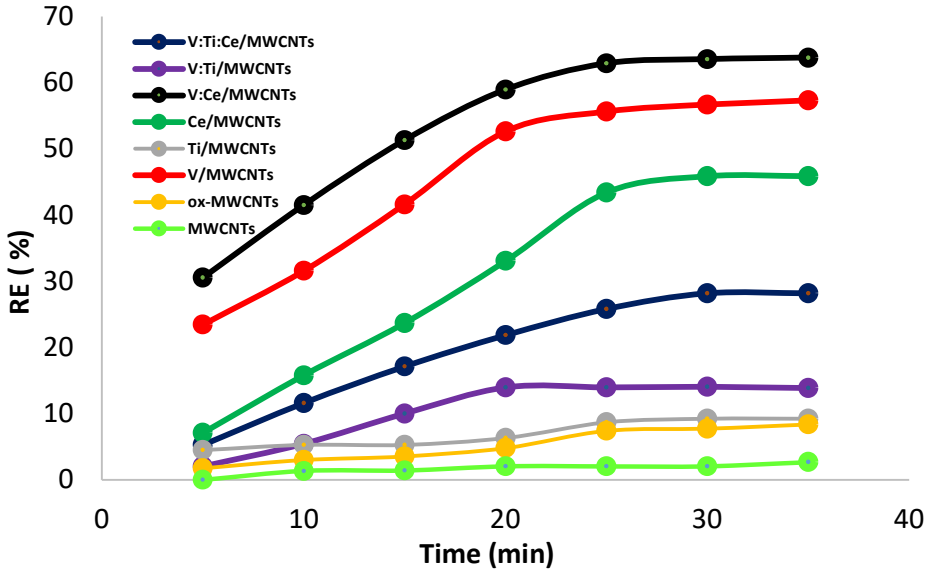

Figure 46. MB adsorption efficiency against contact time using raw, oxidized and metal oxide nanocomposite-doped MWCNTs

As can be seen in Figures 45 and 46, the decrease in MB concentration and increase in the removal efficiency over time with regard to the studied samples were noticeable in the case of V:Ce/MWCNTs and V/MWCNTs for the first 25 min and once an equilibrium had been reached. After 25 min, the adsorption capacity of the samples increased slowly and did not change significantly. The removal efficiency and MB adsorption capacity over metal-oxide and composite nanoparticle-doped MWCNTs are presented in Table 10. The highest removal efficiencies of 57% and 64% were reached over V/MWCNTs and V:Ce/MWCNTs, respectively. These samples also exhibited the highest adsorption capacities of 50.9 and 56.7 mg/g, respectively (Table 10).

Table 10. Removal efficiency (RE) and adsorption capacity (q_t) during MB removal from water over different preparations after 35 min

Adsorbents	RE (%)	q_t (mg/g)
MWCNTs	2.68	2.39
ox-MWCNTs	8.37	7.44
V/MWCNTs	**57.30**	**50.93**
Ti/MWCNTs	9.23	8.21
Ce/MWCNTs	45.85	40.76
V:Ce/MWCNTs	**63.77**	**56.69**
V:Ti/MWCNTs	14.05	12.49
V:Ce:Ti/MWCNTs	28.17	25.05

A similar adsorption capacity (62 mg/g) was obtained over a prepared magnetic nanoadsorbent for the removal of methylene blue [235].

The effect of the amount of adsorbent was studied over the two best-performing composite samples, namely V/MWCNTs and V:Ce/MWCNTs, which exhibited the highest MB removal efficiencies. Different amounts of adsorbents from 1.5 to 10.0 mg were added to the MB solution and the removal of MB was followed for 25 min at room temperature. The results showed that the optimum adsorbent masses were 6.0 and 9.0 mg in the cases of V/MWCNTs and V:Ce/MWCNTs, respectively in 20 mL of solution with an MB concentration of 20 mg/L, as is shown in Figure 47.

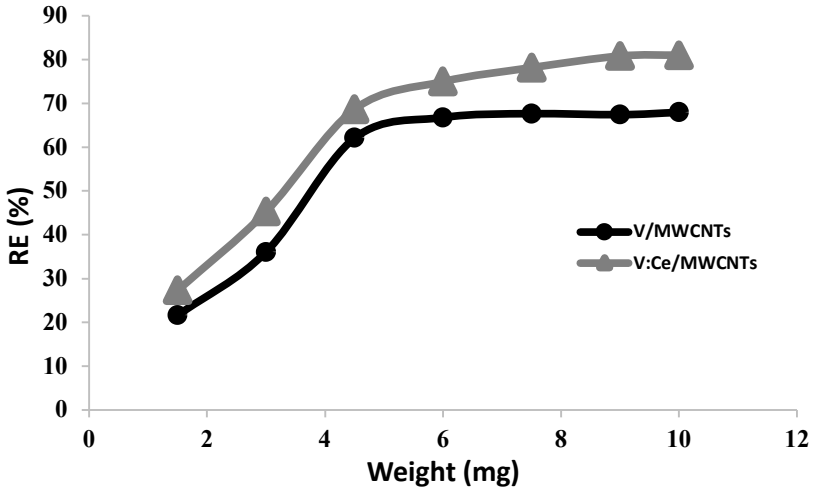

Figure 47. Effect of adsorbent dosage on MB removal over V/MWCNTs and V:Ce/MWCNTs

The effect of temperature on the MB removal efficiency was studied within the temperature range of 15 to 65 °C over V:Ce/MWCNTs samples. The reaction time was 25 min, the mass of the adsorbent was 9 mg, the shaking speed was 240 rpm, the MB concentration was 20 mg/L and the volume of the solution was 20 mL. The results showed that the optimum temperature for MB adsorption over V:Ce/MWCNTs was 45 °C, as is shown in Figure 48.

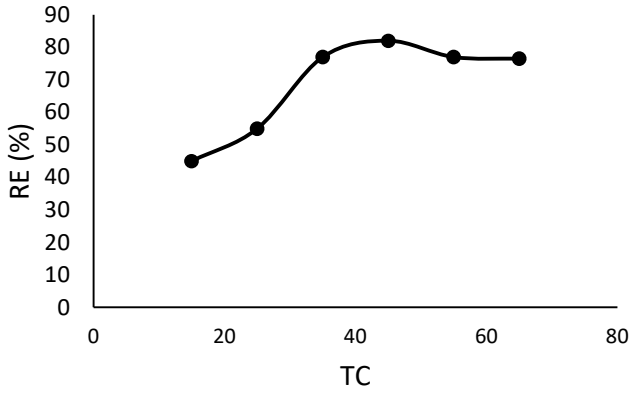

Figure 48. Effect of MB adsorption over V:Ce/MWCNTs against temperature

3.2.2.2 The results of kerosene adsorption over metal oxide-doped MWCNTs

The adsorption of kerosene from an aqueous solution by fresh MWCNTs as well as metal oxide-doped MWCNTs was studied using the GC method and the results are summarized in Figures 49 and 50 as well as Table 11. The initial aqueous kerosene concentration was 500 mg/L and the mass of each sample was 5 mg. The effect of the adsorption time on the kerosene concentration and removal efficiency was studied at different times between 15 and 60 min over the metal oxide-doped MWCNTs samples. The kerosene concentration reached its lowest value 60 min after being pretreated with all the prepared adsorbents (Figure 49). Therefore, the removal efficiency of kerosene was higher after 60 min for all samples, as is shown in Figure 50.

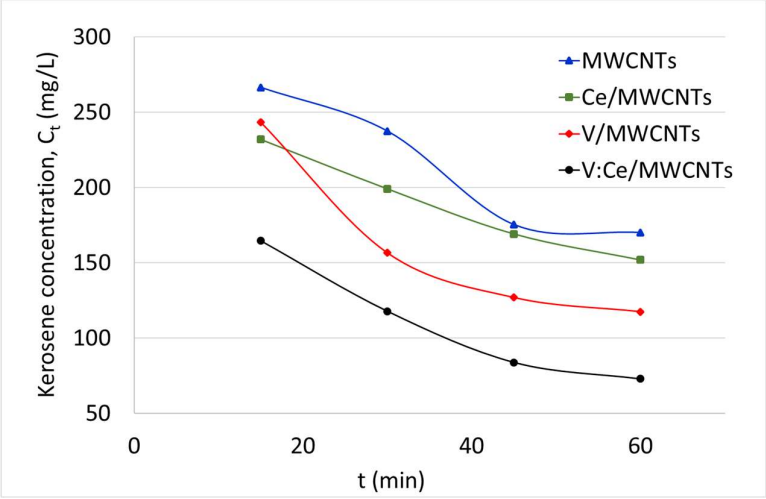

Figure 49. Reduction in kerosene concentration in an aqueous solution against time over MWCNTs, Ce/MWCNTs, V/MWCNTs and V:Ce/MWCNTs (C_0 = 500 mg, V_{sample} = 0.05 L, m_{ads} = 0.005 g)

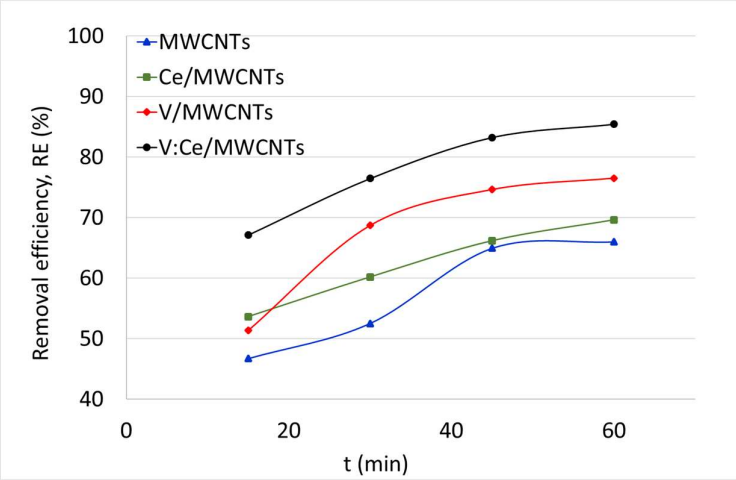

Figure 50. Removal efficiency of kerosene from an aqueous solution against time over MWCNTs, Ce/MWCNTs, V/MWCNTs and V:Ce/MWCNTs (C_0 = 500 mg, V_{sample} = 0.05 L, m_{ads} = 0.005 g)

The removal efficiency of samples increased rapidly during the first 45 mins, after which it slowly decreased for the following 15 min. The GC results presented in Table11 show that the preparation of V:Ce/MWCNTs exhibited the highest adsorption capacity and removal efficiency of kerosene from an aqueous solution (q_t = 4271 mg/g, RE = 85%) after an adsorption time of 60 min regarding the V/MWCNTs (q_t = 3825 mg/g, RE = 77%), Ce/MWCNTs (q_t = 3481 mg/g, RE = 70%) and fresh MWCNTs (q_t = 3300 mg/g, RE = 66%).

Table 11. GC results of the adsorption capacity and removal efficiency of kerosene from an aqueous solution using fresh MWCNTs, Ce/MWCNTs, V/MWCNTs and V:Ce/MWCNTs over different adsorption times

MWCNTs			Ce/MWCNTs		V/MWCNTs		V:Ce/MWCNTs	
Time (min)	RE (%)	q_t (mg/g)	RE (%)	q_t (mg/g)	RE (%)	q_t (mg/g)	RE (%)	q_t (mg/g)
15	47	2335	54	2681	51	2567	67	3355
30	53	2626	60	3009	69	3435	76	3822
45	65	3247	66	3308	75	3731	83	4161
60	66	3300	70	3481	77	3825	85	4271

3.2.3 Kinetic studies of kerosene removal from an aqueous solution over metal oxide-doped MWCNTs

The interactions between the sorbents and adsorbents are explained by a few theoretical approaches such as equilibrium isotherms and adsorption kinetics. Adsorption equilibria explain the physicochemical processes involved in sorption and kinetic measures. They also explain the degree of the transport mechanism of wastewater pollutants onto the adsorbent which is comprised of the external mass transfer of the

sorbate from the bulk solution to the surface of the sorbent, the internal diffusion of the sorbate to the adsorption site, and the overall adsorption process. The kinetic models are relatively efficient when determining the rate at which the adsorbent efficiently removes the adsorbate such as kerosene.

The change in the amount of kerosene adsorbed (q_t) by samples as a function of time is shown in Figure 51. Approximately half of the hydrocarbon concentration (250 mg/L) is removed from water by all samples within the first 15 min of treatment (Figure 49), after which the amount adsorbed rises more slowly as the surface becomes satured with adsorbate. Similar adsorption behaviour was reported with regard to the removal of nitrate [236] and dye molecules [237]. The adsorption capacity study shows that the q_t of fresh MWCNTs is lower than that of metal oxide-doped MWCNTs samples due to the avalibility of more active sorption sites.

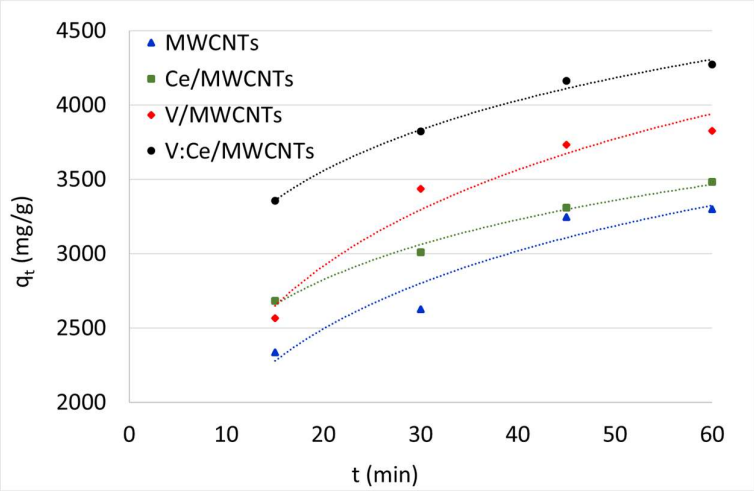

Figure 51. Adsorption capacity of kerosene against the contact time over fresh and doped MWCNTs

In order to ascertain reproducible results, three different kinetic models (pseudo first-order, pseudo second-order and intraparticle diffusion) were applied to study the adsorption kinetics of kerosene over fresh MWCNTs, Ce/MWCNTs, V/MWCNTs and V:Ce/MWCNTs nanocomposites. From (Figure 1 in Appendix-A), it can be seen that the pseudo first-order reaction appropriately fitted to the experimental data for metal oxide-doped MWCNTs (R^2 ~ 0.90-0.97). The value of $q_{e\ cal}$ for V:Ce/MWCNTs was closer to the experimental values obtained (Table 12).

Table 12. Parameters of the applied kinetic model equations with regard to kerosene adsorption from the aqueous solution onto the samples studied

Kinetic Models	Parameters	MWCNTs	Ce/MWCNTs	V/MWCNTs	V:Ce/MWCNTs
	$q_{t\ exp}$ (mg/g)	3300	3481	3825	4271
pseudo first-order	k_1 (min^{-1})	0.089	0.061	0.090	0.090
	$q_{e\ cal}$ (mg/g)	4946	2394	5164	4674
	R^2	0.8969	0.9631	0.9962	0.9494
pseudo second-order	k_2 (mg/g min)	0.30×10^{-4}	0.45×10^{-4}	0.16×10^{-4}	0.28×10^{-4}
	$q_{e\ cal}$ (mg/g)	3333	3333	5000	5000
	R^2	0.9847	0.9978	0.9975	0.9994
intraparticle diffusion	K_d (mg/g $min^{1/2}$)	274	2104	3274	244
	I	1247	1866	1441	2450
	R^2	0.9308	0.9966	0.9064	0.9740

The best-fit kinetic model with regard to the experimental results of kerosene adsorption was the pseudo second-order one (Figure 52). This is indicated by the high values of their linear regressions, namely $R^2 > 0.98$, for all samples as given in Table 12. However, the values of $q_{e\ cal}$ for the V/MWCNTs and V:Ce/MWCNTs were higher than the experimental values obtained, $q_{t\ exp}$. The pseudo second-order model has been applied with regard to the sorption of oil and metal ions over MWCNTs [135].

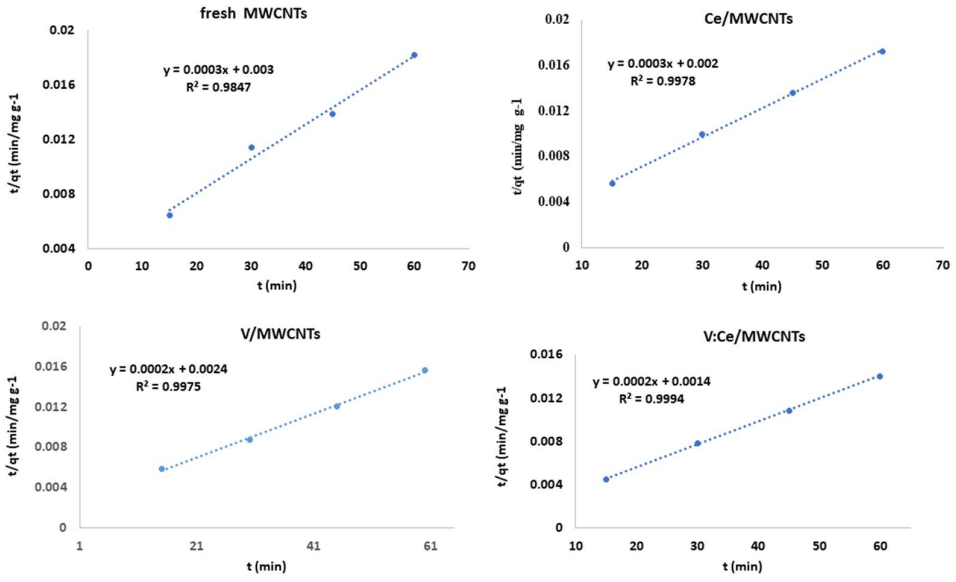

Figure 52 Pseudo-second order plot for kerosene adsorption onto metal oxide-doped MWCNTs

The third kinetic model, that is, intraparticle diffusion, based on the theory proposed by Weber and Morris, was used to identify the diffusion mechanism [238]. According to this theory, the adsorbate uptake, q_t, varies almost proportionally to the square root of the contact time, t½, rather than t [239]. The outcome of this third kinetic model is presented in Figure 53. The constant K_d was obtained from the gradient of the plot of qt against $t^{1/2}$ (Table 12). The resultant plot does not intercept the origin with linear response values and R^2 varies between 0.90 and 0.99 for all samples.

The intercept of the plot is indicative of the boundary layer effect during sorption [240]. Intraparticle diffusion would be considered the rate-limiting step if the plotted curve intercepted the origin. Since the intercept (I) and intraparticle diffusion rate constant (K_d) for all metal oxide-doped MWCNTs samples were large (Table 12), the surface adsorption of kerosene is the rate-limiting step rather than intraparticle diffusion in the reported study.

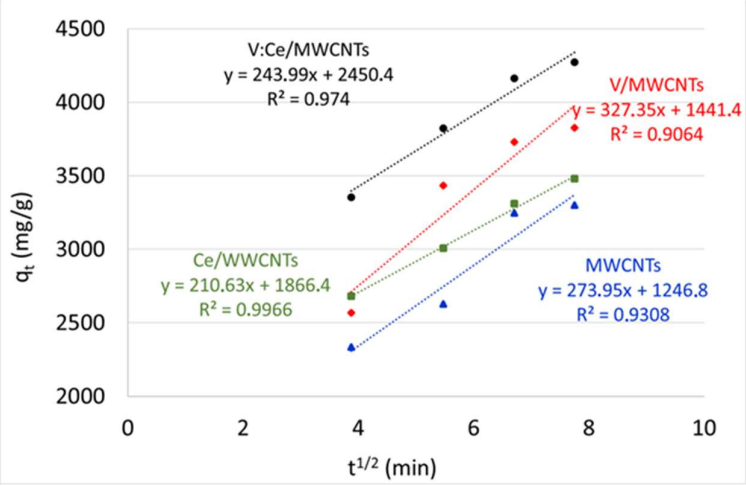

Figure 53. Intraparticle diffusion plot with regard to kerosene adsorption for metal oxide-doped MWCNTs

3.2.4 Adsorption mechanism

3.2.4.1. Mechanism of MB adsorption over metal oxide-doped MWCNTs

For fresh MWCNTs, a π-π interaction can form between π bond in methylene blue and π bond in the carbon nanotubes. The bond could also be a hydrogen bond between the lone pair of electrons on the nitrogen atom and the hydrogen atom at the end of the tubes or at defect sites. When the MWCNTs are oxidized by acids, covalent sidewall functionalization of the nanotubes with -OH, -COOH and -C=O groups occurs, n- π interaction takes place between electron pair of oxygen and π in MB. A stronger

electrostatic interaction can form between carboxyl groups and cationic methylene blue. After modification of the MWCNTs with metal oxide nanoparticles, ionic bonds could be formed between the negatively charged oxygen atom in the metal oxide and the positively charged sulfur in MB (Figure 54).

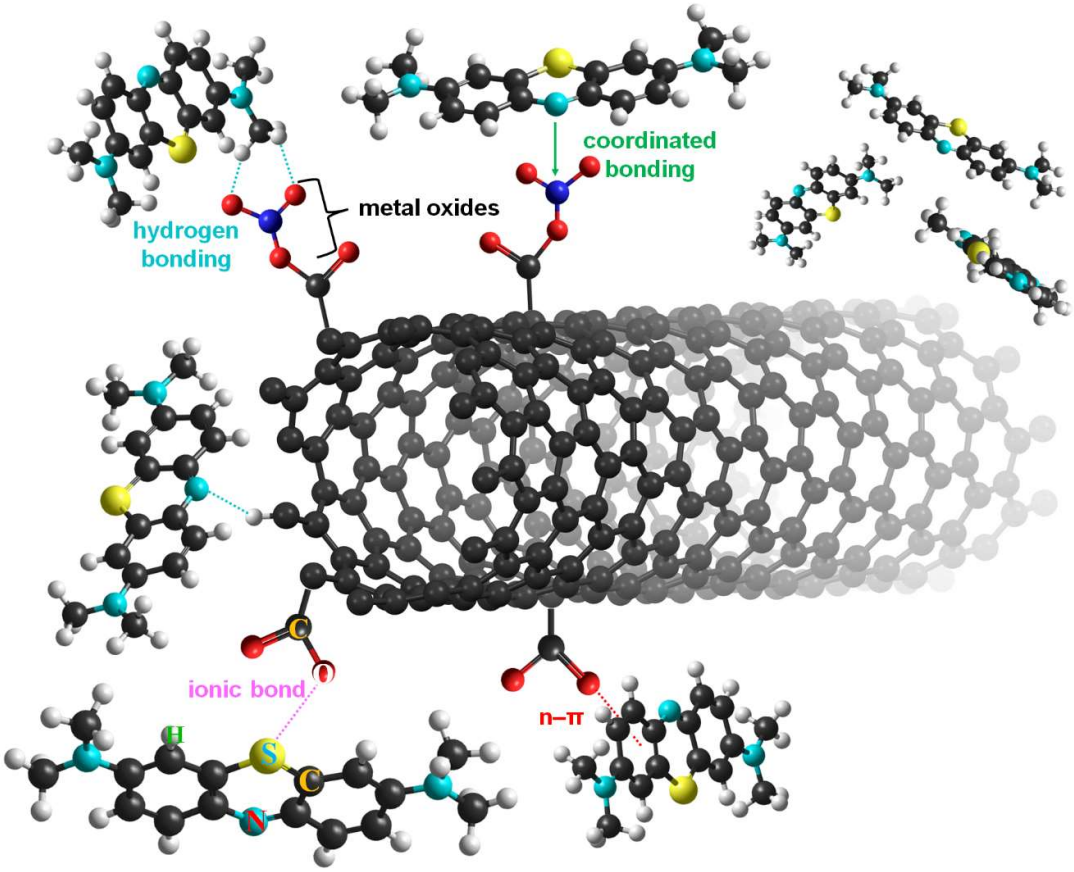

Figure 54. Proposed adsorption mechanism of MB removal using metal oxide-doped MWCNTs

3.2.4.2. Mechanism of kerosene adsorption over metal oxide-doped MWCNTs

A schematic diagram of the sorption of alkane molecules on the surface of MWCNTs samples is presented in Figure 55. One of the most probable ways of bringing about the sorption of nonpolar, alkane molecules on MWCNTs is via CH···π interactions. The CH···π interaction is a weak noncovalent hydrogen bond. In the case of fresh MWCNTs, an interaction occurs between the hydrogen atoms of the saturated hydrocarbons (kerosene) and the carbon atoms of the MWCNTs. Furthermore, a van der Waals interaction could occur. In the case of metal oxide-doped nanoparticles over MWCNTs, hydrogen bonding forms between the oxygen atoms in the metal oxide-doped MWCNTs and the hydrogen atoms in kerosene.

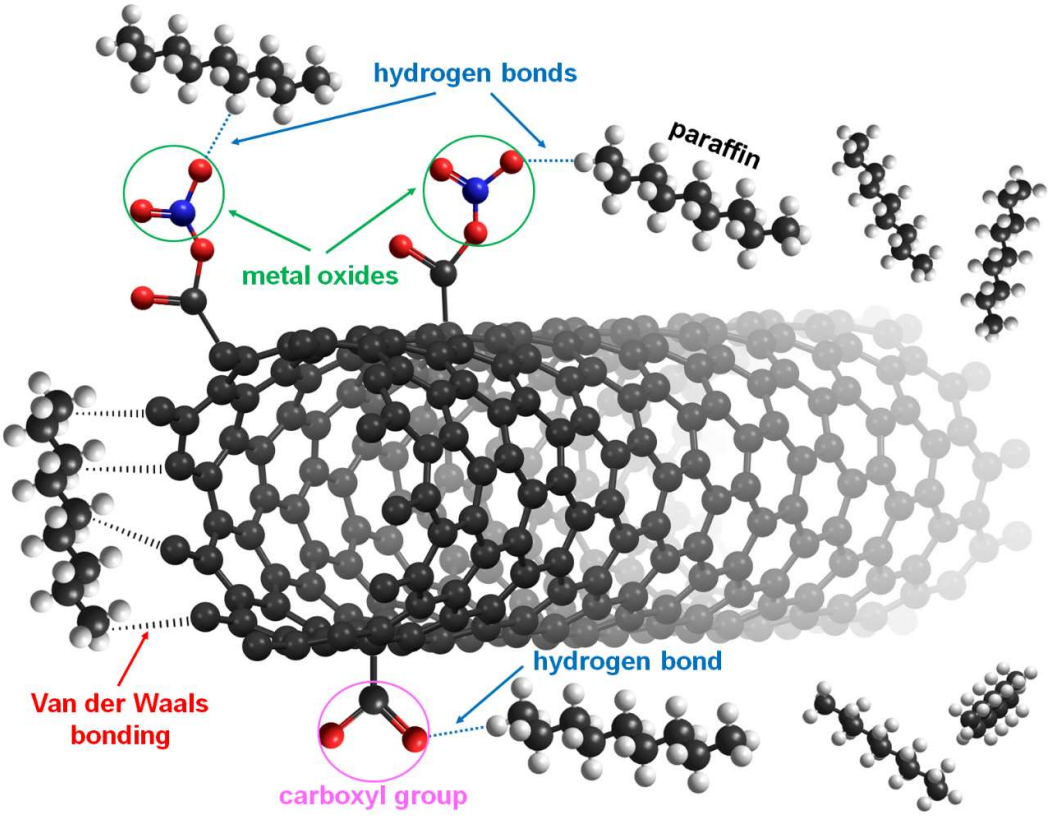

Figure 55. Proposed mechanism for kerosene removal over metal oxide-doped MWCNTs nanocomposites

3.3 Results of Polymer-modified Fe/MWCNTs

3.3.1 Characterization Results of Polymer-modified Fe/MWCNTs

3.3.1.1 X-ray Diffraction Results

The X-ray diffraction results of fresh MWCNTs, ox-MWCNTs, Fe/MWCNTs and polymer-modified PNIPAM:Fe/MWCNTs nanocomposites are shown in Figure 56. In the case of fresh MWCNTs, the main diffraction peaks of (002) and (100) appear at 2θ = 25.9° and 43.0°, respectively, which relate to fresh MWCNTs [241]. No significant changes were observed in the case of ox-MWCNTs, the main peaks remained almost unchanged after oxidizing of MWCNTs in the presence of strong acids.

The main diffraction peaks of Fe/MWCNTs are (220), (311), (400), (422), (511) and (440) corresponding to 2θ = 31.41°, 36.0°, 44.53°, 53.25°, 57.01° and 63.11°, respectively, which belong to magnetite [230]-[231]. According to the XRD results, an amorphous structure for the polymer PNIPAM was observed, the main broad peak is shown at 2θ = 19.04°. After adding PNIPAM to Fe/MWCNTs nanocomposites, the peak

of PNIPAM appeared and this confirmed the preparation of PNIPAM modified Fe/MWCNTs nanocomposites [244] (Figure 56).

The peaks at 2θ = 21.5° and 23.9° in the XRD pattern of PE:Fe/MWCNTs corresponded to the (110) and (200) diffraction peaks of polyethylene, respectively [244], as is shown in Figure 56. However, XRD patterns of polystyrene-modified Fe/MWCNTs could not show the peak at 2θ =19.4° as reported in literature [245] due to the amorphous structure of polymer and/or its small amount in sample.

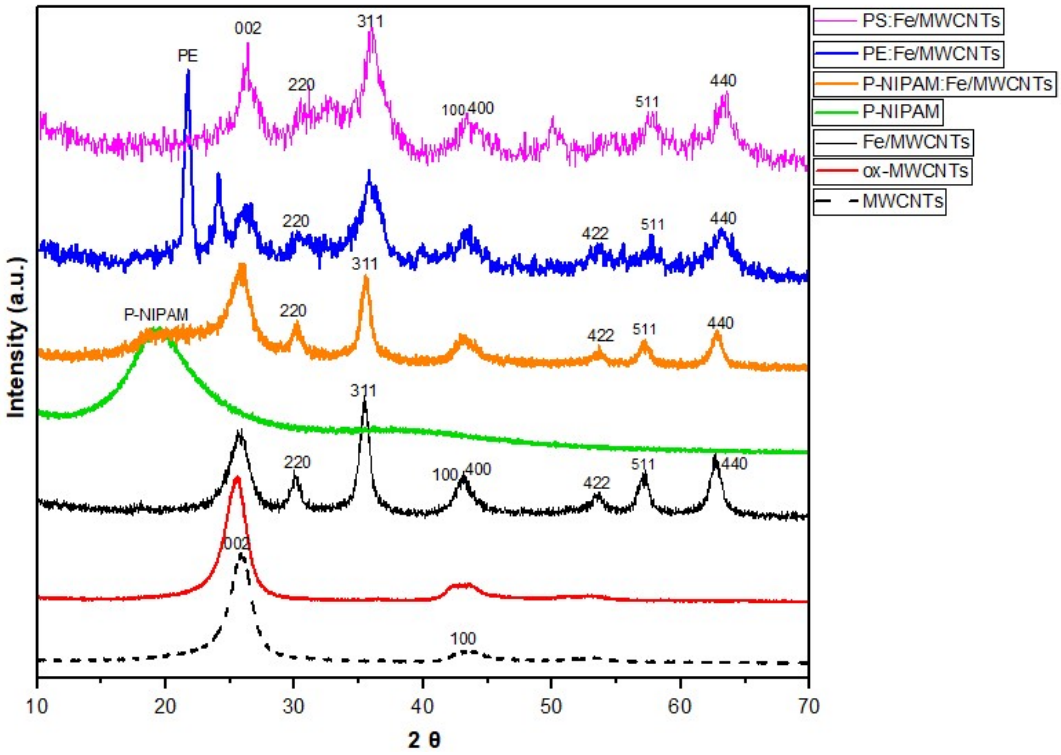

Figure 56. XRD patterns of fresh MWCNTs, ox-MWCNTs, Fe/MWCNTs, PNIPAM:Fe/MWCNTs, PE:Fe/MWCNTs, and PS:Fe/MWCNTs

3.3.1.2 Fourier transform infrared spectroscopy results

FTIR spectra of MWCNTs, ox-MWCNTs, Fe/MWCNTs, PE:Fe/MWCNTs as prepared and PE:Fe/MWCNTs after kerosene adsorption are shown in Figure 57.

For ox-MWCNTs Figures 57 and 58, the band at 3426 cm^{-1} is relating to O-H of stretching vibration of hydroxyl groups. While the peak at 1625 cm^{-1} relates to vibration of C=O carboxyl bond of –COOH group. The peaks at 2925 cm^{-1}, 2845 cm^{-1}, 1460 cm^{-1} and 1395 cm^{-1} are attributed to the asymmetric and symmetric C-H stretching, C=C aromatic ring stretching and C-C stretching for MWCNTs respectively [246], [247].

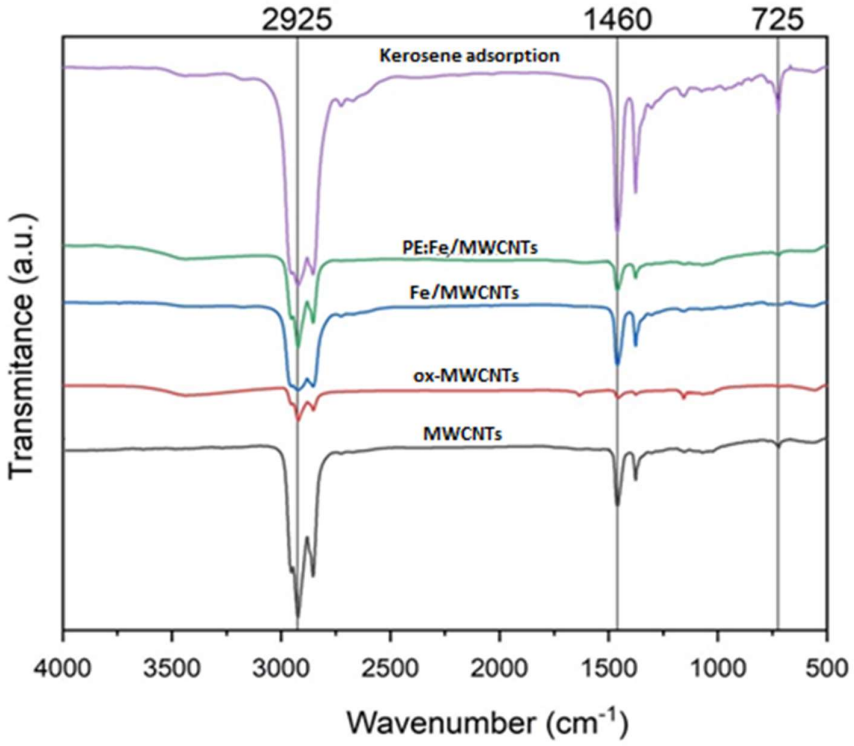

Figure 57 FTIR spectrum for MWCNTs, ox-MWCNTs, Fe/MWCNTs, PE:Fe/MWCNTs and PE:Fe/MWCNTs after kerosene adsorption

The PE:Fe/MWCNTs after kerosene adsorption is shown in Figure 57. The peaks at the 2850–3000, 1460, and 725 cm^{-1} wavelengths represent the chemical functional groups of $–CH_2–$ stretching, –CH bending, and $–CH_2–$ rocking vibration of the aliphatic hydrocarbon, respectively [248]. Kerosene a part of paraffin but has trace of unsaturated hydrocarbons as double bonds or unsaturated cyclic compounds can be adsorbed onto surface of polymer composite (PE:Fe/MWCNTs) [249], [250].

FTIR spectra of MWCNTs, ox-MWCNTs, Fe/MWCNTs, PS:Fe/MWCNTs as prepared and PS:Fe/MWCNTs after toluene adsorption are shown in Figure 58. Table 13 shows the peaks assignments and type of vibration for fresh, oxidized and polysterene modified Fe/MWCNTs and PS:Fe/MWCNTs after toluene removal from water.

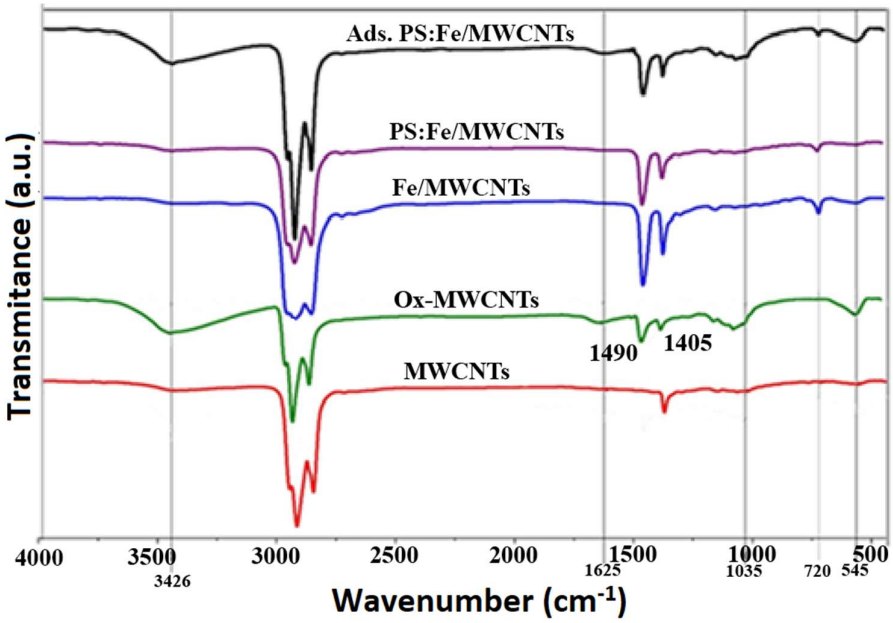

Figure 58 FTIR spectrum for fresh MWCNTs, ox-MWCNTs, Fe/MWCNTs, PS:Fe/MWCNTs and PS:Fe/MWCNTs after toluene adsorption

Table 13 FTIR peak assignments for fresh, oxidized and polysterene modified Fe/MWCNTs [251], [252]

Sample	FTIR wavenumber (cm^{-1})	Band assigment
Fresh MWCNTs	3425 cm^{-1}	O-H stretching vibration of of hydroxyl groups
	2925 cm^{-1} 2845 cm^{-1} 1490 cm^{-1} 1395 cm^{-1}	asymmetric C-H stretching symmetric C-H stretching C=C stretching vibration C-C stretching vibration
ox-MWCNTs	1625 cm^{-1} 3420 cm^{-1}	C=O stretching of –COOH grop O-H stretching of –COOH group
PS:Fe/MWCNTs after toluene adsorption	2925 cm^{-1} 2845 cm^{-1} 1035 cm^{-1}	C-H stretching of aromatic ring C-H stretching of -CH_3 group C-H bending in plane

3.3.1.3 Raman spectroscopy results

The Raman spectra of fresh MWCNTs, ox-MWCNTs, Fe/MWCNTs and polymer-modified PE:Fe/MWCNTs nanocomposites are shown in Figure 59. Three sharp peaks were observed at 1338 cm^{-1}, 1580 cm^{-1} and 2695 cm^{-1} in all samples corresponding to the disorder-induced band (D band), the Raman-allowed tangential mode (G band) and the second-order harmonic band (G' band, Graphite) which attributed to the overtone of the D band, respectively. The D mode indicates the disordered features of the carbon and

defect sites in the curved graphite sheet and sp3 carbons along with other impurities, while the G mode is associated with the ordered crystalline graphite in the MWCNTs in agreement with references [29] and [234]. The Raman spectrum shows a second-order harmonic G' band (graphite) at 2930 cm^{-1} correspondinlg to the D + G band. The PE:Fe/MWCNTs are presented in Figure59 with a higher peak at 2650 cm^{-1}, attributed to the bonding of the polymer in MWCNTs, while this peak decreases when kerosene is adsorbed, as can be seen in Figure 59 [235]-[236].

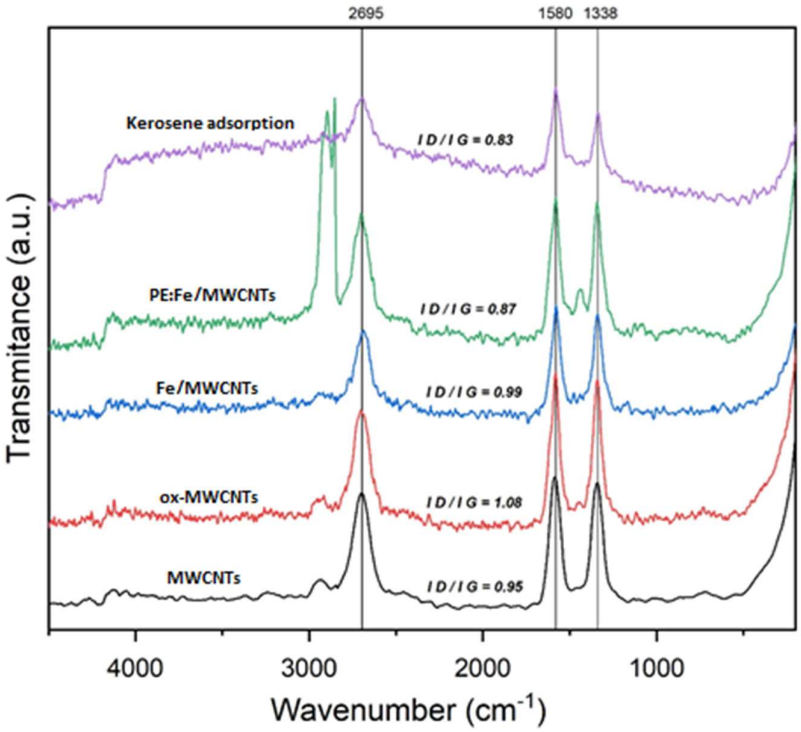

Figure 59. Raman spectra of fresh MWCNTs, ox-MWCNTs, Fe/MWCNTs, PE:Fe/MWCNTs and PE:Fe/MWCNTs after kerosene adsorption

Raman spectroscopy and adsorption test results for polystyrene-modified Fe/MWCNTs samples are shown in Figure 60. According to the results of PS:Fe/MWCNTs with regard to the removal of toluene from water, the D, G and G' bands changed, moreover, after polystyrene was added and PS:Fe/MWCNTs nanocomposites formed, the D, G and G' bands significantly increased in intensity with regard to the bonding of the polymer in Fe/MWCNTs. Meanwhile, the bands continued to increase in intensity and another band appeared at 4150 cm^{-1}, which refers to the adsorption of toluene over PS:Fe/MWCNTs nanocomposites, as can be seen in Figure 60.

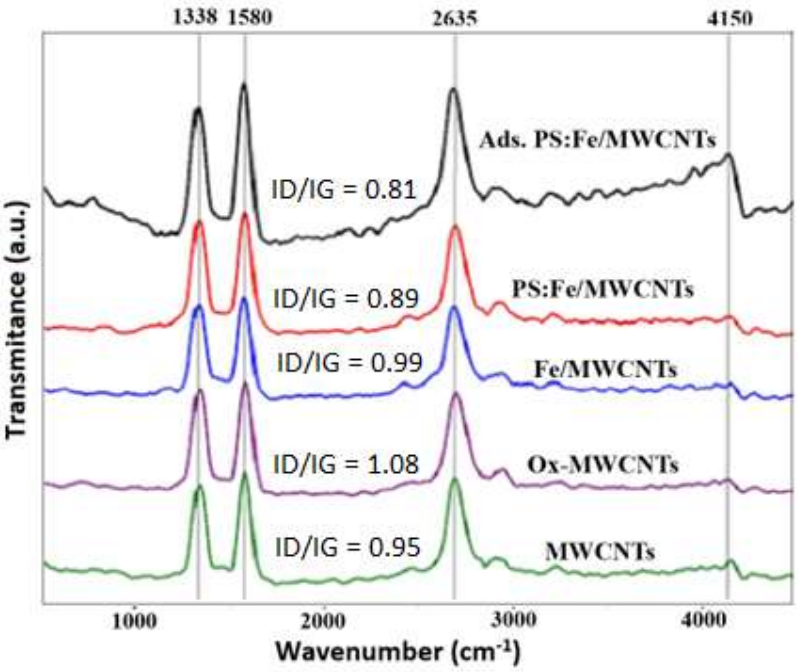

Figure 60. Raman spectra of fresh MWCNTs, ox-MWCNTs, Fe/MWCNTs, PS:Fe/MWCNTs and PS:Fe/MWCNTs after toluene adsorption cm^{-1}

3.3.1.4 Scanning and transmission electron microscopy results

SEM and TEM results of fresh MWCNTs, ox-MWCNTs, Fe/MWCNTs and polystyrene-modified Fe/MWCNTs nanocomposites were recorded. By taking into consideration that the magnetite nanoparticles were prepared over MWCNTs in a ratio of 1:1, according to Figures 61a-b, Fe_3O_4 particles prepared over MWCNTs were well within the nanoscale and nanotubes were observed. Therefore, it is clear that the shape of the carbon nanotubes during oxidation of the MWCNTs with a strong acid and even after the magnetite doped MWCNTs nanocomposites had been prepared is unaffected. After modification of Fe:MWCNTs with polysterene, PS:Fe/MWCNTs were very clearly shown in Figures 61c-d, indicating that the mixing of polystyrene while preparing the nanocomposites facilitates the agglomeration of the MWCNTs and magnetite particles.

The TEM images in Figures 61e-f show magnetite-modified MWCNTs nanocomposites. The images indicate that the tubular shape of the CNTs during the preparation and when the magnetite nanoparticles pass over MWCNTs is unaffacted. Figure 61f shows that the diameter of the magnetite nanoparticles is less than 10 nm. Figures 61f-g present the PS:Fe/MWCNTs nanocomposites from which it was also observed that the agglomeration of the magnetite particles occurred following the addition

of polystyrene. Similarly, the tubular shape of the CNTs remains unaffected even after preparation of the nanocomposites had been completed.

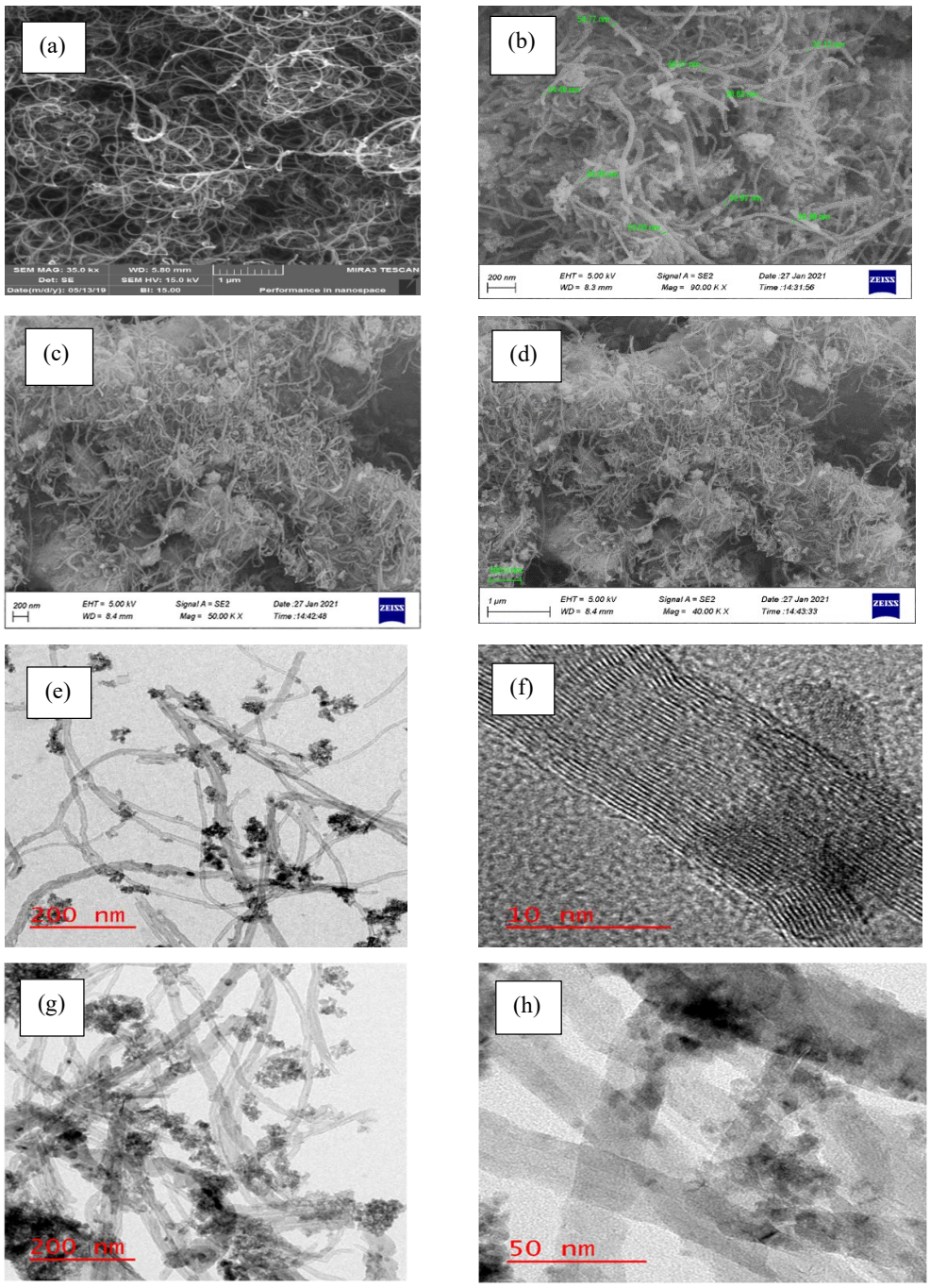

Figure 61 SEM images of Fe/MWCNTs (a and b), PS:Fe/MWCNTs (c and d) and TEM images of Fe/MWCNTs (e and f), PS:Fe/MWCNTs (g and h)

The SEM images of fresh MWCNTs, ox-MWCNTs, Fe/MWCNTs and polyethylene-modified Fe/MWCNTs are presented in Figure 62. The shape of the MWCNTs can be

distinctly observed in the SEM image of fresh MWCNTs (Figure 62). The shape of the MWCNTs was not significantly affected by the oxidation of HNO_3 (Figure 62b). The magnetite nanoparticles deposited on MWCNTs can be observed in the SEM images of Fe/MWCNTs (Figures 62c-d). Furthermore, the agglomeration of polyethylene over Fe/MWCNTs can be observed in the SEM images of PE:Fe/MWCNTs (Figure 62e-f). The TEM images of Fe/MWCNTs (Figures 62g-h) illustrate that magnetite modified the MWCNTs and consisted of nanoparticles (Figure 62h).

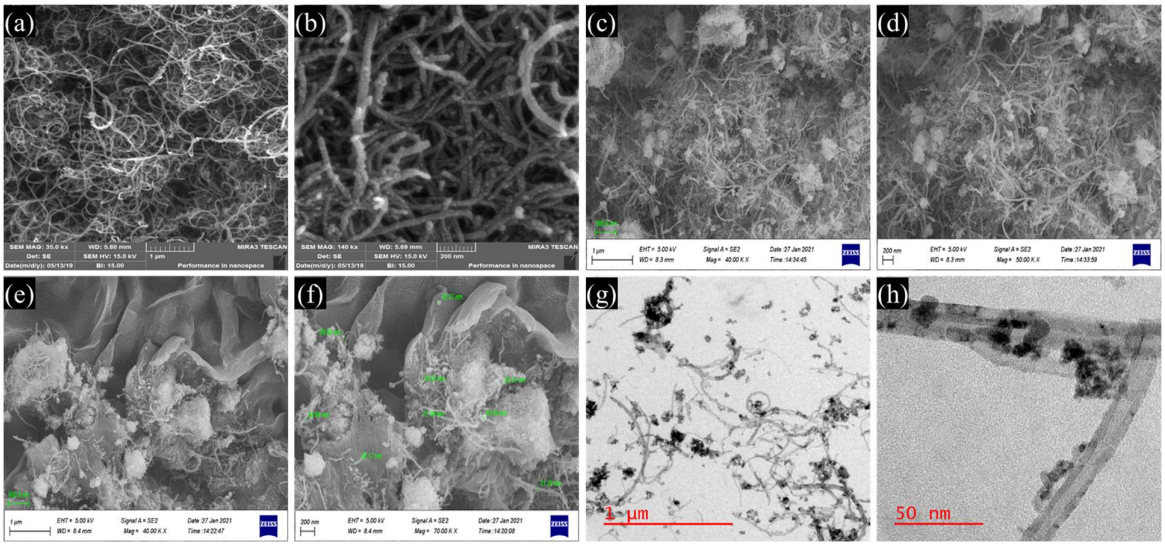

Figure 62 SEM images of (a) fresh MWCNTs, (b) ox-MWCNTs, (c) and (d) Fe/MWCNTs, (e) and (f) PE:Fe/MWCNTs and TEM images of (g) and (h) Fe/MWCNTs

SEM and TEM images of PNIPAM-modified Fe/MWCNTs are shown in Figure 63. SEM and TEM micrographs show the microstructure and morphology of the PNIPAM:Fe/MWCNTs nanocomposites. As is shown in Figures 63a and d, that is, the SEM and TEM images of fresh MWCNTs, the diameter of the nanotubes is between 20 and 30 nm. Figures 63b and e clearly show that the magnetite nanoparticles cover the outer surface of the nanotubes, where the presence of magnetite and CNTs is also evident according to the characteristic EDX lines of iron, oxygen and carbon atoms (Figure 63g).

The SEM and TEM images of PNIPAM:Fe/MWCNTs nanocomposites are presented in Figures 63c and f, where the homogeneous distribution of magnetite nanoparticles is similar to the previously described “fresh” MWCNTs samples. However, the addition of the polymer PNIPAM may cause agglomeration.

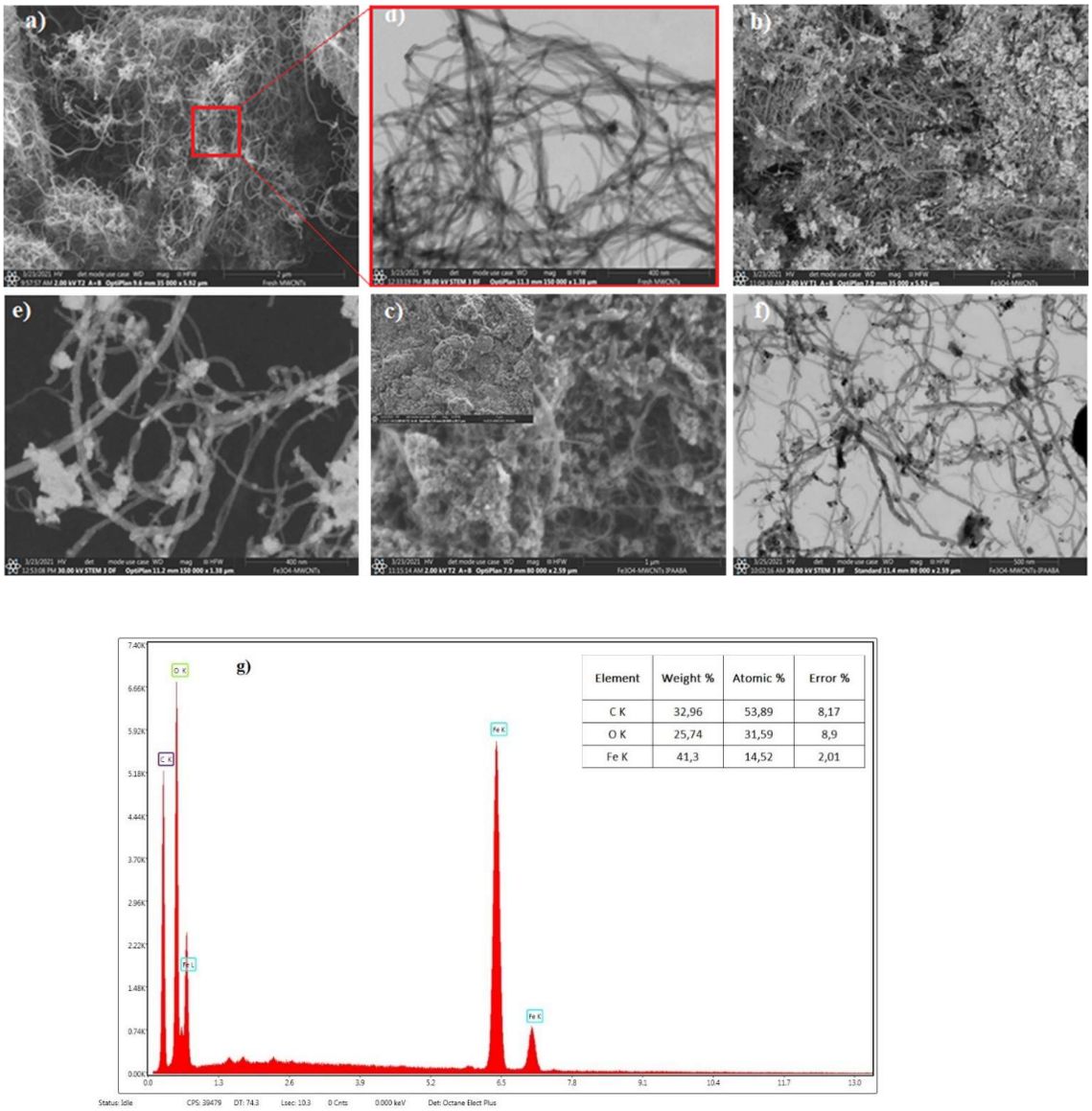

Figure 63 SEM image of fresh MWCNTs (a), Fe/MWCNTs (b), P-NIPAM:Fe/MWCNTs (c); TEM images of resh MWCNTs (d), Fe/MWCNTs (e), P-NIPAM:Fe/MWCNTs (f) amd EDX spectrum for Fe/MWCNTs (g)

3.3.1.5 Low temperature nitrogen adsorption results

The total and micropore surface areas, S_{BET} and S_{micro}; the pore volumes of pores with diameters of between 1.7 and 300 nm and their corresponding micropore volumes, $V_{1.7–300\ nm}$ and V_{micro}; as well as the average pore size, D_{av}, of fresh ox-MWCNTs, Fe/MWCNTs and polymer-modified Fe/MWCNTs samples are summarized in Table 14. The total surface area of fresh MWCNTs was 161 m^2/g, which was higher than that reported by the supplier of 120 m^2/g.

Table 14: Surface areas, pore volumes and average pore sizes of fresh MWCNTs, ox-MWCNTs, Fe/MWCNTs and polymer-modified Fe/MWCNTs

	Samples	S_{BET} m^2/g	$V_{1.7–300\ nm}$ cm^3/g	S_{micro} m^2/g	V_{micro} cm^3/g	D_{av} nm
1	MWCNTs	161	0.7932	22.86	0.0096	17.9
2	ox-MWCNTs	146	1.1142	13.9	0.0053	26.0
3	Fe/MWCNTs	233	0.5737	0	0	8.5
4	PE:Fe/MWCNTs	86	0.2969	0	0	10.1
5	PE:Fe/MWCNTs after kerosene adsorption	73	0.2711	0	0	11.2
6	PS:Fe/MWCNTs	136	0.3372	0	0	8.5
7	PS:Fe/MWCNTs after toluene adsorption	129	0.3075	0	0	7.6
8	PNIPAM polymer	13	0.0619	0	0	15.0
9	PNIPAM:Fe/MWCNTs	73.2	0.3534	0	0	15.8
10	PNIPAM:Fe/MWCNTs after kerosene adsorption	71.1	0.3377	0	0	16.0

The oxidation of MWCNTs with HNO_3 led to the formation of –COOH and –OH functional groups, which can block micropore openings [234] and cause a slight reduction in the BET surface area (S_{BET}) from 161 (for fresh MWCNTs) to 146 m^2/g (for ox-MWCNTs) as discussed in Part 3.2.1.8. The surface area and micropore volume of the ox-MWCNTs were 40% and 55% smaller, respectively, than those of the fresh MWCNTs (Table 14). These results were attributed to the formation of defect sites on the surface of ox-MWCNTs, resulting in CNT splitting [256]. Acid treatment also effects the total pore volume of MWCNTs, as is shown in Figure 64.

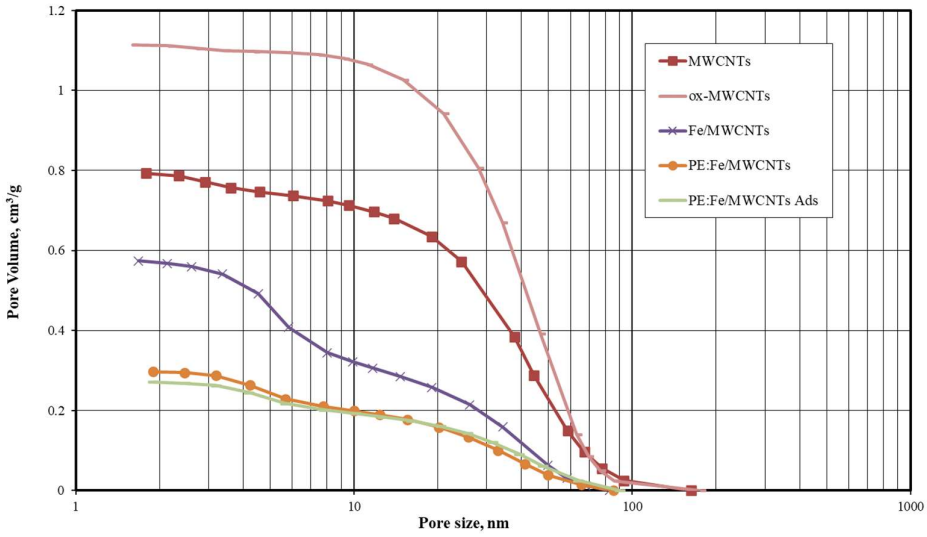

Figure 64. Cumulative mesoporous volume distribution of prepared MWCNTs, ox-MWCNTs, Fe/MWCNTs and PE:Fe/MWCNTs as well as of PE:Fe/MWCNTs after kerosene adsorption

In this study, the deposition of magnetite on MWCNTs caused an increase in their surface areas. S_{BET} of Fe/MWCNTs (233 m^2/g) was higher than that of ox-MWCNTs, indicating that magnetite, which was dispersed over the surface of MWCNTs, blocked their micropores. Moreover, new pores with a diameter of 5 nm were formed on the surface of the ox-MWCNTs (Figures 65 and 66).

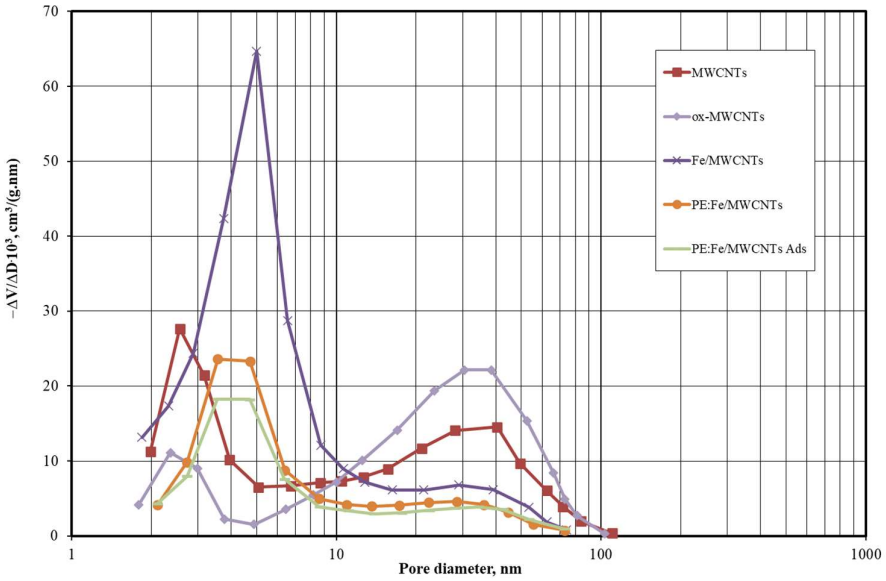

Figure 65. Pore volume distribution of MWCNTs, ox-MWCNTs, Fe/MWCNTs, PE:Fe/MWCNTs and PE:Fe/MWCNTs after kerosene adsorption

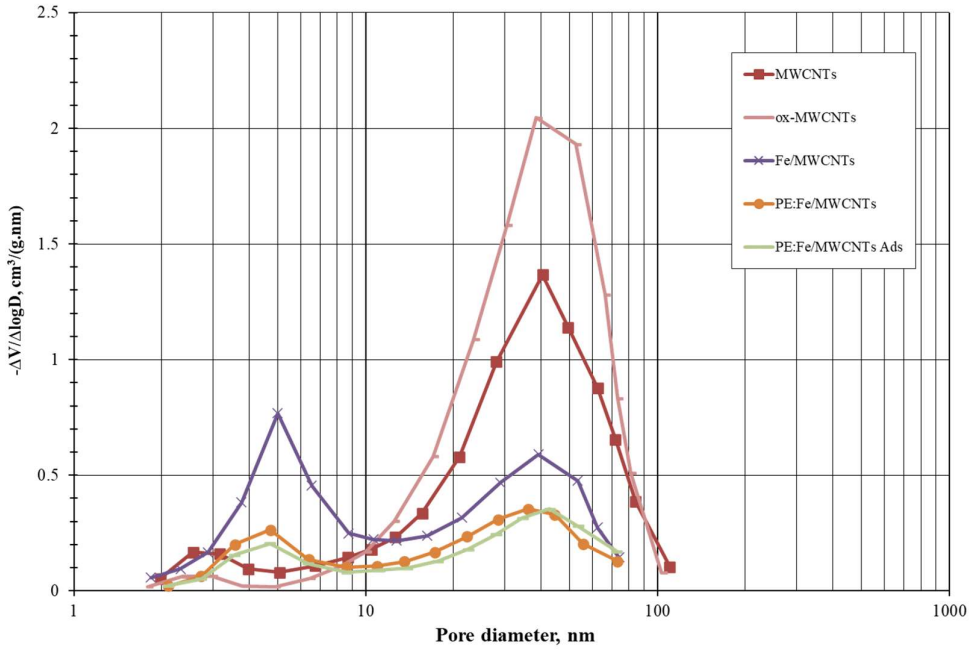

Figure 66. Logarithmic pore volume distribution of MWCNTs, ox-MWCNTs, Fe/MWCNTs, PE:Fe/MWCNTs and PE:Fe/MWCNTs after kerosene adsorption

The addition of the polymers polyethylene and PNIPAM to the Fe/MWCNTs led to significantly greater reductions in the surface area of Fe/MWCNTs (from 233 to 86 and 73 m^2/g, respectively) and their pore volumes (from 0.5737 to 0.2969 and 0.3534 cm^3/g, respectively) in comparison with the depositon of polystyrene on Fe/MWCNTs (Table 14). The addition of polystyrene decreased the surface area of Fe/MWCNTs by 42% from 233 to 136 m^2/g. The incorporation of polymers caused the agglomeration of Fe/MWCNTs, as confirmed by the SEM images of polymers:Fe/MWCNTs (Figures 61-63), thereby decreasing the number of smaller (<10 nm) and larger (>10 nm) pores in the samples as well as decreasing their surface area.

A further reduction in the S_{BET} of polymer-modified Fe/MWCNTs was observed following the adsorption of kerosene/toluene. This suggested that the absorption of pollutants took place on the surface of the adsorbent and the fraction of adsorbed hydrocarbon molecules remained in the bulk of the sample after desorption at 105 °C under a vacuum.

3.3.1.6 Thermogravimetric analysis

The thermogravimetric analyses of fresh MWCNTs, ox-MWCNTs, Fe/MWCNTs and PNIPAM:Fe/MWCNTs were carried out. The reduction in mass of the fresh MWCNTs

sample is small and monotonous up to 200 °C, indicating a minimal quantity of water adsorbed by the hydrophobic sample, while a major reduction in mass is observed between 430 and 733 °C (Figure 67/a, Table 15), which can be associated with the thermal degradation of MWCNTs [213]. The asymmetric shape might be an indication of the different thermal stabilities of MWCNTs as a result of different wall thicknesses present in the sample. Above 1,000 °C, the relatively high amount of residual mass (11.88%) indicates the impurity of the sample, most probably due to the presence of residues of transition metal catalysts used during catalytic chemical vapour deposition [226].

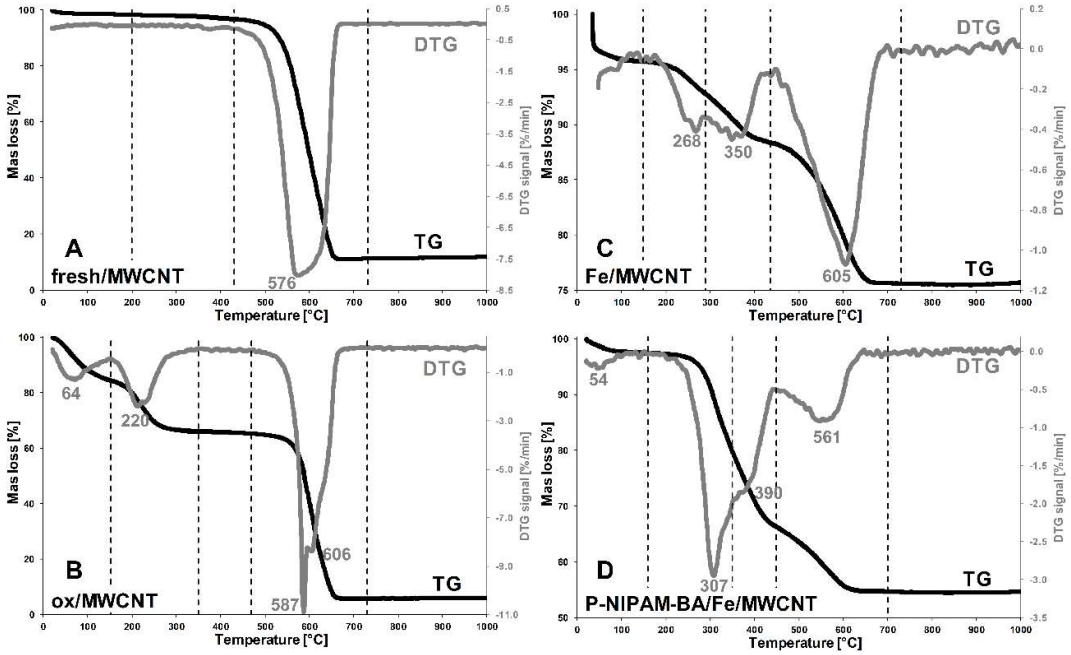

Figure 67. TG and DTG curves of MWCNTs-prepared adsorbent materials

Treatment of the MWCNTs with strong acids (H_2SO_4 and HNO_3) results in the oxidation of the carbon structure along with the formation of surface carboxyl, carbonyl and hydroxyl groups. Acid treatment can also remove amorphous carbon impurities and decrease the amount of catalytic residues [214] [237]. The first mass loss step of ox-MWCNTs (22-153°C, Figure 67b, Table 15) can be attributed to the removal of adsorbed water, indicative of the increased hydrophilic character of the functionalized CNT surface. The second mass loss step (153-350°C) is related to the elimination of residues of oxygenated surface functional groups. A major mass loss step can be identified between 470 and 730°C. As a result of acid treatment, the full width half maximum (FWHM) is reduced and the asymmetric nature of MWCNTs decomposition (470-597°C,

597-730°C) becomes more prominent by removing smaller or less stable CNT nanoparticles. The notably lower residual mass after being heated at 1,000 °C (6.04%) can be related to the dissolved parts of the transition metal catalyst residues following acid treatment.

At temperatures of up to 50 °C, the Fe/MWCNTs sample shows a very rapid reduction in the amount of volatile compounds adsorbed on its surface (Figure 67b, Table 15). A major decomposition step can be identified between 150 and 435 °C, consisting of two overlapping processes (150-290 °C, 290-435 °C). In the absence of oxygen, the small mass gain typical of magnetite oxidation from Fe_3O_4 to Fe_2O_3 and the theoretical mass gain of 3.45% for pure Fe_3O_4 [258] is not expected. No other changes in mass are expected for magnetite [258]. Although the mass loss due to the oxygen-containing functional groups of modified MWCNTs structures is also expected in this region, the Fe modification [259] increased the thermal stability of these functional groups (increased FWHM and DTG maxima from 220 to 268°C, Figure 67c). The thermal decomposition of residual CTAB, used as an additive in the preparation of Fe/MWCNTs, can also take place in this region between 150 and 300°C, while the thermal decomposition of CTAB decomposition products can take place up to 400 °C [260]. The pyrolysis of the CNT structure is observed between 435 and 730 °C with a more uniform rate of decomposition as a result of Fe_3O_4 modification. The relatively high amount of residual mass (75.69%) having been heated at 1,000 °C indicates the additional presence of stable iron oxides in the sample.

The PNIPAM:Fe/MWCNTs sample exhibits a small mass loss step (21-160 °C) related to dehydration (Figure 67, Table 15). A significant mass loss is observed between 160 and 450 °C, consisting of two separate processes. This can be related to the thermal degradation of the PNIPAM polymer. TG analyses confirmed that the polymer was successfully attached to the surface: 34 wt% PNIPAM: 55 wt% Fe/MWCNTs. The removal of the surface functional groups from the CNT surface is also visible, while the decomposition of the carbon backbone takes place between 450 and 700 °C.

Table 15. Mass loss data of MWCNTs samples from the TG curves

Sample	T_{start} (°C)	T_{end} (°C)	Total mass loss (%)	Total mass loss (mg)	Mass loss step (%)	Mass loss step (mg)
Fresh MWCNTs	20	200	1.69	0.1	1.69	0.1
	200	430	3.23	0.2	1.54	0.1
	430	733	88.72	5.9	85.49	5.7
	733	1015	88.12	5.8	-0.60	0.0
	Initial mass: 6.632 mg			Residual mass: 0.788 mg (11.88%)		
ox-MWCNTs	22	153	15.61	1.0	15.61	1.0
	153	350	33.94	2.2	18.33	1.2
	350	470	34.73	2.3	0.79	0.1
	470	730	94.11	6.2	59.38	3.9
	730	1015	93.96	6.2	-0.15	0.0
	Initial mass: 6.612 mg			Residual mass: 0.399 mg (6.04%)		
Fe/MWCNTs	30	150	4.30	0.3	4.30	0.3
	150	290	7.56	0.5	3.26	0.2
	290	435	11.62	0.8	4.06	0.3
	435	730	24.34	1.6	12.72	0.8
	730	1015	24.31	1.6	-0.03	0.0
	Initial mass: 6.508 mg			Residual mass: 4.926 mg (75.69%)		
PNIPAM:Fe/MWCNTs	21	160	2.55	0.2	2.55	0.2
	160	350	20.16	1.4	17.61	1.2
	350	450	33.72	2.3	13.56	0.9
	450	700	45.33	3.1	11.61	0.8
	700	1015	45.33	3.1	0.00	0.0
	Initial mass: 6.736 mg			Residual mass: 3.683 mg (54.67%)		

3.3.2 Adsorption results

3.3.2.1 Kerosene adsorption over PE:Fe/MWCNTs

The removal of kerosene over MWCNTs, ox-MWCNTs, Fe/MWCNTs and PE:Fe/MWCNTs samples was studied in order to better understand the absorption mechanism of saturated hydrocarbons over the polyethylene-modified Fe/MWCNTs surface. Adsorption experiments were performed using adsorbents by increasing the adsorption time from 15 to 30, 60 and 120 min. The initial kerosene concentration, mixture volume of kerosene and adsorbent mass were 200 mg/L, 50 mL and 2 mg, respectively.

Since the kerosene concentration was at its lowest after adsorption on PE:Fe/MWCNTs (Figure 68b), the adsorption efficiency of the PE:Fe/MWCNTs nanocomposite was the highest of all analyzed adsorbents (Figure 68a).

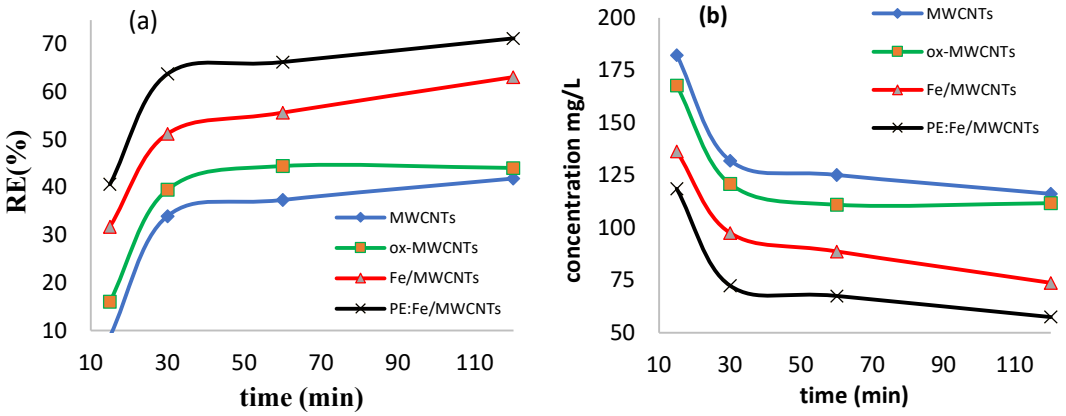

Figure 68. Time evolution of the (a) kerosene removal efficiency (*RE*) on MWCNTs, ox-MWCNTs, Fe/MWCNTs and PE:Fe/MWCNTs as well as the (b) kerosene concentration in kerosene–water mixtures treated with MWCNTs, ox-MWCNTs, Fe/MWCNTs and PE:Fe/MWCNTs

The decrease in kerosene concentration in the PE:Fe/MWCNTs-treated kerosene–water sample and the increase in the kerosene RE of the PE:Fe/MWCNTs adsorbent were significant until an adsorption equilibrium was reached after 60 min (Figures 68a-b). The kerosene RE of PE:Fe/MWCNTs after 120 min did not increase significantly. The kerosene removal efficiencies and kerosene adsorption capacities of fresh MWCNTs, ox-MWCNTs, Fe/MWCNTs and PE:Fe/MWCNTs are summarized in Table 16.

Table 16. Kerosene removal efficiency (*RE*) and kerosene adsorption capacity (q_e) of MWCNTs, ox-MWCNTs, Fe/MWCNTs and PE:Fe/MWCNTs after 120 mins

Adsorbent	RE (%)	q_e (mg/g)
fresh MWCNTs	41.8	2092
ox-MWCNTs	44.0	2204
Fe/MWCNTs	63.1	3154
PE:Fe/MWCNTs	71.2	3560

PE:Fe/MWCNTs yielded the highest kerosene removal efficiency (71.2%) and the highest kerosene adsorption capacity (3560 mg/g) of all the analyzed samples (Table 16). Therefore, the effect of the amount of adsorbent on the adsorption of kerosene from water was evaluated using the PE:Fe/MWCNTs nanocomposite.

Different amounts of PE:Fe/MWCNTs adsorbent within the range of 1.0–6.0 mg were added to kerosene–water mixtures and the removal of kerosene was followed for 60 min at room temperature. The results revealed that the highest removal efficiency observed using 4 mg sorbent, but the optimum recommended mass of PE:Fe/MWCNTs adsorbent in a kerosene–water mixture with a kerosene concentration of 200 mg/L was 2.0 mg since the removal efficiency did not increase significantly when the sorbent increased to 4 mg (Table17).

Table 17. Kerosene removal efficiency (RE) of the PE:Fe/MWCNT nanocomposite adsorbent using various adsorbent doses as well as at different pHs and temperatures of the mixture

Adsorbent dose (mg)	RE (%)	pH of mixture	RE (%)	Temperature of mixture (°C)	RE (%)
1	19	2	82	15	57
2	***64***	***5***	***81***	25	81
4	67	7	62	***35***	***86***
6	65	8	53	45	85
-	-	10	51	-	-

The effect of temperature on the kerosene removal efficiency of PE:Fe/MWCNTs was analyzed within the temperature range of 15–45 °C. The adsorption time, adsorbent mass, shaking speed, kerosene concentration and volume of the kerosene–water mixture were 60 min, 2.0 mg, 240 rpm, 200 mg/L and 50 mL, respectively. The results indicated that the optimum temperature for kerosene adsorption on PE:Fe/MWCNTs was 35 °C (308 K) (Table 17).

The effect of pH on the kerosene removal efficiency of PE:Fe/MWCNTs from water was evaluated within the pH range of 2–10. The adsorption time, adsorbent mass, shaking speed, kerosene concentration, volume of the kerosene–water mixture and solution temperature were 60 mins, 2.0 mg, 240 rpm, 200 mg/L, 50 mL and 35 °C, respectively. The result showed that the removal efficiency for pH values 2 and 5 remanes almost stable (RE=82 and 81%). Therefore the optimum pH value for kerosene adsorption on PE:Fe/MWCNTs is recommended to be 5 since it is closer to neutral pH value (Table17).

3.3.2.2 Kerosene adsorption over PNIPAM:Fe/MWCNTs

Kerosene removal over MWCNTs, ox-MWCNTs, Fe/MWCNTs and PNIPAM:Fe/MWCNTs samples were studied in order to better understand the absorption

mechanism of saturated hydrocarbons over the surface of PNIPAM-modified Fe/MWCNTs. The adsorption process of kerosene is affected by several factors. In this paper, different ranges of time (Time = 0-75 min), dose (m = 2.5-12.5 mg), temperature (T = 20-50 °C) and pH (pH = 3.5-10.0) were used to examine the optimum parameters using PNIPAM:Fe/MWCNTs nanocomposites for the removal of kerosene from water.

Changes in removal efficiency of kerosene against time are presented in Figure 69. The optimum adsorption time was determined to be 45 mins. Treatment with PNIPAM:Fe/MWCNTs nanocomposites yielded the highest removal efficiency of kerosene and the lowest kerosene concentration in comparison with fresh MWCNTs, ox/MWCNTs and Fe/MWCNTs. The removal efficiencies after 45 mins were 45, 55, 69 and 87%, while the adsorption capacities were 2.2, 2.8, 3.4 and 4.4 g/g sorbent for MWCNTs, ox-MWCNTs, Fe/MWCNTs and P-NIPAM:Fe/MWCNTs, respectively, after a process time of 45 mins.

The PNIPAM:Fe/MWCNTs nanocomposite sorbent was regenerated after batch adsorption as a result of sonication with distilled water before being heated at 160 °C using a vacuum oven. Four kerosene adsorption cycles were repeated using regenerated PNIPAM:Fe/MWCNTs. The RE of kerosene was similar after each adsorption cycle. In this work, different parameters such as adsorption time, adsorbent dose, temperature and the pH of the mixture were studied to determine the optimum conditions for kerosene removal from water over PNIPAM:Fe/MWCNTs.

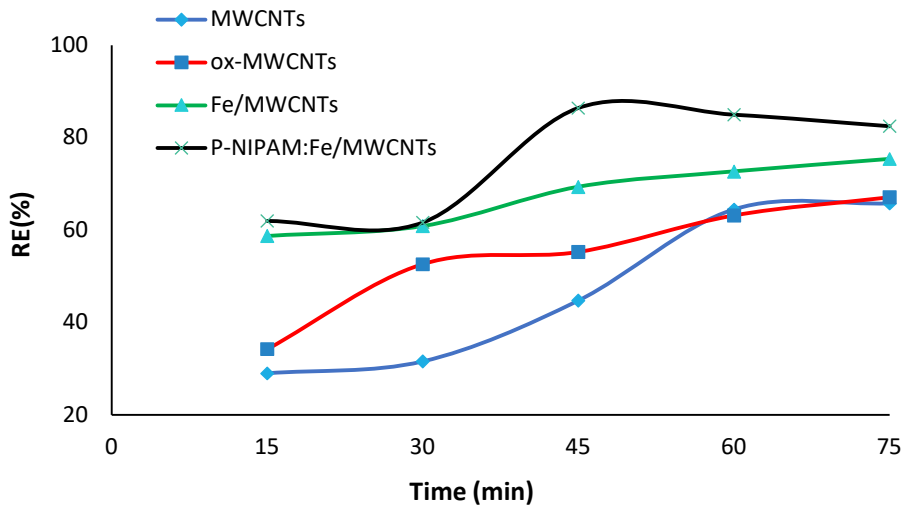

Figure 69 Time evolution of removal efficiency of kerosene from water treated with MWCNTs, ox-MWCNTs, Fe/MWCNTs, and P-NIPAM:Fe/MWCNTs (C =500 mg/L, V=50 mL, Time=75 min, m=5 mg, pH=7, T=20 °C)

The effect of changing the adsorbent dosage within the range of 2.5–12.5 mg was studied. The highest kerosene removal efficiency, namely 86.0%, from water was achieved using an adsorbent dosage of 5 mg, as is shown in Figure70:

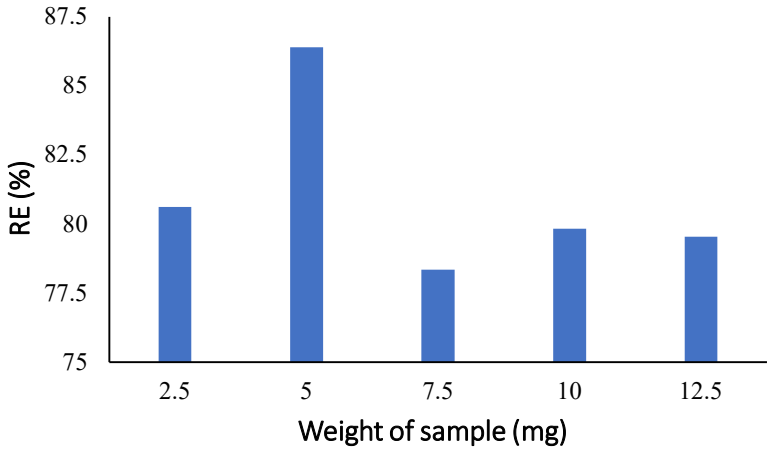

Figure 70 Effect of changing P-NIPAM:Fe/MWCNTs adsorbent dosage on removal efficiency of kerosene from water (C =500 mg/L, V=50 mL, Time=45 min, pH=7, T= 45 °C)

The effect of the temperature on the kerosene removal efficiency was studied at 20, 30, 40 and 50 °C. By increasing the temperature of the solution resulted in an increase in the kinetic energy of the molecules. Therefore, the collision energy between them was increased and the rate of adsorption rose due to the binding of the kerosene onto the adsorbent. The results showed that 40 °C was the optimum temperature to achieve the maximum removal efficiency of kerosene from water over PNIPAM:Fe/MWCNTs, namely 92.3%, as is shown in Figure 71.

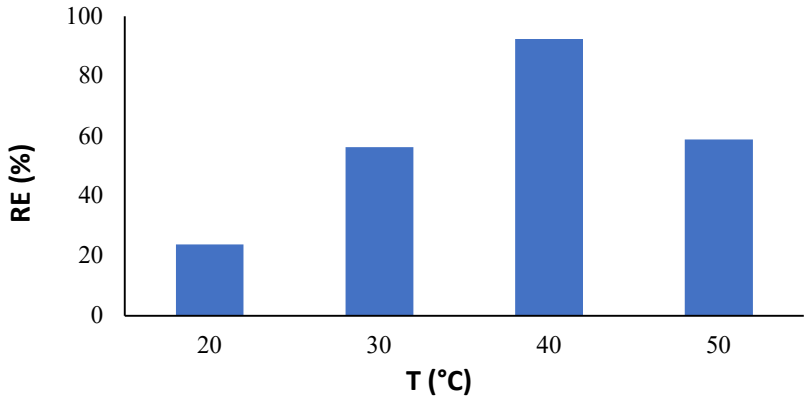

Figure 71 Effect of changing model solution temperature on removal efficiency of kerosene over P-NIPAM:Fe/MWCNTs (C =500 mg/L, V=50 mL, Time=45 min, m=5 mg, pH=7)

The effect of a pH of 3.5, 5.5, 7.0, 8.5 and 10.0 on the removal of kerosene from water was studied. The results showed that at a pH of 3.5, the highest adsorption capacity of kerosene of 95.1% over PNIPAM:Fe/MWCNTs was achieved, as is shown in Figure 72.

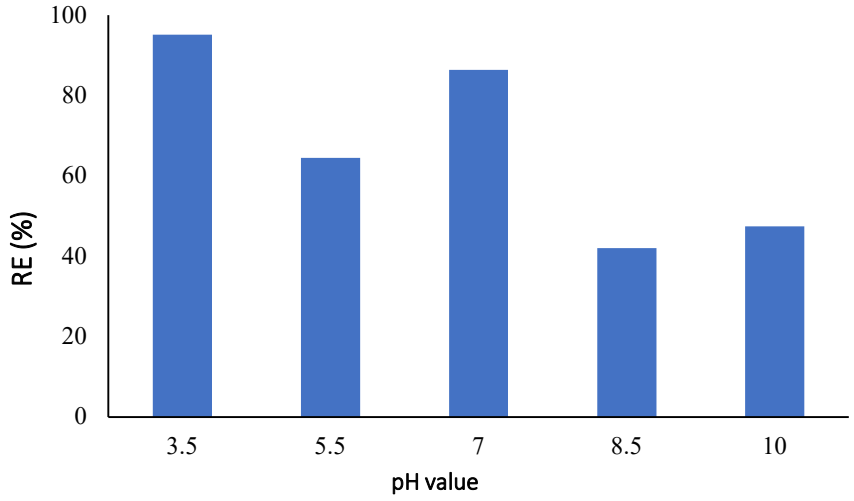

Figure 72 Effect of changing pH of model solution on the removal efficiency of kerosene over P-NIPAM:Fe/MWCNTs (C =500 mg/L, V=50 mL, Time=45 min, m=5 mg, T= 40 °C)

3.3.2.3 Results of toluene adsorption over PS:Fe/MWCNTs

The removal of toluene over MWCNTs, ox-MWCNTs, Fe/MWCNTs and PS:Fe/MWCNTs samples was studied in order to better understand the absorption mechanism of saturated hydrocarbons over a polystyrene-modified Fe/MWCNTs surface. Different contact times were used (15, 30, 60 and 120 min) to study the removal of toluene over samples of adsorbent. The changes in toluene concentration were monitored by HPLC. The initial concentration of toluene was 50 mg/L in all batch experiments, the volume of the solution was 50 mL and the mass of the samples was 2 mg. The decrease in the concentration of toluene and the removal efficiency of toluene from water against the process time are presented in Figures73 and 76. PS:Fe/MWCNTs achieved both the highest removal efficiency and decrease in the concentration of toluene after 60 mins compared to fresh MWCNTs, ox-MWCNTs and Fe/MWCNTs. The highest removal efficiency of 62% was achieved using PS:Fe/MWCNTs. The removal efficiency and sorption capacity mg/g using fresh and modified MWCNTs for toluene removal from water were: MWCNTs (240 mg/g and 19%) < Fe/MWCNTs (450 mg/g and 36%) < PS:Fe/MWCNTs (769 mg/g and 62%). Adding polystyrene to magnetic MWCNTs were improved their efficiency and capacity for toluene removal from water.

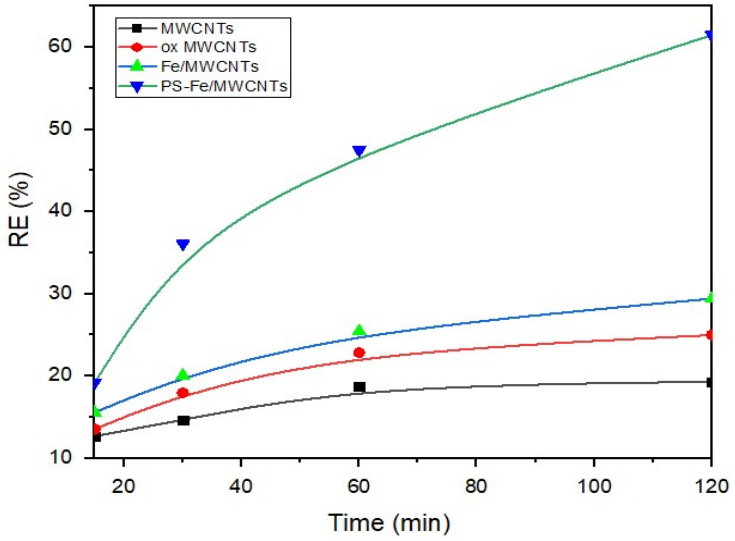

Figure 73 Adsorption removal efficiency of toluene from water against time over MWCNTs, ox-MWCNTs, Fe/MWCNTs and PS:Fe/MWCNTs

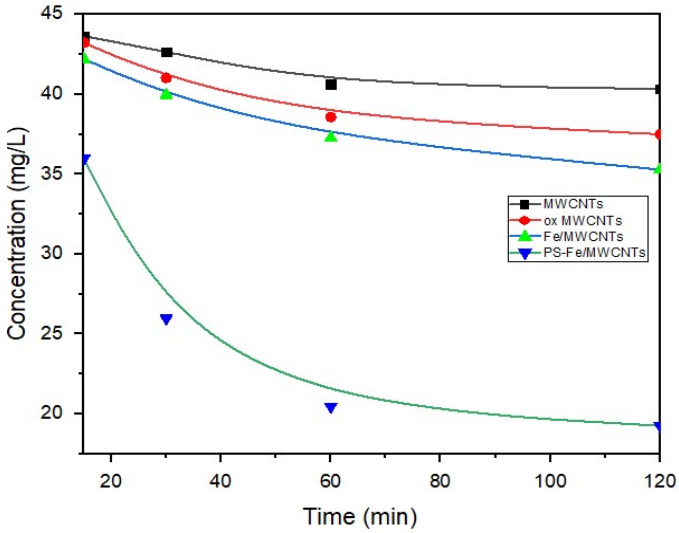

Figure 74 Concentration of toluene from water againt the time over MWCNTs, ox-MWCNTs, Fe/MWCNTs and PS:Fe/MWCNTs

The effect of different adsorbent dosages was studied using PS:Fe/MWCNTs. A set of adsorbent dosages, namely 1, 2, 4 and 6 mg of PS:Fe/MWCNTs, was used to study the removal efficiency of toluene from water. The following parameters were used during the adsorption step: T = 60 mins, V = 50 mL and $C_{toluene}$ = 50 mg/L at ambient temperature. Even though the results show that the highest removal efficiency of toluene from water was achieved using an adsorbent dosage of 4 mg, when 2 mg of PS:Fe/MWCNTs was used, the removal efficiency of toluene from water was 61%, while the removal efficiency

using 4 mg led to an insignificant increase (64 %), as can be seen in Figure 75. Therefore, the best results are achieved when an adsorbent dose of 2 mg is used.

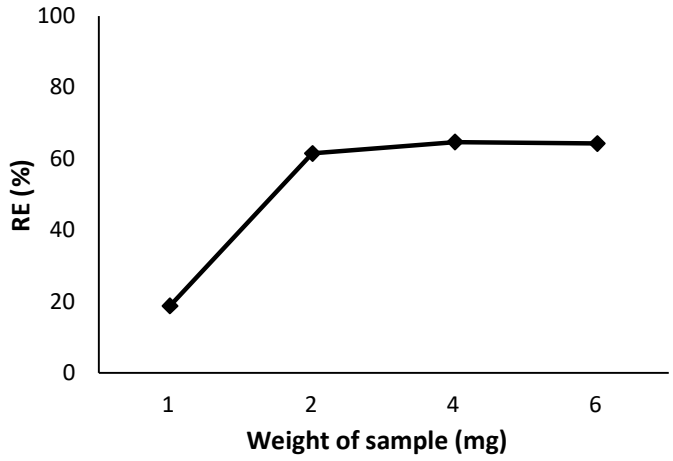

Figure 75 Effect of changing the adsorbent dosage on the removal efficiency of toluene over the PS:Fe/MWCNTs

The effect of the pH on the removal of toluene from water was studied. The solutions were immersed in various pHs (2, 5, 7, 8 and 10) over a PS:Fe/MWCNTs sample using the following parameters: T = 60 min, V = 50 mL, m_{ads} = 2 mg, $C_{toluene}$ = 50 mg/L at ambient temperature, shaking speed = 240 rpm. Although the highest removal efficiency of toluene, namely 84 %, over PS:Fe/MWCNTs was achieved when the pH was 2, the results showed that when the pH of the solution was 5, the optimum removal efficiency of toluene from water of 77% was achieved, as is shown in Figure76. Therefore, instead of using a solution with a pH of 2, a pH of 5 can achieve a removal efficiency of toluene from water of 77%. Furthermore, using a solution with a pH close to 7 is better than one around a pH of 2 since a slight increase in the removal efficiency can be achieved, as can be seen in Figure 76.

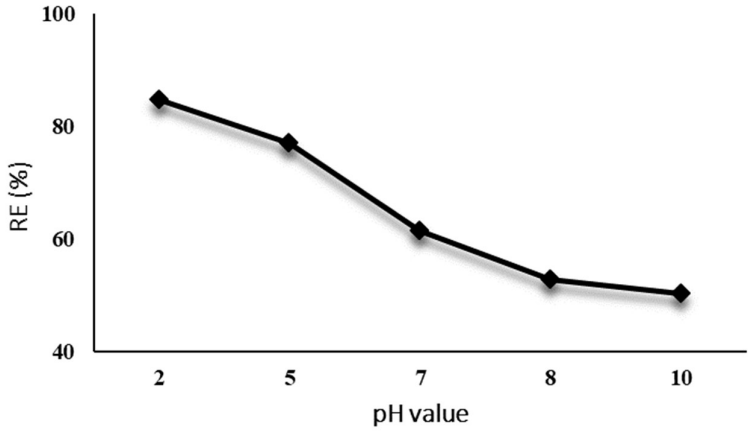

Figure 76 Effect of changing pH of the solution on the removal efficiency of toluene over the PS:Fe/MWCNTs

The effect of temperature on the removal efficiency of toluene over PS:Fe/MWCNTs was studied at 15, 25, 35 and 45 °C. The following parameters were used: T = 60 min, V = 50 mL, m_{ads} = 2 mg, $C_{toluene}$ = 50 mg/L, shaking speed = 240 rpm. The results showed that the optimum temperature was 35 °C for the removal of toluene from water over PS:Fe/MWCNTs as the highest removal efficiency was achieved, that is, 86%, as is shown in Figure 77.

Some adsorption capacities and removal efficiencies of hydrocarbons reported in the literature over adsorbent materials, including polymer-modified Fe/MWCNTs, are summarized in Table18. The data revealed that the prepared and used polymer-modified Fe/MWCNTs in this work have similar adsorption parameters to those reported and can be successfully applied for the treatment of hydrocarbon-contaminated water. The optimum paramers for toluene removal from water using PS:Fe/MWCNTs were: Tsolution = 35 °C, Time = 60 min, m = 2 mg, pHsolution =5 for C = 50 mg/L, V = 50 mL.

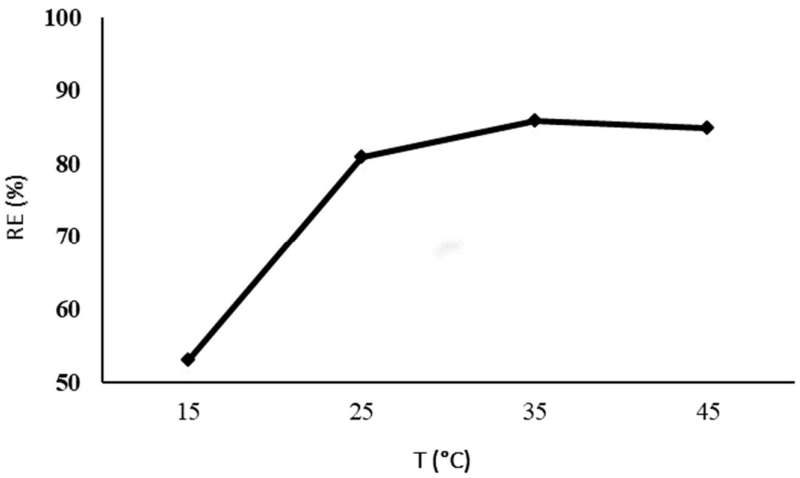

Figure 77 Effect of changing temperature of the solution on the removal efficiency of toluene over the PS:Fe/MWCNTs

Table 18. Adsorption capacities (q_t) and removal efficiencies (RE) of hydrocarbons using several adsorbents

Adsorbent materials	Pollutants	Pollutant concentration (mg/L)	Adsorbent dose (mg)	q_t (mg/g)	RE (%)	Reference
PE:Fe/MWCNTs	Kerosene	200	2	3559	72	This study
PS:Fe/MWCNTs	Toluene	50	2	768	62	This study
P-NIPAM:Fe/MWCNTs	Kerosene	500	2.5	4320	87	This study
Activated carbon	Kerosene	700	1500	370	98	[261]
Agricultural waste barley	Toluene	1150	12500	576	94	[262]
Lauric acid-treated oil palm leaves	Oil	5600	1000	1200	-	[263]
CNTs–iron oxide	Toluene	61	50	382	70	[264]
KOH activated coconut shell based carbon treated with NH_3	Toluene	250	100	357	-	[265]
CNTs–iron oxide	p-Xylene	48	50	460	90	[264]
Microemulsified MWCNTs	Kerosene	500	10	4700	94	[266]
Nipa palm fruit fiber	Kerosene	0.008	20	1.43	66	[267]
Hydrophobic alumina	Crude oil	500	2500	200	-	[268]

3.3.3 Kinetic and isotherm studies on the removal of kerosene and toluene from water over polymer-modified Fe/MWCNTs

A study of adsorption kinetics was carried out to determine the rate of removal of kerosene and toluene from water. From the results, it is clear that initially adsorption is rapid [269] due to surface phenomena such as the physical affinity between the adsorbent and the kerosene or toluene concentration, moreover, due to the availability of vacant sites, it reaches its maximum after 120 min. The kinetic analysis concerning the adsorption of hydrocarbons was carried out using pseudo first-order equation (11), pseudo second-order equation (12) and intraparticle diffusion equation (13). The graphical representations of three kinetic models are shown in Figures78 and 79 a to c.

The best fit kinetic model with regard to the experimental results of kerosene and toluene adsorption was the the pseudo second-order model, as is indicated by the highest values of their linear regression curves, namely $R^2 = 0.9961$ and $R^2 = 0.9910$ for kerosene and toluene, respectively. In the case of kerosene adsorption over PE:Fe/MWCNTs, qe cal = 3,333 mg/g which is very close to the value measured experimentally of qt exp = 3,560 mg/g. While in the case of toluene adsorption over PS:Fe/MWCNTs, qe cal = 1,111 mg/g, which is higher than the experimental value of qt exp = 769 mg/g, supported that the results in figure73 and 74, the highly removal efficiency and lowest continoues decrease in toluene concentration during process time even after 120 min. It supported the fact that the prepared composite need more time to be reached close to 1,111 mg/g.

The results of kinetic studies are in agreement with the previously reported adsorption mechanisms of saturated and aromatic hydrocarbons [270]–[272].

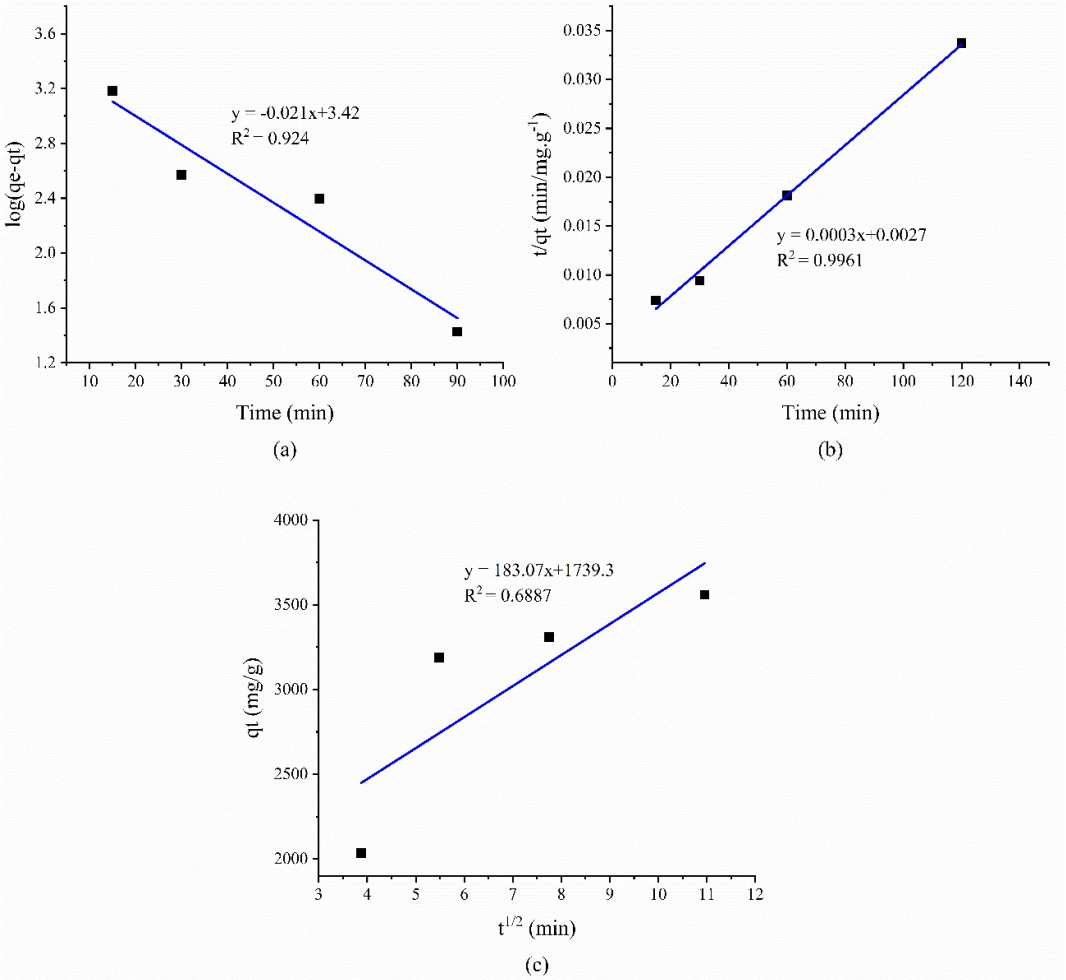

Figure 78 Pseudo-first order plot (a), pseudo-second order plot (b), itra-particle plot (c) for kerosene adsorption over PE:Fe/MWCNTs

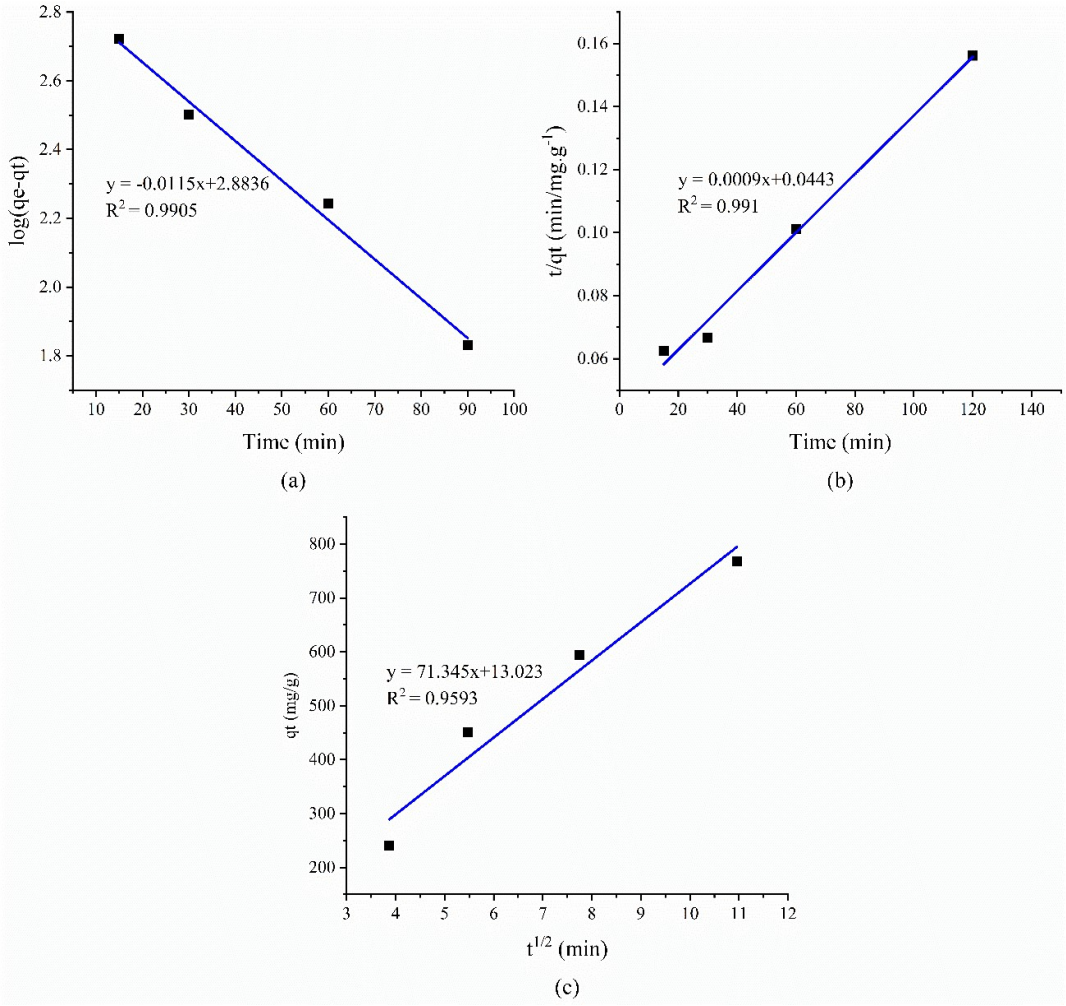

Figure 79. Pseudo-first order plot (a), pseudo-second order plot (b), itra-particle plot (c) for toluene adsorption over PS:Fe/MWCNTs

The validity of the Langmuir and Freundlich isotherm models for kerosene and toluene can be verified by the linear plots of *Ce/qe against Ce* and *log qe against log Ce* of equations (14) and (15), respectively, as are presented in Figures 80 and 81. The isotherm data of the present adsorption systems can be fitted well by the Langmuir equation for the adsorption of kerosene over PE:Fe/MWCNTs with a correlation coefficient (R^2) of 0.9949 (Figure 80a) and by the Freundlich equation for the adsorption of toluene over PS:Fe/MWCNTs with an R^2 of 0.9443 (Figure 81b):

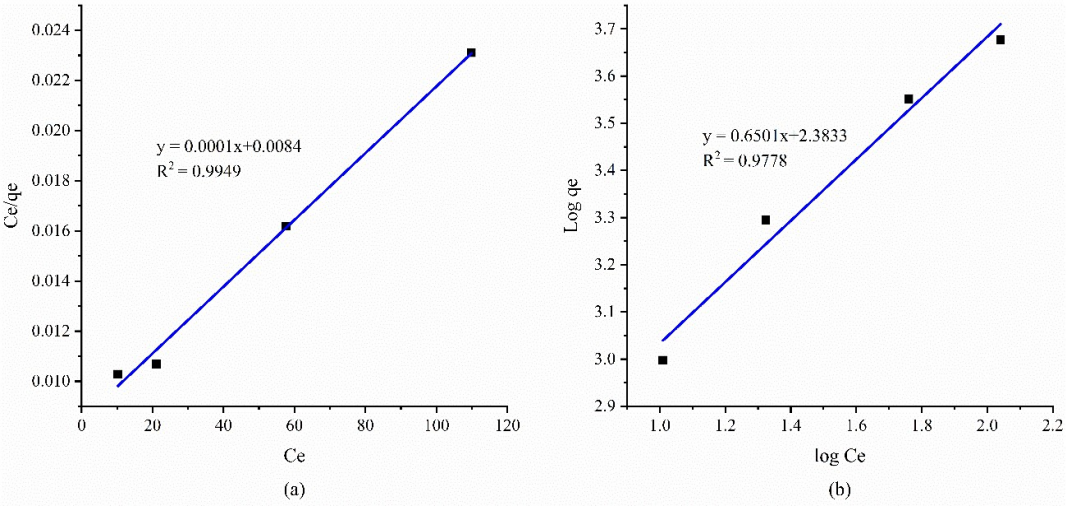

Figure 80 Langmuir isotherm plot (a) and Freundlich isotherm plot (b) for kerosene adsorption onto PE:Fe/MWCNTs

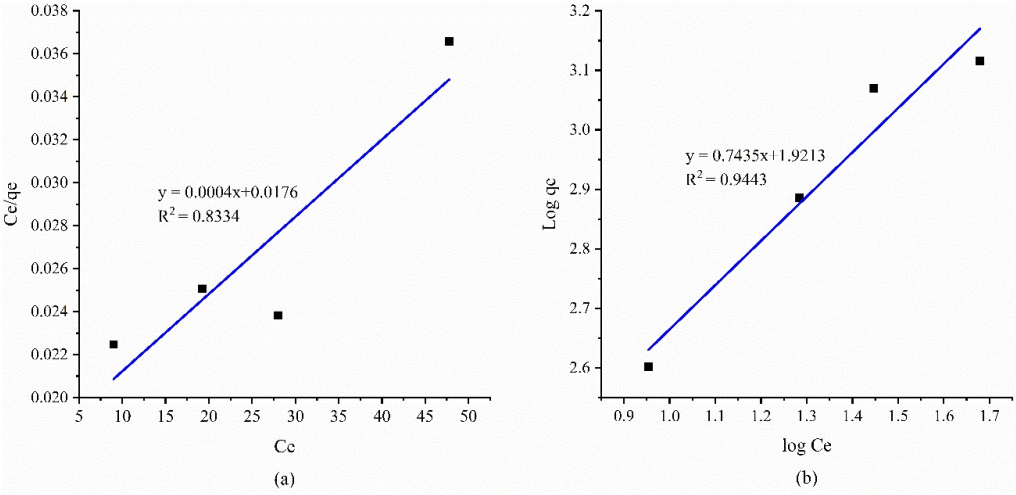

Figure 81 Langmuir isotherm plot (a) and Freundlich isotherm plot (b) for toluene adsorption onto PS:Fe/MWCNTs

3.3.4 Adsorption mechanism of hydrocarbons on polymer-modified Fe:MWCNTs

Adsorption mechanism of kerosene over fresh MWCNTs, ox-MWCNTs, PE:Fe/MWCNTs and PNIPAM:Fe/MWCNTs. In the case of fresh and polymer-modified MWCNTs, saturated hydrocarbons can be adsorbed on the surface of the adsorbent via a CH···π interaction, which is one of the weak non-covalent hydrogen bonds, between a hydrogen atom in kerosene and a carbon atom in MWCNTs, PNIPAM or polyethylene.

In the case of ox-MWCNTs, a hydrogen bond could be formed between the oxygen atom in the carboxyl group and a hydrogen atom in alkanes.

Furthermore, in the case of Fe/MWCNTs, due to the presence of metal oxides, the formation of a hydrogen bond between the oxygen atom in magnetite and a hydrogen atom in kerosene is possible. In addition, the adsorption of hydrocarbon molecules to the surface of the adsorbent could also be due to van der Waals forces. The adsorption of kerosene over PE:Fe/MWCNTs and PNIPAM can be seen in Figures82a and b.

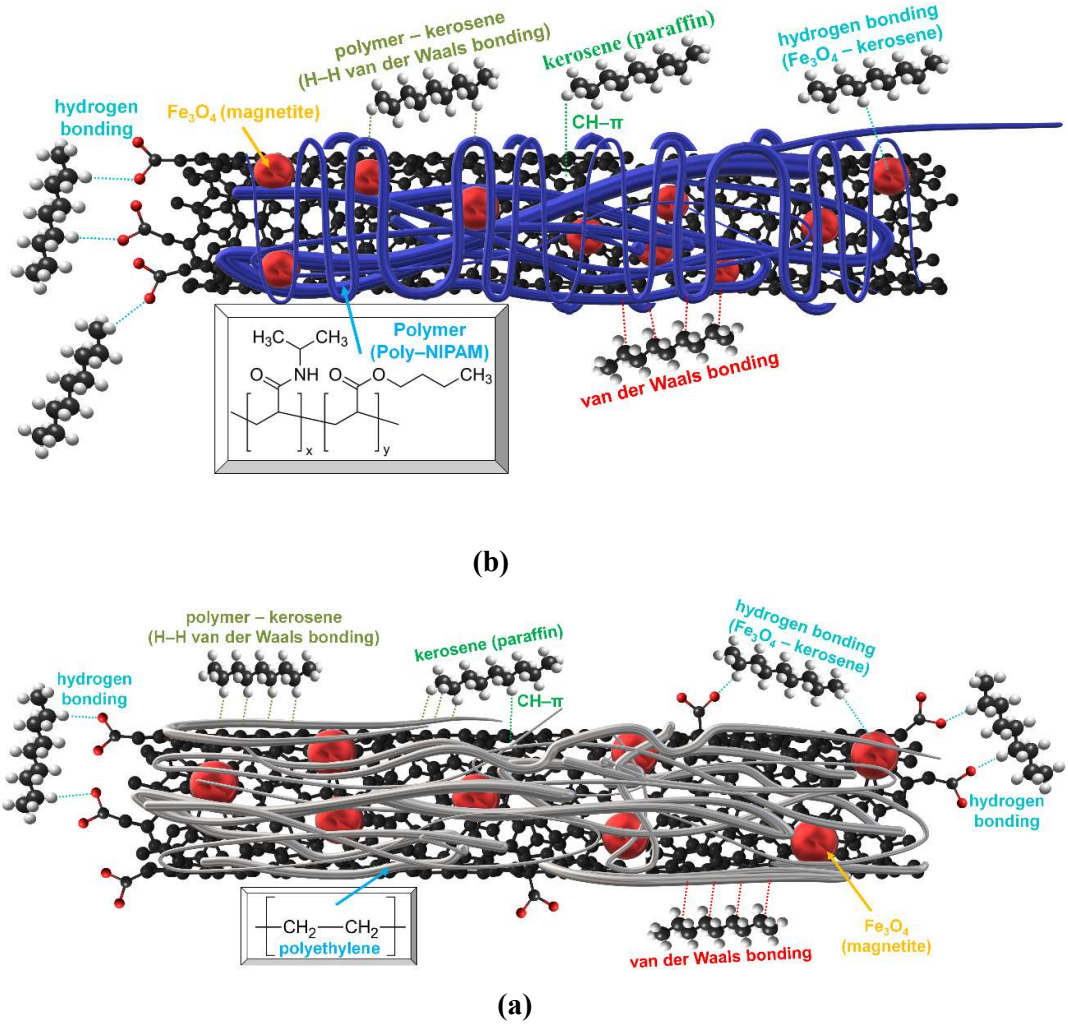

Figure 82 Proposed mechanism of kerosene adsorption over (a) PE:Fe/MWCNTs and (b) P-NIPAM: Fe/MWCNTs

The proposed mechanism of the removal of toluene from water is shown in Figure83.

In the case of fresh MWCNTs, π-π interactions between CNTs and the aromatic rings of toluene occur [7]. In the presence of magnetite, cation−π interactions were proposed between the π electrons of aromatic rings and the iron cation-terminated activated

surfaces (acid-base interaction) [273]. The affinity for toluene increases over PS:Fe_3O_4/MWCNTs following the formation of π–π bonds between the benzene ring of the adsorbed aromatic compound and the polymer [274], [275].

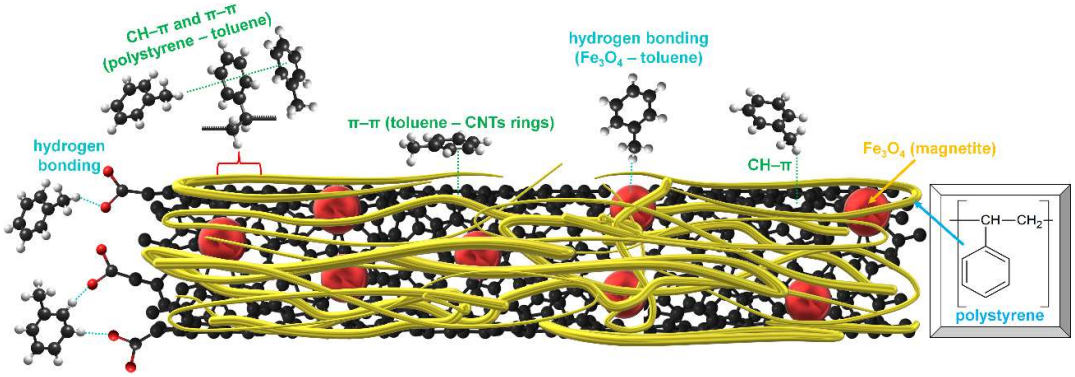

Figure 83 Proposed mechanism of toluene adsorption over PS:Fe/MWCNTs

4. Conclusion

The ability of vanadium pentoxide as well as various metal oxide-doped MWCNTs nanocomposites and polymer-modified Fe/MWCNTs to remove the pollutants kerosene, toluene and methylene blue dye from water was studied in this work. Below a summary of the physicochemical characterization and adsorption test results for each group of adsorption materials studied in this work is given.

4.1. V_2O_5 nanoparticles for the removal of methylene blue dye from Water

The vanadium pentoxide nanoparticles were successfully synthesized via a hydrothermal method and treated at different temperatures (90, 250, 500 and 750 °C). The nanostructure of the prepared material was confirmed by FTIR spectroscopy, X-ray diffraction and SEM. It was confirmed by FTIR spectroscopy that the surface dehydroxylation and decomposition of the starting material, NH_4VO_3, occurred at 250°C. A similar observation was made by a TG study, which showed that the thermal decomposition of NH_4VO_3 to V_2O_5 occurs between 293 and 355 °C.

The XRD data showed that the orthorhombic crystalline structure of V_2O_5 begins to form even at a lower temperature of 90 °C and a well-defined crystalline structure was observed at 750°C. Heat treatment leads to a significant increase in the crystallinity of the samples, meanwhile, can cause a decrease in the surface area of the sample. The reduction in the surface area of the adsorbent can explain the decrease in the sorption activity of the sample annealed at 750°C with regard to the removal of methylene blue.

On the other hand, the obtained results indicated that the heat-treated vanadium samples within a temperature range of between 90 and 750 °C exhibit rather high adsorption capacities varying from 15 to 27 mg/g in terms of MB removal from water. It was found that an increase in the adsorbent dosage up to 60 mg and a slight increase in the temperature of the solution (V=30 mL) from RT to 45 °C yielded the maximum removal efficiency of MB, namely 98% (20 mg/L) from water after 40 mins of treatment.

The applicability and suitability of two common kinetic models was tested. The results of which demonstrated that the best fit of experimental adsorption data was to the pseudo second-order model, while the Freundlich inhomogeneous adsorption model fitted with a higher correlation coefficient with regard to the equilibrium adsorption studies. The presented work showed that V_2O_5 nanoparticles could be applied for the removal of organic industrial pollutants, e.g. methylene blue dye, from wastewater.

4.2. Metal oxide-doped MWCNTs nanocomposites for the removal of kerosene and MB dye from water

The results showed that the novel MWCNTs-based adsorbents are nanomaterials with a major crystalline phase consisting of graphene layers of the MWCNTs. The EDX and TGA studies confirmed the successful deposition/attachment of metal oxides on the surface of MWCNTs. The deposition of TiO_2 (5wt%), V_2O_5 (4-5wt%) and CeO_2 (6-12wt%) as well as V:Ti (~2wt%), V:Ce (8-1wt%) and V:Ce:Ti (6-7wt%) oxides over the oxidized MWCNTs brought about the blockage of some micropores. Meanwhile, the surface area remained relatively high (115–135 m^2/g) for adsorption treatment.

The experimental results showed that the adsorption capacity and removal efficiency of kerosene from water over MWCNTs increased after adding metal oxides. The highest adsorption parameters (RE = 85% and qt = 4271 mg/g) were obtained for vandia and ceria mixed over MWCNTs (V:Ce/MWCNTs). The obtained results were further analysed through kinetic models, which demonstrated that the best fit of experimental data was to the pseudo second-order model. Furthermore, the intraparticle diffusion model showed the influence of the boundary layer effect, thereby confirming the significance of the rate-limiting step on the surface sorption of kerosene. The attachment of hydrocarbons to the adsorbent surfaces in all likelihood occurs through the formation of weak hydrogen bonds.

Metal oxide nanoparticles and their composites modified by MWCNTs were also successfully applied for the removal of methylene blue dye from water. It was found that V/MWCNTs exhibited the best degree of MB adsorption compared with fresh MWCNTs, ox-MWCNTs, Ce/MWCNTs and Ti/MWCNTs. Based on the adsorption results over V/MWCNTs, different vanadia nanocomposite-modified MWCNTs were prepared and studied for the removal of MB from water. The results showed that the V:Ce/MWCNTs achieved the best degree of MB removal from water compared with other preparations. The optimum parameters using V:Ce/MWCNTs for MB removal from water are as follows: contact time = 25 mins, temperature = 45 °C, adsorbent mass = 9.0 mg, solution volume = 20 mL, MB concentration = 20 mg/L and shaking speed = 240 rpm. The adsorption mechanisms of MB can be interpreted mainly by π-π and electrostatic interactions in the case of oxidized and metal oxide-doped MWCNTs.

The studied metal oxide-doped MWCNTs can be considered as potential nanoadsorbents for the depollution control of hydrocarbons (kerosene, oil, etc.) and methylene blue dye, moreover, could open new avenues for their application.

4.3. Polymer-modified Fe/MWCNTs for the removal of hydrocarbons from water

The successful deposition of Fe_3O_4 over MWCNTs (Fe/MWCNTs) was achieved by coprecipitation and proven by SEM/TEM and EDX analyses. Magnetite containing adsorbent materials can be easily separated after the adsorption step using a magnetic field. It was observed that the modification of Fe:MWCNTs using the polymers (polyethylene, polystyrene or PNIPAM) enchanced the adsorption properties of carbon nanotube-based samples.

PE:Fe/MWCNTs increased the removal efficiency and adsorption capacity of kerosene from 42% and 2092 mg/g to 71% and 3560 mg/g, respectively. The optimum parameters of the treatment process were as follows: V=50 mL, $C_{kerosene}$=200 mg/L, contact time = 60 min, $T_{solution}$=35 °C, m_{ads}=2.0 mg, $pH_{solution}$=5 and shaking speed=240 rpm.

The adsorption results show that PNIPAM:Fe/MWCNTs used for the removal of kerosene from water enhanced the removal efficiency and adsorption capacity of MWCNTs from 45% and 2200 mg/g to 87% and 4300 mg/g, respectively. The parameters of the treatment process were as follows: V = 50 mL, $C_{kerosene}$ = 500 mg/L, contact time = 45 min, $T_{solution}$=20 °C, m_{ads}= 5.0 mg, $pH_{mixture}$=5 and shaking speed = 240 rpm.

PS:Fe/MWCNTs used for the removal of toluene from water enhanced the removal efficiency of MWCNTs from 19% and 240 mg/g to 62% and 769 mg/g, respectively. The optimum parameters of the treatment process were as follows:V=50 mL, $C_{toluene}$=50 mg/L, contact time=60 min, $T_{solution}$ = 35 °C, m_{ads} = 2.0 mg, $pH_{mixture}$=5 and shaking speed = 240 rpm.

The adsorption kinetics of kerosene and toluene followed a pseudo second-order kinetic model using PE:Fe/MWCNTs and PS:Fe/MWCNTs polymer composites. Moreover, the equilibrium adsorption study revealed that kerosene adsorption over PE:Fe/MWCNTs followed the Langmuir adsorption isotherm model, suggesting that adsorption was a uniform and homogeneous process. The Freundlich adsorption isotherm model fitted better with a high correlation coefficient when using PS:Fe/MWCNTs for the removal of toluene from water, suggesting the adsorption of toluene is a heterogeneous process and not the result of monolayer adsorption.

This study has proven that polymer-modified magnetic MWCNTs are highly promising adsorbents for the removal of hydrocarbons from contaminated water.

5. New scientific findings

The new scientific findings obtained during my PhD research in several theses are as follows:

5.1. V_2O_5 Nanoparticles for the removal of methylene blue from water

5.1.1. The nanostructure of prepared V_2O_5 was confirmed by FTIR, XRD, AFM and SEM studies. TG/DTA and FTIR analyses confirmed that the surface dehydroxylation and decomposition of the starting material NH_4VO_3 occurred at 250 °C, while thermal decomposition of NH_4VO_3 into V_2O_5 occurred between 293 and 355 °C [Appendix B. 1-2].

5.1.2. I affirmed by XRD data that the orthorhombic crystalline structure of V_2O_5 begins to form at an even lower temperature of 90 °C and a well-defined crystalline structure was observed at 750 °C. Heat treatment led to a significant increase in the crystallinity of samples, while it can cause a decrease in the surface area of the sample. The reduction in surface area for adsorption of the sample can explain the decrease in the sorption activity of the sample annealed at 750 °C with regard to the removal of methylene blue [Appendix B. 1-2].

5.1.3. The obtained results indicated that the vanadium samples heat treated at 90 and 750 °C have rather high adsorption capacities of between 15 and 27 mg/g in terms of MB removal from water when compared to other sorbents reported in the literature (qt between 15 and 19 mg/g). The optimum parameters concerning water contaminated by MB were as follows: annealing temperature of V_2O_5=500 °C, V = 30 mL, C=20 mg/L, Time=45min, $T_{solution}$=45°C, m_{ads}=60 mg, $pH_{solution}$=7 [Appendix B. 2].

5.1.4. I found that the best-fit kinetic and isotherm models with regard to the experimental results of methylene blue adsorption were the pseudo second-order and Freundlich equations with correlation coefficients R^2 of 0.9882 and 0.8929 respectively [Appendix B. 2].

5.2. Metal Oxide-Doped MWCNTs Nanocomposites for the Removal of Kerosene and Methylene Blue Dye from Water

5.2.1. I synthesised the novel adsorbents, namely metal oxide-doped MWCNTs nanoparticles, while preserving the crystalline phase and morphology of the graphene layers of carbon nanotubes (confirmed by BET, XRD, SEM, TEM). [Appendix B. 3].

5.2.2. I confirmed the successful doping of metal-oxide nanocomposites over MWCNTs surfaces using EDX and TGA analyses. The deposition of TiO_2 (5wt%), V_2O_5 (4-5 wt%) and CeO_2 (6-12 wt%) as well as V:Ti (~2wt%), V:Ce (8–10wt%) and V:Ce:Ti (6-7 wt%) oxides over the oxidized MWCNTs caused the blockage of some micropores. Meanwhile, the surface area available for adsorption treatment remained relatively high (115–135 m^2/g) [Appendix B. 3].

5.2.3. I found that the adsorption capacity (qt) and removal efficiency (RE) of MWCNTs with regard to the removal of kerosene and methylene blue from water increased after adding V_2O_5:CeO_2 over MWCNTs: $qt_{kerosene}$ increased from 3,355 to 4,271 mg/g and $RE_{kerosene}$ increased from 67 to 85% (V=50 mL, C=500 mg/L, Time = 60 min, $T_{solution}$=25 °C, m_{ads}=5 mg, $pH_{solusion}$ = 7); while qt_{MB} increased from 2.4 to 56.7 mg/g and RE_{MB} increased from 3 to 64% (V=20 mL, C=20 mg/L, Time = 25 min, $T_{solution}$=25 °C, m_{ads} =4.5 mg, $pH_{solusion}$=7) [Appendix B. 3].

5.2.4. I evaluated the kinetic data and the pseudo second-order kinetic model for the removal of kerosene from water with a correlation coefficient R_2 of 0.9994 was proposed. Furthermore, the intraparticle diffusion model showed the presence of the boundary layer effect, thereby confirming the significant contribution of the rate-limiting step towards the surface sorption of kerosene. The attachment of hydrocarbon molecules to adsorbent surfaces is likely to predominantly occur as a result of the formation of weak hydrogen bonds [Appendix B. 3].

5.3. Polymer-modified magnetite/MWCNTs for the removal of hydrocarbons from water

5.3.1. I designed new type of polymer (polyethylene (PE), polystyrene (PS), poly-n-isopropylacrylamide-co-butylacrylate (PNIPAM))-modified Fe/MWCNTs mesoporous materials for the removal of hydrocarbons from water. The presence

of magnetite components facilitated the facile separation of adsorbents from the mixture when subjected to an external magnetic field [Appendix B. 4, 5, 6].

5.3.2. I observed that the covalent functionalization via acids of MWCNTs followed by the deposition of iron oxide and non-covalent polymer modification preserved the crystalline structure of the carbon nanotubes. Furthermore, the surface area (S_{BET} =71-136 m^2/g) and pore structure (7.6-16.0 nm) of polymer-modified Fe/MWCNTs remain suitable for their application in wastewater purification processes [Appendix B. 4, 5, 6].

5.3.3. I proved using EDX analyses that iron oxide is attached to the surface of carbon nanotubes. The magnate crystalline structure of iron oxide was verified by XRD analysis. TG analyses confirmed that the polymer was successfully attached to the surface: 34 wt% PNIPAM: 55 wt% Fe/MWCNTs. The Raman spectroscopic studies confirmed the interaction between the carbon nanotubes, iron oxide and polymers. The calculated ID/IG ratio of the Raman peaks of MWCNTs, ox-MWCNTs, Fe/MWCNTs, PE:Fe/MWCNTs and PS:Fe/MWCNTs were 0.95, 1.08, 0.99, 0.87 and 0.89 respectively [Appendix B. 4, 5].

5.3.4. I concluded that the adsorption capacity and removal efficiency of the polymer-modified Fe/MWCNTs are higher than for MWCNTs:

- qt exp and RE for kerosene: MWCNTs (2092 mg/g and 42%) < Fe/MWCNTs (3154 mg/g and 63%) < PE:Fe/MWCNTs (3560 mg/g and 71%) under the following experimental conditions: C=200 mg/L, V=50 mL, $T_{solution}$ =25 °C, Time = 120 min, m = 2 mg, $pH_{solution}$ =7 [Appendix B. 4].

- qt exp and RE for kerosene: MWCNTs (2200 mg/g and 45%) < Fe/MWCNTs (3400 mg/g and 69%) < PNIPAM:Fe/MWCNTs (4400 mg/g and 87%) under the following experimental conditions for PNIPAM:Fe/MWCNTs: C = 500 mg/L, V = 50 mL, $T_{solution}$=25°C, Time=75 min, m=5 mg, $pH_{solution}$=7 [Appendix B. 6].

- qt exp and RE for toluene: MWCNTs (240 mg/g and 19%) < Fe/MWCNTs (450 mg/g and 36%) < PS:Fe/MWCNTs (769 mg/g and 62%) under the following experimental conditions:C = 50 mg/L, V =50 mL, $T_{solution}$=25 °C, Time=120 mins, m = 2 mg, $pH_{solution}$=7 [Appendix B. 5].

These results can be attributed to the fact that the hydrophobic/hydrophilic properties of MWCNTs are modified by preparing magnetite over MWCNTs followed by adding different types of polymers.

5.3.5. I observed that the experimental data of kerosene and toluene adsorption over PE:Fe/MWCNTs, PNIPAM:Fe/MWCNTs and PS:Fe/MWCNTs fitted well to the second-order kinetic model ($R^2 > 0.99$). In the case of kerosene adsorption over PE:Fe/MWCNTs, qe cal = 3,333 mg/g which is very close to the value measured experimentally of qt exp = 3,560 mg/g. In the case of toluene adsorption over PS:Fe/MWCNTs, qe cal = 1,111 mg/g, which is higher than the experimental value of qt exp = 769 mg/g [Appendix B. 4, 5, 6].

5.3.6. The equilibrium adsorption study concerning the removal of kerosene from water using polyethylene-modified Fe/MWCNTs showed that the Langmuir isotherm was obeyed and fitted with a high correlation coefficient, which suggests that the adsorption process is uniform and homogeneous. The Freundlich adsorption isotherm model fitted better when PS:Fe/MWCNTs were used to remove toluene from water, suggesting that the adsorption of toluene is heterogeneous and non-uniform [Appendix B. 4, 5, 6].

5.3.7. I proposed that the most probable mechanisms for the sorption of non-polar, alkane molecules on MWCNTs is via CH···π interactions. CH···π interactions are a type of weak non-covalent hydrogen bonds. In the case of fresh and polymer-modified MWCNTs, saturated hydrocarbons can be bonded to the surface of an adsorbent via a CH···π interaction between a hydrogen atom in kerosene and a carbon atom in MWCNTs and/or the polymer, namely PNIPAM or polyethylene. In addition, the adsorption of hydrocarbon molecules to the surface of the adsorbent could be due to intermolecular attractive forces (van der Waals forces) and ionic bonds (through stoichiometric charges of opposite signs) [Appendix B. 4, 6].

5.3.8. In the case of fresh MWCNTs, pi-pi interactions between the aromatic rings of CNTs and that of toluene occur. The carboxylic oxygen atoms of the acid-treated surface of MWCNTs and magnetite act as an electron donor, while the aromatic ring of toluene behaves as an electron acceptor in the formation of pi-pi interactions. It was found that the adsorption affinity of toluene by

PS:Fe/MWCNTs increases as a result of the formation of pi-pi interactions between the benzene rings of toluene and the polystyrene components of the adsorbent.

References

[1] S. Li *et al.*, "Magnetic multi-walled carbon nanotubes modified with polyaluminium chloride for removal of humic acid from aqueous solution," *Journal of Molecular Liquids*, vol. 279, pp. 241–250, 2019, doi: 10.1016/j.molliq.2019.01.016.

[2] Y. Z. Lin, L. bin Zhong, S. Dou, Z. D. Shao, Q. Liu, and Y. M. Zheng, "Facile synthesis of electrospun carbon nanofiber/graphene oxide composite aerogels for high efficiency oils absorption," *Environment International*, vol. 128, no. March, pp. 37–45, 2019, doi: 10.1016/j.envint.2019.04.019.

[3] B. Dubansky, A. Whitehead, J. T. Miller, C. D. Rice, and F. Galvez, "Multitissue molecular, genomic, and developmental effects of the deepwater horizon oil spill on resident Gulf killifish (Fundulus grandis)," *Environmental Science and Technology*, vol. 47, no. 10, pp. 5074–5082, 2013, doi: 10.1021/es400458p.

[4] M. Li, C. Bian, G. Yang, and X. Qiang, "Facile fabrication of water-based and non-fluorinated superhydrophobic sponge for efficient separation of immiscible oil/water mixture and water-in-oil emulsion," *Chemical Engineering Journal*, vol. 368, no. February, pp. 350–358, 2019, doi: 10.1016/j.cej.2019.02.176.

[5] X. Liang, S. Liu, S. Wang, Y. Guo, and S. Jiang, "Carbon-based sorbents: Carbon nanotubes," *Journal of Chromatography A*, vol. 1357, pp. 53–67, 2014, doi: 10.1016/j.chroma.2014.04.039.

[6] L. Zhao *et al.*, "Nanomaterials for treating emerging contaminants in water by adsorption and photocatalysis: Systematic review and bibliometric analysis," *Science of the Total Environment*, vol. 627, pp. 1253–1263, 2018, doi: 10.1016/j.scitotenv.2018.02.006.

[7] H. Anjum, K. Johari, N. Gnanasundaram, A. Appusamy, and M. Thanabalan, "Investigation of green functionalization of multiwall carbon nanotubes and its application in adsorption of benzene, toluene & p-xylene from aqueous solution," *Journal of Cleaner Production*, vol. 221, pp. 323–338, 2019, doi: 10.1016/j.jclepro.2019.02.233.

[8] D. A. Gopakumar, V. Arumughan, D. Pasquini, S. Y. Leu, H. P. S. Abdul Khalil, and S. Thomas, *Nanocellulose-Based Membranes for Water Purification*. Elsevier Inc., 2019. doi: 10.1016/B978-0-12-813926-4.00004-5.

[9] A. Tkaczyk, K. Mitrowska, and A. Posyniak, "Synthetic organic dyes as contaminants of the aquatic environment and their implications for ecosystems: A review," *Science of the Total Environment*, vol. 717. Elsevier B.V., May 15, 2020. doi: 10.1016/j.scitotenv.2020.137222.

[10] B. Wang, B. Gao, A. R. Zimmerman, and X. Lee, "Impregnation of multiwall carbon nanotubes in alginate beads dramatically enhances their adsorptive ability to aqueous methylene blue," *Chemical Engineering Research and Design*, vol. 133, pp. 235–242, May 2018, doi: 10.1016/j.cherd.2018.03.026.

[11] Z. Wang, M. Gao, X. Li, J. Ning, Z. Zhou, and G. Li, "Efficient adsorption of methylene blue from aqueous solution by graphene oxide modified persimmon tannins," *Materials Science and Engineering C*, vol. 108, Mar. 2020, doi: 10.1016/j.msec.2019.110196.

[12] M. Valcárcel, S. Cárdenas, B. M. Simonet, Y. Moliner-Martínez, and R. Lucena, "Carbon nanostructures as sorbent materials in analytical processes," *TrAC - Trends in Analytical Chemistry*, vol. 27, no. 1, pp. 34–43, 2008, doi: 10.1016/j.trac.2007.10.012.

[13] S. Mallakpour and E. Khadem, "Carbon nanotube–metal oxide nanocomposites: Fabrication, properties and applications," *Chemical Engineering Journal*, vol. 302, pp. 344–367, 2016, doi: 10.1016/j.cej.2016.05.038.

[14] H. Maleki, "Recent advances in aerogels for environmental remediation applications: A review," *Chemical Engineering Journal*, vol. 300, pp. 98–118, 2016, doi: 10.1016/j.cej.2016.04.098.

[15] R. K. Ibrahim *et al.*, "A clean approach for functionalized carbon nanotubes by deep eutectic solvents and their performance in the adsorption of methyl orange from aqueous solution," *Journal of Environmental Management*, vol. 235, no. February, pp. 521–534, 2019, doi: 10.1016/j.jenvman.2019.01.070.

[16] K. R. Parmar, D. T. K. Dora, K. K. Pant, and S. Roy, "An ultra-light flexible aerogel-based on methane derived CNTs as a reinforcing agent in silica-CMC matrix for efficient oil adsorption," *Journal of Hazardous Materials*, vol. 375, no. April, pp. 206–215, 2019, doi: 10.1016/j.jhazmat.2019.04.017.

[17] Y. H. Li *et al.*, "Competitive adsorption of Pb2+, Cu2+ and Cd 2+ ions from aqueous solutions by multiwalled carbon nanotubes," *Carbon N Y*, vol. 41, no. 14, pp. 2787–2792, 2003, doi: 10.1016/S0008-6223(03)00392-0.

[18] W. A. H. Altowayti, N. Othman, P. S. Goh, A. F. Alshalif, A. A. Al-Gheethi, and H. A. Algaifi, "Application of a novel nanocomposites carbon nanotubes functionalized with mesoporous silica-nitrenium ions (CNT-MS-N) in nitrate removal: Optimizations and nonlinear and linear regression

analysis," *Environmental Technology and Innovation*, vol. 22, May 2021, doi: 10.1016/j.eti.2021.101428.

[19] A. Yadav, P. Yadav, P. K. Labhasetwar, and V. K. Shahi, "CNT functionalized ZIF-8 impregnated poly(vinylidene fluoride-co-hexafluoropropylene) mixed matrix membranes for antibiotics removal from pharmaceutical industry wastewater by vacuum membrane distillation," *Journal of Environmental Chemical Engineering*, vol. 9, no. 6, Dec. 2021, doi: 10.1016/j.jece.2021.106560.

[20] X. Hu, C. Zou, and X. Zou, "The formation of supramolecular carbon nanofiber via amidation reaction on the surface of amino single walled carbon nanotubes for selective adsorption organic pollutants," *Journal of Colloid and Interface Science*, vol. 542, pp. 112–122, 2019, doi: 10.1016/j.jcis.2019.01.130.

[21] Y. Wu *et al.*, "Three-dimensional A-Fe2O3/amino-functionalization carbon nanotube sponge for adsorption and oxidative removal of tetrabromobisphenol A," *Separation and Purification Technology*, vol. 211, no. June 2018, pp. 359–367, 2019, doi: 10.1016/j.seppur.2018.10.002.

[22] E. A. Abdelrahman, R. M. Hegazey, and R. E. El-Azabawy, "Efficient removal of methylene blue dye from aqueous media using Fe/Si, Cr/Si, Ni/Si, and Zn/Si amorphous novel adsorbents," *Journal of Materials Research and Technology*, vol. 8, no. 6, pp. 5301–5313, 2019, doi: 10.1016/j.jmrt.2019.08.051.

[23] S. K. Jayaraj, V. Sadishkumar, T. Arun, and P. Thangadurai, "Enhanced photocatalytic activity of V2O5 nanorods for the photodegradation of organic dyes: A detailed understanding of the mechanism and their antibacterial activity," *Materials Science in Semiconductor Processing*, vol. 85, pp. 122–133, Oct. 2018, doi: 10.1016/j.mssp.2018.06.006.

[24] C. Anushree and J. Philip, "Efficient removal of methylene blue dye using cellulose capped Fe 3 O 4 nanofluids prepared using oxidation-precipitation method," *Colloids and Surfaces A: Physicochemical and Engineering Aspects*, vol. 567, no. January, pp. 193–204, 2019, doi: 10.1016/j.colsurfa.2019.01.057.

[25] A. Dawood Salman, J. Tatjána, M. A. Al-Mayyahi, R. I. Ibrahim, T. Adnan Abdullah, and E. H. Khader, "Improvement of mechanical properties of Oil well cement by incorporate Nano-CaCO3 prepared from eggshell waste," *IOP Conference Series: Materials Science and Engineering*, vol. 765, no. 1, 2020, doi: 10.1088/1757-899X/765/1/012006.

[26] L. Kong, Z. Diao, X. Chang, Y. Xiong, and D. Chen, "Synthesis of recoverable and reusable granular MgO-SCCA-Zn hybrid ozonation catalyst for degradation of methylene blue," *Journal of Environmental Chemical Engineering*, vol. 4, no. 4, pp. 4385–4391, 2016, doi: 10.1016/j.jece.2016.10.002.

[27] A. Mishra *et al.*, "Rapid photodegradation of methylene blue dye by rGO- V2O5 nano composite," *Journal of Alloys and Compounds*, vol. 842, Nov. 2020, doi: 10.1016/j.jallcom.2020.155746.

[28] R. Rasheed, H. Salah, R. Al-Shaikhly, T. Abdullah, A. Salman, and T. Yuzakova, *Synthesis and catalytic activity studies of α-MnO2 nanorodes, rutile TiO2 and its composite prepared by hydrothermal method*, vol. 2213. 2020. doi: 10.1063/5.0000228.

[29] N. Al-Jammal *et al.*, "Functionalized carbon nanotubes for hydrocarbon removal from water," *Journal of Environmental Chemical Engineering*, vol. 8, no. 2, p. 103570, 2020, doi: 10.1016/j.jece.2019.103570.

[30] E. Santoso, R. Ediati, Y. Kusumawati, H. Bahruji, D. O. Sulistiono, and D. Prasetyoko, "Review on recent advances of carbon based adsorbent for methylene blue removal from waste water," *Materials Today Chemistry*, vol. 16, p. 100233, 2020, doi: 10.1016/j.mtchem.2019.100233.

[31] S. Bolisetty and R. Mezzenga, "Amyloid-carbon hybrid membranes for universal water purification," *Nature Nanotechnology*, vol. 11, no. 4, pp. 365–371, 2016, doi: 10.1038/nnano.2015.310.

[32] S. F. Soares, M. I. Rodrigues, T. Trindade, and A. L. Daniel-da-Silva, "Chitosan-silica hybrid nanosorbents for oil removal from water," *Colloids and Surfaces A: Physicochemical and Engineering Aspects*, vol. 532, pp. 305–313, 2017, doi: 10.1016/j.colsurfa.2017.04.076.

[33] M. Sharma *et al.*, "ZnO tetrapods and activated carbon based hybrid composite: Adsorbents for enhanced decontamination of hexavalent chromium from aqueous solution," *Chemical Engineering Journal*, vol. 358, pp. 540–551, 2019, doi: 10.1016/j.cej.2018.10.031.

[34] M. E. A. El-sayed, "Nanoadsorbents for water and wastewater remediation," *Science of the Total Environment*, vol. 739, p. 139903, 2020, doi: 10.1016/j.scitotenv.2020.139903.

[35] I. Ali *et al.*, "Preparation and characterization of SnO2-CeO2 nanocomposites: Sorption, modeling and kinetics for azorubine dye removal in water," *Journal of Molecular Liquids*, 2021, doi: 10.1016/j.molliq.2021.117119.

[36] D. Ewis, A. Benamor, M. M. Ba-Abbad, M. Nasser, M. El-Naas, and H. Qiblawey, "Removal of Oil Content from Oil-Water Emulsions Using Iron Oxide/Bentonite Nano Adsorbents," *Journal of Water Process Engineering*, vol. 38, Dec. 2020, doi: 10.1016/j.jwpe.2020.101583.

[37] A. T. Hoang, S. Nižetić, X. Q. Duong, L. Rowinski, and X. P. Nguyen, "Advanced super-hydrophobic polymer-based porous absorbents for the treatment of oil-polluted water," *Chemosphere*, vol. 277. Elsevier Ltd, Aug. 01, 2021. doi: 10.1016/j.chemosphere.2021.130274.

[38] N. Tavker, U. Gaur, and M. Sharma, "Cellulose supported bismuth vanadate nanocomposite for effective removal of organic pollutant," *Journal of Environmental Chemical Engineering*, vol. 8, no. 4, Aug. 2020, doi: 10.1016/j.jece.2020.104027.

[39] H. Neelamegan, D. K. Yang, G. J. Lee, S. Anandan, and J. J. Wu, "Synthesis of magnetite nanoparticles anchored cellulose and lignin-based carbon nanotube composites for rapid oil spill cleanup," *Materials Today Communications*, vol. 22, no. June 2019, p. 100746, 2020, doi: 10.1016/j.mtcomm.2019.100746.

[40] D. A. Pethsangave, P. H. Wadekar, R. v. Khose, and S. Some, "Super-hydrophobic carrageenan cross-linked graphene sponge for recovery of oil and organic solvent from their water mixtures," *Polymer Testing*, vol. 90, no. July, p. 106743, 2020, doi: 10.1016/j.polymertesting.2020.106743.

[41] J. Duan, W. Liu, X. Zhao, Y. Han, S. E. O'Reilly, and D. Zhao, "Study of residual oil in Bay Jimmy sediment 5 years after the Deepwater Horizon oil spill: Persistence of sediment retained oil hydrocarbons and effect of dispersants on desorption," *Science of the Total Environment*, vol. 618, pp. 1244–1253, 2018, doi: 10.1016/j.scitotenv.2017.09.234.

[42] H. Singh, N. Bhardwaj, S. K. Arya, and M. Khatri, "Environmental impacts of oil spills and their remediation by magnetic nanomaterials," *Environmental Nanotechnology, Monitoring and Management*, vol. 14, no. November 2019, p. 100305, 2020, doi: 10.1016/j.enmm.2020.100305.

[43] "ITOPF Limited, 2019. Oil tanker spill statistics 2018. London," *ITOPF*, 2019.

[44] V. Bebarta and C. DeWitt, "Miscellaneous hydrocarbon solvents," *Clinics in Occupational and Environmental Medicine*, vol. 4, no. 3, pp. 455–479, 2004, doi: 10.1016/j.coem.2004.03.004.

[45] D. Borah and R. N. S. Yadav, "Bioremediation of petroleum based contaminants with biosurfactant produced by a newly isolated petroleum oil degrading bacterial strain," *Egyptian Journal of Petroleum*, vol. 26, no. 1, pp. 181–188, 2017, doi: 10.1016/j.ejpe.2016.02.005.

[46] P. Saharan, G. R. Chaudhary, S. K. Mehta, and A. Umar, "Removal of water contaminants by iron oxide nanomaterials," *Journal of Nanoscience and Nanotechnology*, vol. 14, no. 1, pp. 627–643, 2014, doi: 10.1166/jnn.2014.9053.

[47] J. Huang, H. Liu, S. Chen, and C. Ding, "Hierarchical porous MWCNTs-silica aerogel synthesis for high-efficiency oily water treatment," *Journal of Environmental Chemical Engineering*, vol. 4, no. 3, pp. 3274–3282, 2016, doi: 10.1016/j.jece.2016.06.039.

[48] O. Saber, N. H. Mohamed, and A. A. Al Jaafari, "Synthesis of Magnetic Nanoparticles and Nanosheets for Oil Spill Removal," *Nanoscience &Nanotechnology-Asia*, vol. 5, no. 1, pp. 32–43, 2015, doi: 10.2174/2210681205666150601215445.

[49] J. Fu *et al.*, "Adsorption of methylene blue by a high-efficiency adsorbent (polydopamine microspheres): Kinetics, isotherm, thermodynamics and mechanism analysis," *Chemical Engineering Journal*, vol. 259, pp. 53–61, 2015, doi: 10.1016/j.cej.2014.07.101.

[50] A. Gagrani, J. Zhou, and T. Tsuzuki, "Solvent free mechanochemical synthesis of MnO2 for the efficient degradation of Rhodamine-B," *Ceramics International*, vol. 44, no. 5, pp. 4694–4698, 2018, doi: 10.1016/j.ceramint.2017.12.050.

[51] H. Shayesteh, A. Ashrafi, and A. Rahbar-Kelishami, "Evaluation of Fe3O4@MnO2 core-shell magnetic nanoparticles as an adsorbent for decolorization of methylene blue dye in contaminated water: Synthesis and characterization, kinetic, equilibrium, and thermodynamic studies," *Journal of Molecular Structure*, vol. 1149, pp. 199–205, 2017, doi: 10.1016/j.molstruc.2017.07.100.

[52] S. I. Siddiqui, O. Manzoor, M. Mohsin, and S. A. Chaudhry, "Nigella sativa seed based nanocomposite-MnO2/BC: An antibacterial material for photocatalytic degradation, and adsorptive removal of Methylene blue from water," *Environmental Research*, vol. 171, no. September 2018, pp. 328–340, 2019, doi: 10.1016/j.envres.2018.11.044.

[53] S. I. Siddiqui, G. Rathi, and S. A. Chaudhry, "Acid washed black cumin seed powder preparation for adsorption of methylene blue dye from aqueous solution: Thermodynamic, kinetic and isotherm studies," *Journal of Molecular Liquids*, vol. 264, pp. 275–284, 2018, doi: 10.1016/j.molliq.2018.05.065.

[54] A. H. Jawad, R. A. Rashid, R. M. A. Mahmuod, M. A. M. Ishak, N. N. Kasim, and K. Ismail, "Adsorption of methylene blue onto coconut (Cocos nucifera) leaf: optimization, isotherm and kinetic studies," *Desalination and Water Treatment*, vol. 57, no. 19, pp. 8839–8853, 2016, doi: 10.1080/19443994.2015.1026282.

[55] W. A. Khanday, M. Asif, and B. H. Hameed, “Cross-linked beads of activated oil palm ash zeolite/chitosan composite as a bio-adsorbent for the removal of methylene blue and acid blue 29 dyes,” *International Journal of Biological Macromolecules*, vol. 95, pp. 895–902, 2017, doi: 10.1016/j.ijbiomac.2016.10.075.

[56] Y. He, D. bin Jiang, J. Chen, D. Y. Jiang, and Y. X. Zhang, “Synthesis of MnO2 nanosheets on montmorillonite for oxidative degradation and adsorption of methylene blue,” *Journal of Colloid and Interface Science*, vol. 510, pp. 207–220, 2018, doi: 10.1016/j.jcis.2017.09.066.

[57] X. S. Hu, R. Liang, and G. Sun, “Super-adsorbent hydrogel for removal of methylene blue dye from aqueous solution,” *Journal of Materials Chemistry A*, vol. 6, no. 36, pp. 17612–17624, 2018, doi: 10.1039/c8ta04722g.

[58] K. L. Tan and B. H. Hameed, “Insight into the adsorption kinetics models for the removal of contaminants from aqueous solutions,” vol. 0, pp. 1–24, 2017, doi: 10.1016/j.jtice.2017.01.024.

[59] A. M. Tayeb, R. Farouq, O. A. Mohamed, and M. A. Tony, “Oil spill clean-up using combined sorbents: a comparative investigation and design aspects,” *International Journal of Environmental Analytical Chemistry*, vol. 100, no. 3, pp. 311–323, 2020, doi: 10.1080/03067319.2019.1636976.

[60] F. Zareei Pour, M. M. Sabzehmeidani, H. Karimi, V. Madadi Avargani, and M. Ghaedi, “Superhydrophobic–superoleophilic electrospun nanofibrous membrane modified by the chemical vapor deposition of dimethyl dichlorosilane for efficient oil–water separation,” *Journal of Applied Polymer Science*, vol. 136, no. 24, pp. 1–11, 2019, doi: 10.1002/app.47621.

[61] Y. Wei, H. Qi, X. Gong, and S. Zhao, “Specially Wettable Membranes for Oil–Water Separation,” *Advanced Materials Interfaces*, vol. 5, no. 23, pp. 1–27, 2018, doi: 10.1002/admi.201800576.

[62] T. Mohammadi, M. Kazemimoghadam, and M. Saadabadi, “Modeling of membrane fouling and flux decline in reverse osmosis during separation of oil in water emulsions,” *Desalination*, vol. 157, no. 1–3, pp. 369–375, 2003, doi: 10.1016/S0011-9164(03)00419-3.

[63] D. Kukkar *et al.*, “Recent advances in carbon nanotube sponge–based sorption technologies for mitigation of marine oil spills,” *Journal of Colloid and Interface Science*, vol. 570, pp. 411–422, 2020, doi: 10.1016/j.jcis.2020.03.006.

[64] A. Kamgar and S. Hassanajili, “Super-hydrophobic Fe3O4@SiO2@MPS nanoparticles for oil remediation: The influence of pH and concentration on clustering phenomenon and oil sorption,” *Journal of Molecular Liquids*, vol. 315, p. 113709, 2020, doi: 10.1016/j.molliq.2020.113709.

[65] H. Ghasemzadeh, M. Dargahi, G. Eyvazi, and B. V. Farahani, “Nanomagnetic Organogel Based on Dodecyl Methacrylate for Absorption and Removal of Organic Solvents,” *Chinese Journal of Polymer Science (English Edition)*, vol. 37, no. 5, pp. 444–450, 2019, doi: 10.1007/s10118-019-2213-4.

[66] F. D. Marques, F. G. Souza, and G. E. Oliveira, “Oil sorbers based on renewable sources and coffee grounds,” *Journal of Applied Polymer Science*, vol. 133, no. 11, pp. 1–7, 2016, doi: 10.1002/app.43127.

[67] L. Wu, J. Zhang, B. Li, and A. Wang, “Mechanical- and oil-durable superhydrophobic polyester materials for selective oil absorption and oil/water separation,” *Journal of Colloid and Interface Science*, vol. 413, pp. 112–117, 2014, doi: 10.1016/j.jcis.2013.09.028.

[68] A. Middea *et al.*, “Magnetic polystyrene–palygorskite nanocomposite obtained by heterogeneous phase polymerization to apply in the treatment of oily waters,” *Journal of Applied Polymer Science*, vol. 135, no. 15, pp. 2–9, 2018, doi: 10.1002/app.46162.

[69] J. O. Nwadiogbu, V. I. E. Ajiwe, and P. A. C. Okoye, “Removal of crude oil from aqueous medium by sorption on hydrophobic corncobs: Equilibrium and kinetic studies,” *Journal of Taibah University for Science*, vol. 10, no. 1, pp. 56–63, 2016, doi: 10.1016/j.jtusci.2015.03.014.

[70] A. T. Hoang, V. V. Le, A. R. M. S. Al-Tawaha, D. N. Nguyen, M. M. Noor, and V. V. Pham, “An absorption capacity investigation of new absorbent based on polyurethane foams and rice straw for oil spill cleanup,” *Petroleum Science and Technology*, vol. 36, no. 5, pp. 361–370, 2018, doi: 10.1080/10916466.2018.1425722.

[71] S. Hashemian, M. Rahimi, and A. A. Kerdegari, “CuFe2O4@graphene nanocomposite as a sorbent for removal of alizarine yellow azo dye from aqueous solutions,” *Desalination and Water Treatment*, vol. 57, no. 31, pp. 14696–14707, 2016, doi: 10.1080/19443994.2015.1065766.

[72] O. Ghasemi, N. Mehrdadi, M. Baghdadi, B. Aminzadeh, and A. Ghaseminejad, “Spilled oil absorption from Caspian sea water by graphene/chitosan nano composite,” *Energy Sources, Part A: Recovery, Utilization and Environmental Effects*, vol. 42, no. 23, pp. 2856–2872, 2020, doi: 10.1080/15567036.2019.1618995.

[73] N. A. Abdelwahab and F. M. Helaly, “Preparation and characterization of porous acrylate terpolymer nanocomposite for removal of diesel oil from artificial seawater,” *Separation Science*

and Technology (Philadelphia), vol. 52, no. 9, pp. 1624–1634, 2017, doi: 10.1080/01496395.2017.1295992.

[74] Z. Ayazi, M. Pourvali, and A. A. Matin, "Preparation of a novel stir bar coating based on montmorillonite doped polypyrrole/nylon-6 nanocomposite for sorptive extraction of organophosphorous pesticides in aqueous samples," *International Journal of Environmental Analytical Chemistry*, vol. 98, no. 2, pp. 138–155, 2018, doi: 10.1080/03067319.2018.1438421.

[75] A. P. Periasamy, W. P. Wu, R. Ravindranath, P. Roy, G. L. Lin, and H. T. Chang, "Polymer/reduced graphene oxide functionalized sponges as superabsorbents for oil removal and recovery," *Marine Pollution Bulletin*, vol. 114, no. 2, pp. 888–895, 2017, doi: 10.1016/j.marpolbul.2016.11.005.

[76] D. Feldman, "Lignin nanocomposites," *Journal of Macromolecular Science, Part A: Pure and Applied Chemistry*, vol. 53, no. 6, pp. 382–387, 2016, doi: 10.1080/10601325.2016.1166006.

[77] Y. Si *et al.*, "Superelastic and Superhydrophobic Nanofiber-Assembled Cellular Aerogels for Effective Separation of Oil/Water Emulsions," *ACS Nano*, vol. 9, no. 4, pp. 3791–3799, 2015, doi: 10.1021/nn506633b.

[78] S. Samadi, S. S. Yazd, H. Abdoli, P. Jafari, and M. Aliabadi, "Fabrication of novel chitosan/PAN/magnetic ZSM-5 zeolite coated sponges for absorption of oil from water surfaces," *International Journal of Biological Macromolecules*, vol. 105, pp. 370–376, 2017, doi: 10.1016/j.ijbiomac.2017.07.050.

[79] M. Y. Koroleva, S. A. Shirokikh, L. K. Khasanova, E. S. Babusenko, and E. v. Yurtov, "Highly porous polymeric sponges for oil sorption," *Mendeleev Communications*, vol. 29, no. 2, pp. 176–177, 2019, doi: 10.1016/j.mencom.2019.03.020.

[80] Z. Luo *et al.*, "Photothermal hierarchical carbon nanotube/reduced graphene oxide microspherical aerogels with radially orientated microchannels for efficient cleanup of crude oil spills," *Journal of Colloid and Interface Science*, vol. 570, pp. 61–71, 2020, doi: 10.1016/j.jcis.2020.02.097.

[81] P. Madhusudhana Reddy, C. J. Chang, J. K. Chen, M. T. Wu, and C. F. Wang, "Robust polymer grafted Fe 3 O 4 nanospheres for benign removal of oil from water," *Applied Surface Science*, vol. 368, pp. 27–35, 2016, doi: 10.1016/j.apsusc.2016.01.250.

[82] Y. Zhan *et al.*, *Robust super-hydrophobic/super-oleophilic sandwich-like UIO-66-F4@rGO composites for efficient and multitasking oil/water separation applications*, vol. 388. Elsevier B.V., 2020. doi: 10.1016/j.jhazmat.2019.121752.

[83] A. W. Ritchie, H. J. Cox, S. N. Barrientos-Palomo, G. J. Sharples, and J. P. S. Badyal, "Bioinspired multifunctional polymer–nanoparticle–surfactant complex nanocomposite surfaces for antibacterial oil–water separation," *Colloids and Surfaces A: Physicochemical and Engineering Aspects*, vol. 560, no. August 2018, pp. 352–359, 2019, doi: 10.1016/j.colsurfa.2018.10.030.

[84] Q. Wang, Y. Zhang, T. Hu, and C. Meng, "Fe3O4 nanoparticles/polymer immobilized on silicate platelets for crude oil recovery," *Microporous and Mesoporous Materials*, vol. 278, pp. 185–194, 2019, doi: 10.1016/j.micromeso.2018.11.033.

[85] Z. Sarwar *et al.*, "Fibrous PEBA-graphene nanocomposite filaments and membranes fabricated by extrusion and additive manufacturing," *European Polymer Journal*, vol. 121, p. 109317, 2019, doi: 10.1016/j.eurpolymj.2019.109317.

[86] P. P. Dorneanu, C. Cojocaru, N. Olaru, P. Samoila, A. Airinei, and L. Sacarescu, "Electrospun PVDF fibers and a novel PVDF/CoFe 2 O 4 fibrous composite as nanostructured sorbent materials for oil spill cleanup," *Applied Surface Science*, vol. 424, pp. 389–396, 2017, doi: 10.1016/j.apsusc.2017.01.177.

[87] V. K. Gupta and Suhas, "Application of low-cost adsorbents for dye removal - A review," *Journal of Environmental Management*, vol. 90, no. 8, pp. 2313–2342, 2009, doi: 10.1016/j.jenvman.2008.11.017.

[88] S. M. Ghoreishi and R. Haghighi, "Chemical catalytic reaction and biological oxidation for treatment of non-biodegradable textile effluent," *Chemical Engineering Journal*, vol. 95, no. 1–3, pp. 163–169, 2003, doi: 10.1016/S1385-8947(03)00100-1.

[89] M. Rafatullah, O. Sulaiman, R. Hashim, and A. Ahmad, "Adsorption of methylene blue on low-cost adsorbents: A review," *Journal of Hazardous Materials*, vol. 177, no. 1–3, pp. 70–80, 2010, doi: 10.1016/j.jhazmat.2009.12.047.

[90] E. I. Unuabonah, G. U. Adie, L. O. Onah, and O. G. Adeyemi, "Multistage optimization of the adsorption of methylene blue dye onto defatted Carica papaya seeds," *Chemical Engineering Journal*, vol. 155, no. 3, pp. 567–579, 2009, doi: 10.1016/j.cej.2009.07.012.

[91] M. A. Rauf, I. Shehadeh, A. Ahmed, and A. Al-zamly, "Removal of Methylene Blue Dye from Aqueous Solution by Using Cestrum nocturnum Leaves, as a Low Cost Adsorbent," *Journal of Chemical, Biological and Physical Sciences*, vol. 7, no. 3, pp. 608–613, 2017, doi: 10.24214/jcbps.d.7.3.51225.

[92] B. Shi, G. Li, D. Wang, C. Feng, and H. Tang, “Removal of direct dyes by coagulation: The performance of preformed polymeric aluminum species,” *Journal of Hazardous Materials*, vol. 143, no. 1–2, pp. 567–574, 2007, doi: 10.1016/j.jhazmat.2006.09.076.
[93] Y. Zhou, Z. Liang, and Y. Wang, “Decolorization and COD removal of secondary yeast wastewater effluents by coagulation using aluminum sulfate,” *Desalination*, vol. 225, no. 1–3, pp. 301–311, 2008, doi: 10.1016/j.desal.2007.07.010.
[94] A. Mishra and M. Bajpai, “The flocculation performance of Tamarindus mucilage in relation to removal of vat and direct dyes,” *Bioresource Technology*, vol. 97, no. 8, pp. 1055–1059, 2006, doi: 10.1016/j.biortech.2005.04.049.
[95] J. W. Lee, S. P. Choi, R. Thiruvenkatachari, W. G. Shim, and H. Moon, “Evaluation of the performance of adsorption and coagulation processes for the maximum removal of reactive dyes,” *Dyes and Pigments*, vol. 69, no. 3, pp. 196–203, 2006, doi: 10.1016/j.dyepig.2005.03.008.
[96] K. G. Bhattacharyya and A. Sharma, “Adsorption of Pb(II) from aqueous solution by Azadirachta indica (Neem) leaf powder,” *Journal of Hazardous Materials*, vol. 113, no. 1–3, pp. 97–109, 2004, doi: 10.1016/j.jhazmat.2004.05.034.
[97] G. Crini, “Non-conventional low-cost adsorbents for dye removal: A review,” *Bioresource Technology*, vol. 97, no. 9, pp. 1061–1085, 2006, doi: 10.1016/j.biortech.2005.05.001.
[98] B. Koumanova and S. J. Allen, “Decolourisation of Water / Wastewater Using Adsorption (Review),” *Journal of the University of Chemical Technology and Metallurgy*, vol. 40, pp. 175–192, 2005.
[99] M. T. Yagub, T. K. Sen, S. Afroze, and H. M. Ang, “NU SC,” *Advances in Colloid and Interface Science*, 2014, doi: 10.1016/j.cis.2014.04.002.
[100] A. Sengupta and N. K. Gupta, “MWCNTs BASED SORBENTS FOR NUCLEAR WASTE MANAGEMENT: A REVIEW,” *Biochemical Pharmacology*, 2017, doi: 10.1016/j.jece.2017.09.054.
[101] C. Santhosh, V. Velmurugan, G. Jacob, S. K. Jeong, A. N. Grace, and A. Bhatnagar, “Role of nanomaterials in water treatment applications: A review,” *Chemical Engineering Journal*, vol. 306, pp. 1116–1137, 2016, doi: 10.1016/j.cej.2016.08.053.
[102] H. Sadegh *et al.*, “The role of nanomaterials as effective adsorbents and their applications in wastewater treatment,” *Journal of Nanostructure in Chemistry*, vol. 7, no. 1, pp. 1–14, 2017, doi: 10.1007/s40097-017-0219-4.
[103] Z. Cai, Y. Sun, W. Liu, F. Pan, P. Sun, and J. Fu, “An overview of nanomaterials applied for removing dyes from wastewater,” 2017, doi: 10.1007/s11356-017-9003-8.
[104] G. Z. Kyzas and K. A. Matis, “Nanoadsorbents for pollutants removal: A review,” *Journal of Molecular Liquids*, vol. 203, pp. 159–168, 2015, doi: 10.1016/j.molliq.2015.01.004.
[105] F. Lu and D. Astruc, “Nanomaterials for removal of toxic elements from water,” *Coordination Chemistry Reviews*, vol. 356, pp. 147–164, 2018, doi: 10.1016/j.ccr.2017.11.003.
[106] D. A. Richards, A. Maruani, and V. Chudasama, “Antibody fragments as nanoparticle targeting ligands: a step in the right direction,” *Chemical Science*, vol. 8, no. 1, pp. 63–77, 2016, doi: 10.1039/c6sc02403c.
[107] R. Ladj *et al.*, “Individual inorganic nanoparticles: Preparation, functionalization and in vitro biomedical diagnostic applications,” *Journal of Materials Chemistry B*, vol. 1, no. 10, pp. 1381–1396, 2013, doi: 10.1039/c2tb00301e.
[108] J. P. Rao and K. E. Geckeler, “Polymer nanoparticles: Preparation techniques and size-control parameters,” *Progress in Polymer Science (Oxford)*, vol. 36, no. 7, pp. 887–913, 2011, doi: 10.1016/j.progpolymsci.2011.01.001.
[109] R. TIRUWA, “A review on nanoparticles – preparation and evaluation parameters,” *Indian Journal of Pharmaceutical and Biological Research*, vol. 4, no. 2, pp. 27–31, 2016, doi: 10.30750/ijpbr.4.2.4.
[110] A. Akbarzadeh, R. Rezaei-sadabady, S. Davaran, S. W. Joo, and N. Zarghami, “Liposome : classification , prepNew aspects of liposomesaration , and applications,” *Nanoscale Research Letters*, vol. 8, no. 102, pp. 1–9, 2013, [Online]. Available: http://www.nanoscalereslett.com/content/8/1/102
[111] J. U. A. H. Junghanns and R. H. Müller, “Nanocrystal technology, drug delivery and clinical applications,” *International Journal of Nanomedicine*, vol. 3, no. 3, pp. 295–309, 2008, doi: 10.2147/IJN.S595.
[112] A. Malik, S. Chaudhary, G. Garg, and A. Tomar, “Dendrimers : A Tool for Drug Delivery,” *Advances in Biological Research*, vol. 6, no. 4, pp. 165–169, 2012, doi: 10.5829/idosi.abr.2012.6.4.6254.

[113] M. N. Zafar, Q. Dar, F. Nawaz, M. N. Zafar, M. Iqbal, and M. F. Nazar, "Effective adsorptive removal of azo dyes over spherical ZnO nanoparticles," *Journal of Materials Research and Technology*, vol. 8, no. 1, pp. 713–725, Jan. 2019, doi: 10.1016/j.jmrt.2018.06.002.
[114] M. N. Zafar, Q. Dar, F. Nawaz, M. N. Zafar, M. Iqbal, and M. F. Nazar, "Effective adsorptive removal of azo dyes over spherical ZnO nanoparticles," *Journal of Materials Research and Technology*, vol. 8, no. 1, pp. 713–725, 2019, doi: 10.1016/j.jmrt.2018.06.002.
[115] S. Iijima, "Growth of carbon nanotubes," 1993.
[116] "The smallest carbon nanotube Related papers," 2000. [Online]. Available: www.nature.com
[117] V. N. Popov, "Carbon nanotubes: Properties and application," *Materials Science and Engineering R: Reports*, vol. 43, no. 3, pp. 61–102, 2004, doi: 10.1016/j.mser.2003.10.001.
[118] C. Backes and A. Hirsch, "Noncovalent Functionalization of Carbon Nanotubes," in *Chemistry of Nanocarbons*, Chichester, UK: John Wiley & Sons, Ltd, 2010, pp. 1–48. doi: 10.1002/9780470660188.ch1.
[119] M. Endo and H. W. Kroto, "Formation of carbon nanofibers," *Journal of Physical Chemistry*, vol. 96, no. 17, pp. 6941–6944, 1992, doi: 10.1021/j100196a017.
[120] A. Oberlin, M. Endo, and T. Koyama, "Filamentous growth of carbon through benzene decomposition," *Journal of Crystal Growth*, vol. 32, no. 3, pp. 335–349, 1976, doi: 10.1016/0022-0248(76)90115-9.
[121] D. A. Britz and A. N. Khlobystov, "Noncovalent interactions of molecules with single walled carbon nanotubes," *Chemical Society Reviews*, vol. 35, no. 7, pp. 637–659, 2006, doi: 10.1039/b507451g.
[122] P. Avouris, "Molecular electronics with carbon nanotubes," *Accounts of Chemical Research*, vol. 35, no. 12, pp. 1026–1034, 2002, doi: 10.1021/ar010152e.
[123] G. P. Rao, C. Lu, and F. Su, "Sorption of divalent metal ions from aqueous solution by carbon nanotubes: A review," *Separation and Purification Technology*, vol. 58, no. 1, pp. 224–231, 2007, doi: 10.1016/j.seppur.2006.12.006.
[124] B. Pan and B. Xing, "Adsorption mechanisms of organic chemicals on carbon nanotubes," *Environmental Science and Technology*, vol. 42, no. 24. pp. 9005–9013, Dec. 15, 2008. doi: 10.1021/es801777n.
[125] P. Kondratyuk and J. T. Yates, "Molecular views of physical adsorption inside and outside of single-wall carbon nanotubes," *Accounts of Chemical Research*, vol. 40, no. 10, pp. 995–1004, 2007, doi: 10.1021/ar700013c.
[126] C. Chen, J. Hu, D. Shao, J. Li, and X. Wang, "Adsorption behavior of multiwall carbon nanotube/iron oxide magnetic composites for Ni(II) and Sr(II)," *Journal of Hazardous Materials*, vol. 164, no. 2–3, pp. 923–928, May 2009, doi: 10.1016/j.jhazmat.2008.08.089.
[127] Z.-C. Di, Y.-H. Li, Z.-K. Luan, and J. Liang, "Adsorption of Chromium(VI) Ions from Water by Carbon Nanotubes."
[128] X. Tan, M. Fang, C. Chen, S. Yu, and X. Wang, "Counterion effects of nickel and sodium dodecylbenzene sulfonate adsorption to multiwalled carbon nanotubes in aqueous solution," *Carbon N Y*, vol. 46, no. 13, pp. 1741–1750, Nov. 2008, doi: 10.1016/j.carbon.2008.07.023.
[129] C. H. Chen and C. C. Huang, "Hydrogen adsorption in defective carbon nanotubes," *Separation and Purification Technology*, vol. 65, no. 3, pp. 305–310, Mar. 2009, doi: 10.1016/j.seppur.2008.10.048.
[130] Y. H. Li *et al.*, "Competitive adsorption of Pb2+, Cu2+ and Cd 2+ ions from aqueous solutions by multiwalled carbon nanotubes," in *Carbon*, 2003, vol. 41, no. 14, pp. 2787–2792. doi: 10.1016/S0008-6223(03)00392-0.
[131] C. Chen and X. Wang, "Adsorption of Ni(II) from aqueous solution using Oxidized multiwall carbon nanotubes," *Industrial and Engineering Chemistry Research*, vol. 45, no. 26, pp. 9144–9149, Dec. 2006, doi: 10.1021/ie060791z.
[132] C. Chen and X. Wang, "Adsorption of Ni(II) from aqueous solution using Oxidized multiwall carbon nanotubes," *Industrial and Engineering Chemistry Research*, vol. 45, no. 26, pp. 9144–9149, 2006, doi: 10.1021/ie060791z.
[133] J. Goering, E. Kadossov, and U. Burghaus, "Adsorption kinetics of alcohols on single-wall carbon nanotubes: An ultrahigh vacuum surface chemistry study," *Journal of Physical Chemistry C*, vol. 112, no. 27, pp. 10114–10124, 2008, doi: 10.1021/jp801686u.
[134] H. Hyung and J. H. Kim, "Natural organic matter (NOM) adsorption to multi-walled carbon nanotubes: Effect of NOM characteristics and water quality parameters," *Environmental Science and Technology*, vol. 42, no. 12, pp. 4416–4421, 2008, doi: 10.1021/es702916h.
[135] N. M. Mubarak, J. N. Sahu, E. C. Abdullah, and N. S. Jayakumar, "Rapid adsorption of toxic Pb(II) ions from aqueous solution using multiwall carbon nanotubes synthesized by microwave chemical

vapor deposition technique," *Journal of Environmental Sciences (China)*, vol. 45, no. Ii, pp. 143–155, 2016, doi: 10.1016/j.jes.2015.12.025.

[136] V. Datsyuk *et al.*, "Chemical oxidation of multiwalled carbon nanotubes," *Carbon N Y*, vol. 46, no. 6, pp. 833–840, May 2008, doi: 10.1016/j.carbon.2008.02.012.

[137] J. L. Bahr, E. T. Mickelson, M. J. Bronikowski, R. E. Smalley, and J. M. Tour, "Dissolution of small diameter single-wall carbon nanotubes in organic solvents?," *Chemical Communications*, no. 2, pp. 193–194, Jan. 2001, doi: 10.1039/b008042j.

[138] V. Singh, D. Joung, L. Zhai, S. Das, S. I. Khondaker, and S. Seal, "Graphene based materials: Past, present and future," *Progress in Materials Science*, vol. 56, no. 8. Elsevier Ltd, pp. 1178–1271, Oct. 10, 2011. doi: 10.1016/j.pmatsci.2011.03.003.

[139] T. Liu, S. Chen, and H. Liu, "Oil adsorption and reuse performance of multi-walled carbon nanotubes," *Procedia Engineering*, vol. 102, pp. 1896–1902, 2015, doi: 10.1016/j.proeng.2015.01.329.

[140] B. Wang, B. Gao, A. R. Zimmerman, and X. Lee, "Impregnation of multiwall carbon nanotubes in alginate beads dramatically enhances their adsorptive ability to aqueous methylene blue," *Chemical Engineering Research and Design*, vol. 133, pp. 235–242, May 2018, doi: 10.1016/j.cherd.2018.03.026.

[141] J. L. Gong *et al.*, "Removal of cationic dyes from aqueous solution using magnetic multi-wall carbon nanotube nanocomposite as adsorbent," *Journal of Hazardous Materials*, vol. 164, no. 2–3, pp. 1517–1522, May 2009, doi: 10.1016/j.jhazmat.2008.09.072.

[142] R. K. Ibrahim *et al.*, "A clean approach for functionalized carbon nanotubes by deep eutectic solvents and their performance in the adsorption of methyl orange from aqueous solution," *Journal of Environmental Management*, vol. 235, pp. 521–534, Apr. 2019, doi: 10.1016/j.jenvman.2019.01.070.

[143] Y. B. Yang, M. Rahimi, J. K. Singh, M. C. Böhm, and F. Müller-Plathe, "Adsorption and Condensation of SO2 in Double-Walled Carbon Nanotube Arrays Studied by Monte Carlo Simulations and Simple Analytical Models," *Journal of Physical Chemistry C*, vol. 120, no. 14, pp. 7510–7521, 2016, doi: 10.1021/acs.jpcc.5b08910.

[144] H. Al-Johani and M. A. Salam, "Kinetics and thermodynamic study of aniline adsorption by multi-walled carbon nanotubes from aqueous solution," *Journal of Colloid and Interface Science*, vol. 360, no. 2, pp. 760–767, Aug. 2011, doi: 10.1016/j.jcis.2011.04.097.

[145] X. Ren, C. Chen, M. Nagatsu, and X. Wang, "Carbon nanotubes as adsorbents in environmental pollution management: A review," *Chemical Engineering Journal*, vol. 170, no. 2–3. pp. 395–410, Jun. 01, 2011. doi: 10.1016/j.cej.2010.08.045.

[146] K. Yang, W. Wu, Q. Jing, W. Jiang, and B. Xing, "Competitive adsorption of naphthalene with 2,4-dichlorophenol and 4-chloroaniline on multiwalled carbon nanotubes," *Environmental Science and Technology*, vol. 44, no. 8, pp. 3021–3027, Apr. 2010, doi: 10.1021/es100018a.

[147] S. Agnihotri, J. P. B. Mota, M. Rostam-Abadi, and M. J. Rood, "Theoretical and experimental investigation of morphology and temperature effects on adsorption of organic vapors in single-walled carbon nanotubes," *Journal of Physical Chemistry B*, vol. 110, no. 15, pp. 7640–7647, 2006, doi: 10.1021/jp060040a.

[148] P. Kondratyuk, Y. Wang, J. K. Johnson, and J. T. Yates, "Observation of a one-dimensional adsorption site on carbon nanotubes: Adsorption of alkanes of different molecular lengths," *Journal of Physical Chemistry B*, vol. 109, no. 44, pp. 20999–21005, 2005, doi: 10.1021/jp0582078.

[149] S. M. Gatica, M. J. Bojan, G. Stan, and M. W. Cole, "Quasi-one- and two-dimensional transitions of gases adsorbed on nanotube bundles," *Journal of Chemical Physics*, vol. 114, no. 8, pp. 3765–3769, 2001, doi: 10.1063/1.1339886.

[150] S. Rols, M. R. Johnson, P. Zeppenfeld, M. Bienfait, O. E. Vilches, and J. Schneble, "Argon adsorption in open-ended single-wall carbon nanotubes," *Physical Review B - Condensed Matter and Materials Physics*, vol. 71, no. 15, pp. 1–8, 2005, doi: 10.1103/PhysRevB.71.155411.

[151] F. M. Machado and S. B. Fagan, "Carbon Nanoadsorbents Density of States," *Springer International Publishing Switzerland*, 2015, doi: 10.1007/978-3-319-18875-1.

[152] F. Su, C. Lu, K. R. Johnston, and S. Hu, *Kinetics, thermodynamics, and regeneration of BTEX adsorption in aqueous solutions via NaOCl-Oxidized carbon nanotubes*, 1st ed., no. X. Elsevier, 2010. doi: 10.1016/B978-0-08-054820-3.00005-8.

[153] J. Ma *et al.*, "Comparative Study of Graphene Hydrogels and Aerogels Reveals the Important Role of Buried Water in Pollutant Adsorption," *Environmental Science and Technology*, vol. 51, no. 21, pp. 12283–12292, 2017, doi: 10.1021/acs.est.7b02227.

[154] L. Chen, R. S. Smith, B. D. Kay, and Z. Dohnálek, "Adsorption of small hydrocarbons on rutile TiO2(110)," *Surface Science*, vol. 650, pp. 83–92, 2016, doi: 10.1016/j.susc.2015.11.002.

[155] X. Tan *et al.*, “Superhydrophobic/superoleophilic corn straw as an eco-friendly oil sorbent for the removal of spilled oil,” *Clean Technologies and Environmental Policy*, vol. 23, no. 1, pp. 145–152, Jan. 2021, doi: 10.1007/s10098-019-01808-8.

[156] Q. Cao, Q. Yu, D. W. Connell, and G. Yu, “Titania/carbon nanotube composite (TiO2/CNT) and its application for removal of organic pollutants,” *Clean Technologies and Environmental Policy*, vol. 15, no. 6. Springer Verlag, pp. 871–880, 2013. doi: 10.1007/s10098-013-0581-y.

[157] R. Zandipak and S. Sobhanardakani, “Novel mesoporous Fe3O4/SiO2/CTAB–SiO2 as an effective adsorbent for the removal of amoxicillin and tetracycline from water,” *Clean Technologies and Environmental Policy*, vol. 20, no. 4, pp. 871–885, May 2018, doi: 10.1007/s10098-018-1507-5.

[158] S. Kirti, V. M. Bhandari, J. Jena, L. G. Sorokhaibam, and A. S. Bhattacharyya, “Exploiting functionalities of biomass in nanocomposite development: application in dye removal and disinfection along with process intensification,” *Clean Technologies and Environmental Policy*, vol. 20, no. 5, pp. 981–994, Jul. 2018, doi: 10.1007/s10098-018-1519-1.

[159] S. S. M. Hassan, A. H. Kamel, A. A. Hassan, A. E. G. E. Amr, H. A. El-Naby, and E. A. Elsayed, “A sno2/ceo2 nano-composite catalyst for alizarin dye removal from aqueous solutions,” *Nanomaterials*, vol. 10, no. 2, Feb. 2020, doi: 10.3390/nano10020254.

[160] R. T. Rasheed, H. S. Mansoor, R. R. Al-Shaikhly, T. A. Abdullah, A. D. Salman, and T. Juzsakova, “Synthesis and catalytic activity studies of α-MnO<inf>2</inf> nanorodes, rutile TiO<inf>2</inf> and its composite prepared by hydrothermal method,” in *AIP Conference Proceedings*, 2020, vol. 2213. doi: 10.1063/5.0000228.

[161] T. A. Abdullah *et al.*, “Promotional effect of metal oxides (MxOy = TiO2, V2O5) on multi-walled carbon nanotubes (MWCNTs) for kerosene removal from contaminated water,” *Materials Letters*, vol. 292, Jun. 2021, doi: 10.1016/j.matlet.2021.129612.

[162] Q. Duan, J. Lee, Y. Liu, and H. Qi, “Preparation and Photocatalytic Performance of MWCNTs/TiO2 Nanocomposites for Degradation of Aqueous Substrate,” *Journal of Chemistry*, vol. 2016, 2016, doi: 10.1155/2016/1262017.

[163] S. Mallakpour and E. Khadem, “Carbon nanotube–metal oxide nanocomposites: Fabrication, properties and applications,” *Chemical Engineering Journal*, vol. 302, pp. 344–367, 2016, doi: 10.1016/j.cej.2016.05.038.

[164] J. H. Li, R. Y. Hong, G. H. Luo, Y. Zheng, H. Z. Li, and D. G. Wei, “An easy approach to encapsulating Fe3O4 nanoparticles in multiwalled carbon nanotubes,” *Xinxing Tan Cailiao/New Carbon Materials*, vol. 25, no. 3, pp. 192–198, 2010, doi: 10.1016/S1872-5805(09)60026-3.

[165] X. J. Pang, J. Zhang, G. W. Qi, X. H. Dai, J. P. Zhou, and S. Y. Zhang, “Multi-walled carbon nanotube-reinforced porous iron oxide as a superior anode material for lithium ion battery,” *Journal of Alloys and Compounds*, vol. 640, pp. 8–14, 2015, doi: 10.1016/j.jallcom.2015.03.188.

[166] J. Hu, D. Shao, C. Chen, G. Sheng, X. Ren, and X. Wang, “Removal of 1-naphthylamine from aqueous solution by multiwall carbon nanotubes/iron oxides/cyclodextrin composite,” *Journal of Hazardous Materials*, vol. 185, no. 1, pp. 463–471, 2011, doi: 10.1016/j.jhazmat.2010.09.055.

[167] A. A. Akinpelu, M. E. Ali, M. R. Johan, R. Saidur, M. A. Qurban, and T. A. Saleh, “Polycyclic aromatic hydrocarbons extraction and removal from wastewater by carbon nanotubes: A review of the current technologies, challenges and prospects,” *Process Safety and Environmental Protection*, vol. 122, pp. 68–82, 2019, doi: 10.1016/j.psep.2018.11.006.

[168] W. F. Elmobarak and F. Almomani, “Application of Fe3O4 magnetite nanoparticles grafted in silica (SiO2) for oil recovery from oil in water emulsions,” *Chemosphere*, vol. 265, p. 129054, 2021, doi: 10.1016/j.chemosphere.2020.129054.

[169] K. Yamashita, S. Okada, and H. Sawada, “Preparation of fluoroalkyl end-capped vinyltrimethoxysilane oligomeric silica/magnetite composites – Application to separation of oil and water,” *Colloids and Surfaces A: Physicochemical and Engineering Aspects*, vol. 581, no. August, p. 123668, 2019, doi: 10.1016/j.colsurfa.2019.123668.

[170] M. Herrero, K. Núñez, R. Gallego, J. C. Merino, and J. M. Pastor, “Control of molecular weight and polydispersity in polyethylene/needle-like shaped clay nanocomposites obtained by in situ polymerization with metallocene catalysts,” *European Polymer Journal*, vol. 75, pp. 125–141, 2016, doi: 10.1016/j.eurpolymj.2015.12.005.

[171] P. A. Zapata, C. Belver, R. Quijada, P. Aranda, and E. Ruiz-Hitzky, “Silica/clay organo-heterostructures to promote polyethylene-clay nanocomposites by in situ polymerization,” *Applied Catalysis A: General*, vol. 453, pp. 142–150, 2013, doi: 10.1016/j.apcata.2012.12.012.

[172] S. A. H. Jalali, A. Allafchian, H. Bahramian, and R. Amiri, “An antibacterial study of a new magnetite silver nanocomposite,” *Journal of Environmental Chemical Engineering*, vol. 5, no. 6, pp. 5786–5792, 2017, doi: 10.1016/j.jece.2017.11.016.

[173] H. A. Raslan, H. A. El-Saied, R. M. mohamed, and N. M. Yousif, “Gamma radiation induced fabrication of styrene butadiene rubber/ magnetite nanocomposites for positive temperature coefficient thermistors application,” *Composites Part B: Engineering*, vol. 176, no. February, p. 107326, 2019, doi: 10.1016/j.compositesb.2019.107326.
[174] S. Palchoudhury and J. R. Lead, “A facile and cost-effective method for separation of oil-water mixtures using polymer-coated iron oxide nanoparticles,” *Environmental Science and Technology*, vol. 48, no. 24, pp. 14558–14563, 2014, doi: 10.1021/es5037755.
[175] S. Huggias, P. A. Bolla, J. C. Azcarate, M. A. Serradell, M. L. Casella, and P. J. Peruzzo, “Noble metal nanoparticles-based heterogeneous bionano-catalysts supported on S-layer protein/polyurethane system,” *Catalysis Today*, vol. 372, no. August, pp. 98–106, 2021, doi: 10.1016/j.cattod.2020.09.016.
[176] R. T. Rasheed *et al.*, “Synthesis, characterization of V<inf>2</inf>O<inf>5</inf> nanoparticles and determination of catalase mimetic activity by new colorimetric method,” *Journal of Thermal Analysis and Calorimetry*, vol. 145, no. 2, 2021, doi: 10.1007/s10973-020-09725-5.
[177] T. A. Abdullah *et al.*, “V<inf>2</inf> O<inf>5</inf>, CeO<inf>2</inf> and Their MWCNTs Nanocomposites Modified for the Removal of Kerosene from Water,” *Nanomaterials*, vol. 12, no. 2, 2022, doi: 10.3390/nano12020189.
[178] Z. F. Yang, L. Y. Li, C. te Hsieh, and R. S. Juang, “Co-precipitation of magnetic Fe3O4 nanoparticles onto carbon nanotubes for removal of copper ions from aqueous solution,” *J Taiwan Inst Chem Eng*, vol. 82, pp. 56–63, Jan. 2018, doi: 10.1016/j.jtice.2017.11.009.
[179] U. Staudinger, L. Jakisch, and L. Hilbig, “Dispersion and localization behavior of modified mwcnts in immiscible polymer blends of polystyrene and polybutadiene and in corresponding nanostructured block copolymers,” *Journal of Composites Science*, vol. 4, no. 2, 2020, doi: 10.3390/jcs4020040.
[180] T. A. Abdullah *et al.*, “V2O5 NANOPARTICLES FOR DYES REMOVAL FROM WATER,” *Chemistry Journal of Moldova*, vol. 16, no. 2, 2021, doi: 10.19261/CJM.2021.911.
[181] T. A. Abdullah *et al.*, “Polyethylene over magnetite-multiwalled carbon nanotubes for kerosene removal from water,” *Chemosphere*, vol. 287, 2022, doi: 10.1016/j.chemosphere.2021.132310.
[182] A. M. Aljeboree, A. N. Alshirifi, and A. F. Alkaim, “Kinetics and equilibrium study for the adsorption of textile dyes on coconut shell activated carbon,” *Arabian Journal of Chemistry*, vol. 10, pp. S3381–S3393, May 2017, doi: 10.1016/j.arabjc.2014.01.020.
[183] A. T. Lawal, “Recent progress in graphene based polymer nanocomposites,” *Cogent Chemistry*, vol. 6, no. 1, p. 1833476, Jan. 2020, doi: 10.1080/23312009.2020.1833476.
[184] M. K. Nazal, M. Khaled, M. A. Atieh, I. H. Aljundi, G. A. Oweimreen, and A. M. Abulkibash, “The nature and kinetics of the adsorption of dibenzothiophene in model diesel fuel on carbonaceous materials loaded with aluminum oxide particles,” *Arabian Journal of Chemistry*, vol. 12, no. 8, pp. 3678–3691, Dec. 2019, doi: 10.1016/j.arabjc.2015.12.003.
[185] M. J. Nazarahari *et al.*, “Synthesis, characterization, and assessment of a ceo2@nanoclay nanocomposite for enhanced oil recovery,” *Nanomaterials*, vol. 10, no. 11, pp. 1–26, Nov. 2020, doi: 10.3390/nano10112280.
[186] S. Padmajan Sasikala, K. v. Mahesh, P. Prabhakaran, A. Peer Mohammed, and S. Ananthakumar, “Multiwall carbon nanotube reinforced teflon fibrils for oil spill clean up and its effective recycling as textile dye sorbent,” *Journal of Environmental Management*, vol. 211, pp. 198–205, Apr. 2018, doi: 10.1016/j.jenvman.2018.01.011.
[187] X. Zhou *et al.*, “Multiwalled carbon nanotubes-V2O5 integrated composite with nanosized architecture as a cathode material for high performance lithium ion batteries,” *Journal of Materials Chemistry A*, vol. 1, no. 48, pp. 15459–15468, 2013, doi: 10.1039/c3ta13143b.
[188] D. Malaescu, I. Grozescu, P. Sfirloaga, P. Vlazan, and C. N. Marin, “The electrical properties of some composite materials based on sodium and tantalum oxides,” *Acta Physica Polonica A*, vol. 129, no. 1, pp. 133–137, Jan. 2016, doi: 10.12693/APhysPolA.129.133.
[189] E. Burstein, “LETTERS TO THE ED ITOR Anoma1ous Optical Absorption Limit in InSb.”
[190] S. Tewari and A. Bhattacharjee, “Structural, electrical and optical studies on spray-deposited aluminium-doped ZnO thin films,” 2011.
[191] A. Biedunkiewicz, U. Gabriel, P. Figiel, and M. Sabara, “Investigations on NH4VO3 thermal decomposition in dry air,” *Journal of Thermal Analysis and Calorimetry*, vol. 108, no. 3, pp. 965–970, 2012, doi: 10.1007/s10973-011-2149-6.
[192] A. G. S. Filho, O. P. Ferreira, E. J. G. Santos, J. M. Filho, and O. L. Alves, “Raman spectra in vanadate nanotubes revisited,” *Nano Letters*, vol. 4, no. 11, pp. 2099–2104, Nov. 2004, doi: 10.1021/nl0488477.

[193] J. Yener, T. Kopac, G. Dogu, and T. Dogu, “Dynamic analysis of sorption of Methylene Blue dye on granular and powdered activated carbon,” *Chemical Engineering Journal*, vol. 144, no. 3, pp. 400–406, Nov. 2008, doi: 10.1016/j.cej.2008.02.009.

[194] P. M. Thabede, N. D. Shooto, and E. B. Naidoo, “Removal of methylene blue dye and lead ions from aqueous solution using activated carbon from black cumin seeds,” *South African Journal of Chemical Engineering*, vol. 33, pp. 39–50, Jul. 2020, doi: 10.1016/j.sajce.2020.04.002.

[195] S. Karagöz, T. Tay, S. Ucar, and M. Erdem, “Activated carbons from waste biomass by sulfuric acid activation and their use on methylene blue adsorption,” *Bioresource Technology*, vol. 99, no. 14, pp. 6214–6222, Sep. 2008, doi: 10.1016/j.biortech.2007.12.019.

[196] Y. C. Sharma and Uma, “Optimization of parameters for adsorption of methylene blue on a low-cost activated carbon,” *Journal of Chemical and Engineering Data*, vol. 55, no. 1, pp. 435–439, Jan. 2010, doi: 10.1021/je900408s.

[197] T. Sarat Chandra *et al.*, “Defatted algal biomass as a non-conventional low-cost adsorbent: Surface characterization and methylene blue adsorption characteristics,” *Bioresource Technology*, vol. 184, pp. 395–404, May 2015, doi: 10.1016/j.biortech.2014.10.018.

[198] S. Mallakpour and M. Hatami, “An effective, low-cost and recyclable bio-adsorbent having amino acid intercalated LDH@Fe3O4/PVA magnetic nanocomposites for removal of methyl orange from aqueous solution,” *Applied Clay Science*, vol. 174, pp. 127–137, Jun. 2019, doi: 10.1016/j.clay.2019.03.026.

[199] T. H. Le, T. H. A. Ngo, V. T. Doan, L. M. T. Nguyen, and M. C. Le, “Preparation of Manganese Dioxide Nanoparticles on Laterite for Methylene Blue Degradation,” *Journal of Chemistry*, vol. 2019, 2019, doi: 10.1155/2019/1602752.

[200] A. Alagarsamy, S. Chandrasekaran, and A. Manikandan, “Green synthesis and characterization studies of biogenic zirconium oxide (ZrO2) nanoparticles for adsorptive removal of methylene blue dye,” *Journal of Molecular Structure*, vol. 1247, Jan. 2022, doi: 10.1016/j.molstruc.2021.131275.

[201] M. L. F. A. de Castro, M. L. B. Abad, D. A. G. Sumalinog, R. R. M. Abarca, P. Paoprasert, and M. D. G. de Luna, “Adsorption of Methylene Blue dye and Cu(II) ions on EDTA-modified bentonite: Isotherm, kinetic and thermodynamic studies,” *Sustainable Environment Research*, vol. 28, no. 5, pp. 197–205, 2018, doi: 10.1016/j.serj.2018.04.001.

[202] T. Zhou *et al.*, “Effective adsorption of light green anionic dye from solution by CPB modified peanut in column mode,” *Journal of Molecular Liquids*, vol. 211, pp. 909–914, 2015, doi: 10.1016/j.molliq.2015.08.018.

[203] G. William Kajjumba, S. Emik, A. Öngen, H. Kurtulus Özcan, and S. Aydın, “Modelling of Adsorption Kinetic Processes—Errors, Theory and Application,” *Advanced Sorption Process Applications*, pp. 1–19, 2019, doi: 10.5772/intechopen.80495.

[204] N. Somsesta, V. Sricharoenchaikul, and D. Aht-Ong, “Adsorption removal of methylene blue onto activated carbon/cellulose biocomposite films: Equilibrium and kinetic studies,” *Materials Chemistry and Physics*, vol. 240, no. June 2019, p. 122221, 2020, doi: 10.1016/j.matchemphys.2019.122221.

[205] T. H. Tran *et al.*, “Adsorption isotherms and kinetic modeling of methylene blue dye onto a carbonaceous hydrochar adsorbent derived from coffee husk waste,” *Science of the Total Environment*, vol. 725, p. 138325, 2020, doi: 10.1016/j.scitotenv.2020.138325.

[206] F. J. Tuli, A. Hossain, A. K. M. F. Kibria, A. R. M. Tareq, S. M. M. A. Mamun, and A. K. M. A. Ullah, “Removal of methylene blue from water by low-cost activated carbon prepared from tea waste: A study of adsorption isotherm and kinetics,” *Environmental Nanotechnology, Monitoring and Management*, vol. 14, no. August, p. 100354, 2020, doi: 10.1016/j.enmm.2020.100354.

[207] B. Choudhury and A. Choudhury, “Luminescence characteristics of cobalt doped TiO2 nanoparticles,” *Journal of Luminescence*, vol. 132, no. 1, pp. 178–184, 2012, doi: 10.1016/j.jlumin.2011.08.020.

[208] M. Waqif, P. Bazin, O. Saur, J. C. Lavalley, G. Blanchard, and O. Touret, “Study of ceria sulfation,” *Applied Catalysis B: Environmental*, vol. 11, no. 2, pp. 193–205, 1997, doi: 10.1016/S0926-3373(96)00040-9.

[209] H. Chang *et al.*, “Comparison of preparation methods for ceria catalyst and the effect of surface and bulk sulfates on its activity toward NH3-SCR,” *Journal of Hazardous Materials*, vol. 262, no. x, pp. 782–788, 2013, doi: 10.1016/j.jhazmat.2013.09.043.

[210] D. M. D. M. Prabaharan, K. Sadaiyandi, M. Mahendran, and S. Sagadevan, “Structural, Optical, Morphological and Dielectric Properties of Cerium Oxide Nanoparticles,” *Materials Research*, vol. 19, no. 2, pp. 478–482, 2016, doi: 10.1590/1980-5373-MR-2015-0698.

[211] M. G. Sujana, K. K. Chattopadyay, and S. Anand, “Characterization and optical properties of nano-ceria synthesized by surfactant-mediated precipitation technique in mixed solvent system,” *Applied Surface Science*, vol. 254, no. 22, pp. 7405–7409, 2008, doi: 10.1016/j.apsusc.2008.05.341.
[212] S. Costa, E. Borowiak-Palen, M. Kruszyñska, A. Bachmatiuk, and R. J. Kaleńczuk, “Characterization of carbon nanotubes by Raman spectroscopy,” *Materials Science- Poland*, vol. 26, no. 2, pp. 433–441, 2008.
[213] J. H. Lehman, M. Terrones, E. Mansfield, K. E. Hurst, and V. Meunier, “Evaluating the characteristics of multiwall carbon nanotubes,” *Carbon N Y*, vol. 49, no. 8, pp. 2581–2602, 2011, doi: 10.1016/j.carbon.2011.03.028.
[214] A. Jorio and R. Saito, “Raman spectroscopy for carbon nanotube applications,” *Journal of Applied Physics*, vol. 129, no. 2, 2021, doi: 10.1063/5.0030809.
[215] Puech *et al.*, “Analyzing the Raman Spectra of Graphenic Carbon Materials from Kerogens to Nanotubes: What Type of Information Can Be Extracted from Defect Bands?,” *C — Journal of Carbon Research*, vol. 5, no. 4, p. 69, 2019, doi: 10.3390/c5040069.
[216] H. Murphy, P. Papakonstantinou, and T. I. T. Okpalugo, “Raman study of multiwalled carbon nanotubes functionalized with oxygen groups,” *Journal of Vacuum Science & Technology B: Microelectronics and Nanometer Structures*, vol. 24, no. 2, p. 715, 2006, doi: 10.1116/1.2180257.
[217] Y. Osswald, S.; Havel, M.; Gogotsi, “Monitoring oxidation of multiwalled carbon nanotubes by Raman spectroscopy,” *J. Raman Spectrosc*, vol. 38, pp. 728–736, 2007.
[218] R. A. DiLeo, B. J. Landi, and R. P. Raffaelle, “Purity assessment of multiwalled carbon nanotubes by Raman spectroscopy,” *Journal of Applied Physics*, vol. 101, no. 6, 2007, doi: 10.1063/1.2712152.
[219] P. Shvets, O. Dikaya, K. Maksimova, and A. Goikhman, “A review of Raman spectroscopy of vanadium oxides,” *Journal of Raman Spectroscopy*, vol. 50, no. 8, pp. 1226–1244, 2019, doi: 10.1002/jrs.5616.
[220] C. Schilling, A. Hofmann, C. Hess, and M. V. Ganduglia-Pirovano, “Raman Spectra of Polycrystalline CeO2: A Density Functional Theory Study,” *Journal of Physical Chemistry C*, vol. 121, no. 38, pp. 20834–20849, 2017, doi: 10.1021/acs.jpcc.7b06643.
[221] C. Su, B. Y. Hong, and C. M. Tseng, “Sol-gel preparation and photocatalysis of titanium dioxide,” in *Catalysis Today*, 2004, vol. 96, no. 3, pp. 119–126. doi: 10.1016/j.cattod.2004.06.132.
[222] D. Zhao, D. Li, X. Wu, and E. H. Han, “Batch supercritical hydrothermal synthesis of CeO2 nanoparticles,” *Advanced Materials Research*, vol. 284–286, pp. 773–780, 2011, doi: 10.4028/www.scientific.net/AMR.284-286.773.
[223] R. T. Rasheed *et al.*, “Synthesis, characterization of V2O5 nanoparticles and determination of catalase mimetic activity by new colorimetric method,” *Journal of Thermal Analysis and Calorimetry*, vol. 145, no. 2, pp. 297–307, 2021, doi: 10.1007/s10973-020-09725-5.
[224] P. Wang, F. Meng, C. Gao, W. Xie, J. Wang, and A. Li, “Structural, morphological and optical characteristics of fusiform Co-doped CeO2 via a facile hydrothermal method,” *Journal of Materials Science: Materials in Electronics*, vol. 29, no. 13, pp. 11482–11488, Jul. 2018, doi: 10.1007/s10854-018-9243-5.
[225] N. T. Abdel-Ghani, G. A. El-Chaghaby, and F. S. Helal, “Individual and competitive adsorption of phenol and nickel onto multiwalled carbon nanotubes,” *Journal of Advanced Research*, vol. 6, no. 3, pp. 405–415, May 2015, doi: 10.1016/j.jare.2014.06.001.
[226] K. A. Shah and B. A. Tali, “Synthesis of carbon nanotubes by catalytic chemical vapour deposition: A review on carbon sources, catalysts and substrates,” *Materials Science in Semiconductor Processing*, vol. 41, pp. 67–82, 2016, doi: 10.1016/j.mssp.2015.08.013.
[227] N. Sezer and M. Koç, “Oxidative acid treatment of carbon nanotubes,” *Surfaces and Interfaces*, vol. 14, no. July 2018, pp. 1–8, 2019, doi: 10.1016/j.surfin.2018.11.001.
[228] J. P. Bom, D.; Andrews, R.; Jacques, D.; Anthony, J.; Chen, B.; Meier, M.S.; Selegue, “Thermogravimetric Analysis of the Oxidation of Multiwalled Carbon Nanotubes: Evidence for the Role of Defect Sites in Carbon Nanotube Chemistry,” *Nano Lett*, vol. 2, pp. 615–619, 2002.
[229] A. Trovarelli, “Catalytic Properties of Ceria and CeO2-Containing Materials,” *Catal. Rev.*, vol. 38, pp. 439–520, 1996.
[230] I. E. Wachs, “Catalysis science of supported vanadium oxide catalysts,” *Dalton Transactions*, vol. 42, 2013.
[231] A. Vita, “Catalytic Applications of CeO 2 -Based Materials,” pp. 5–8, 2020.
[232] C. Notthoff, M. Winterer, A. Beckel, M. Geller, and J. Heindl, “Spatial high resolution energy dispersive X-ray spectroscopy on thin lamellas,” *Ultramicroscopy*, vol. 129, pp. 30–35, 2013, doi: 10.1016/j.ultramic.2013.02.008.

[233] T. A. Abdullah *et al.*, “Promotional effect of metal oxides (MxOy = TiO2, V2O5) on multi-walled carbon nanotubes (MWCNTs) for kerosene removal from contaminated water,” *Materials Letters*, vol. 292, 2021, doi: 10.1016/j.matlet.2021.129612.
[234] M. E. Birch, T. A. Ruda-Eberenz, M. Chai, R. Andrews, and R. L. Hatfield, “Properties that influence the specific surface areas of carbon nanotubes and nanofibers,” *Annals of Occupational Hygiene*, vol. 57, no. 9, pp. 1148–1166, 2013, doi: 10.1093/annhyg/met042.
[235] R. Kecili and C. M. Hussain, *Mechanism of adsorption on nanomaterials*. Elsevier Inc., 2018. doi: 10.1016/B978-0-12-812792-6.00004-2.
[236] Sadeghi, AM, Bagheri, M G, Zohuriaan, MJ, “Nitrate removal from aqueous solutions by adsorption onto hydrogel-rice husk biochar composite,” *Water environmental research*, 2019.
[237] M. C. Ribas, M. A. E. de Franco, M. A. Adebayo, E. C. Lima, G. M. B. Parkes, and L. A. Feris, “Adsorption of Procion Red MX - 5B dye from aqueous solution using homemade peach and commercial activated carbons,” *Applied Water Science*, vol. 10, no. 6, pp. 1–13, 2020, doi: 10.1007/s13201-020-01237-9.
[238] A. Rezvanpour, R. Roostaazad, M. Hesampour, M. Nyström, and C. Ghotbi, “Effective factors in the treatment of kerosene-water emulsion by using UF membranes,” *Journal of Hazardous Materials*, vol. 161, no. 2–3, pp. 1216–1224, 2009, doi: 10.1016/j.jhazmat.2008.04.074.
[239] S. Mustapha *et al.*, *Application of TiO2 and ZnO nanoparticles immobilized on clay in wastewater treatment: a review*, vol. 10, no. 1. Springer International Publishing, 2020. doi: 10.1007/s13201-019-1138-y.
[240] F. A. Dawodu and K. G. Akpomie, “Simultaneous adsorption of Ni(II) and Mn(II) ions from aqueous solution unto a Nigerian kaolinite clay,” *Journal of Materials Research and Technology*, vol. 3, no. 2, pp. 129–141, 2014, doi: 10.1016/j.jmrt.2014.03.002.
[241] M. A. Salam and R. Burk, “Synthesis and characterization of multi-walled carbon nanotubes modified with octadecylamine and polyethylene glycol,” *Arabian Journal of Chemistry*, vol. 10, pp. S921–S927, 2017, doi: 10.1016/j.arabjc.2012.12.028.
[242] M. E. Compeán-Jasso, F. Ruiz, J. R. Martínez, and A. Herrera-Gómez, “Magnetic properties of magnetite nanoparticles synthesized by forced hydrolysis,” *Materials Letters*, vol. 62, no. 27, pp. 4248–4250, 2008, doi: 10.1016/j.matlet.2008.06.053.
[243] K. S. Loh, Y. H. Lee, A. Musa, A. A. Salmah, and I. Zamri, “Use of Fe3O4 nanoparticles for enhancement of biosensor response to the herbicide 2,4-dichlorophenoxyacetic acid,” *Sensors*, vol. 8, no. 9, pp. 5775–5791, 2008, doi: 10.3390/s8095775.
[244] F. Z. Benabid, N. Kharchi, F. Zouai, A. H. I. Mourad, and D. Benachour, “Impact of co-mixing technique and surface modification of ZnO nanoparticles using stearic acid on their dispersion into HDPE to produce HDPE/ZnO nanocomposites,” *Polymers and Polymer Composites*, vol. 27, no. 7, pp. 389–399, 2019, doi: 10.1177/0967391119847353.
[245] P. Sen, K. Suresh, R. Vinoth Kumar, M. Kumar, and G. Pugazhenthi, “A simple solvent blending coupled sonication technique for synthesis of polystyrene (PS)/multi-walled carbon nanotube (MWCNT) nanocomposites: Effect of modified MWCNT content,” *Journal of Science: Advanced Materials and Devices*, vol. 1, no. 3, pp. 311–323, Sep. 2016, doi: 10.1016/j.jsamd.2016.06.016.
[246] L. Qiu, Y. Chen, Y. Yang, L. Xu, and X. Liu, “A study of surface modifications of carbon nanotubes on the properties of polyamide 66/multiwalled carbon nanotube composites,” *Journal of Nanomaterials*, vol. 2013, 2013, doi: 10.1155/2013/252417.
[247] G. Trykowski, S. Biniak, L. Stobinski, and B. Lesiak, “Preliminary investigations into the purification and functionalization of multiwall carbon nanotubes,” in *Acta Physica Polonica A*, 2010, vol. 118, no. 3, pp. 515–518. doi: 10.12693/APhysPolA.118.515.
[248] H. Akgün, E. Yapıcı, Z. Günkaya, A. Özkan, and M. Banar, “Utilization of liquid product through pyrolysis of LDPE and C/LDPE as commercial wax”, doi: 10.1007/s11356-021-13999-z/Published.
[249] D. Dey, N. Chandra Murmu, and P. Banerjee, “Tailor-made synthesis of an melamine-based aminal hydrophobic polymer for selective adsorption of toxic organic pollutants: An initiative towards wastewater purification,” *RSC Advances*, vol. 9, no. 13, pp. 7469–7478, 2019, doi: 10.1039/c9ra00453j.
[250] M. S. Khan, Inamullah, M. Sohail, and N. S. Khattak, “Conversion of Mixed Low-Density Polyethylene Wastes into Liquid Fuel by Novel CaO/SiO2 Catalyst,” *Journal of Polymers and the Environment*, vol. 24, no. 3, pp. 255–263, Sep. 2016, doi: 10.1007/s10924-016-0768-5.
[251] T. A. Abdullah *et al.*, “Polystyrene-fe<inf>3</inf> o<inf>4</inf>-mwcnts nanocomposites for toluene removal from water,” *Materials*, vol. 14, no. 19, 2021, doi: 10.3390/ma14195503.
[252] H. Anjum, K. Johari, N. Gnanasundaram, A. Appusamy, and M. Thanabalan, “Investigation of green functionalization of multiwall carbon nanotubes and its application in adsorption of benzene,

toluene & p-xylene from aqueous solution," *Journal of Cleaner Production*, vol. 221, pp. 323–338, Jun. 2019, doi: 10.1016/j.jclepro.2019.02.233.
[253] M. Zdrojek, W. Gebicki, C. Jastrzebski, T. Melin, and A. Huczko, "Studies of Multiwall Carbon Nanotubes using Raman Spectroscopy and Atomic Force Microscopy," vol. 100, pp. 265–268, 2004, doi: 10.4028/www.scientific.net/SSP.99-100.265.
[254] M. T. Bankole *et al.*, "Selected Heavy Metals Removal From Electroplating Wastewater by Purified and Polyhydroxylbutyrate Functionalized Carbon Nanotubes Adsorbents," *Scientific Reports*, vol. 9, no. 1, pp. 1–19, 2019, doi: 10.1038/s41598-018-37899-4.
[255] L. Bokobza and J. Zhang, "Raman spectroscopic characterization of multiwall carbon nanotubes and of composites," *Express Polymer Letters*, vol. 6, no. 7, pp. 601–608, 2012, doi: 10.3144/expresspolymlett.2012.63.
[256] S. A. Chernyak *et al.*, "Oxidation, defunctionalization and catalyst life cycle of carbon nanotubes: A Raman spectroscopy view," *Physical Chemistry Chemical Physics*, vol. 19, no. 3, pp. 2276–2285, 2017, doi: 10.1039/c6cp04657f.
[257] S. Rahmam, N. M. Mohamed, and S. Sufian, "Effect of acid treatment on the multiwalled carbon nanotubes," *Materials Research Innovations*, vol. 18, pp. S6-196-S6-199, Dec. 2014, doi: 10.1179/1432891714Z.0000000001038.
[258] M. Stoia, R. Istratie, and C. Păcurariu, "Investigation of magnetite nanoparticles stability in air by thermal analysis and FTIR spectroscopy," *Journal of Thermal Analysis and Calorimetry*, vol. 125, no. 3, pp. 1185–1198, Sep. 2016, doi: 10.1007/s10973-016-5393-y.
[259] X. Zhang, Q. Zhang, and J. Zheng, "Effect and mechanism of iron oxide modified carbon nanotubes on thermal oxidative stability of silicone rubber," *Composites Science and Technology*, vol. 99, pp. 1–7, Jul. 2014, doi: 10.1016/j.compscitech.2014.05.003.
[260] "Goworek2009_Article_ThermalDegradationOfCTABInAs-s".
[261] K. Okiel, M. El-Sayed, and M. Y. El-Kady, "Treatment of oil–water emulsions by adsorption onto activated carbon, bentonite and deposited carbon," *Egyptian Journal of Petroleum*, vol. 20, no. 2, pp. 9–15, Jun. 2011, doi: 10.1016/j.ejpe.2011.06.002.
[262] S. Ibrahim, S. Wang, and H. M. Ang, "Removal of emulsified oil from oily wastewater using agricultural waste barley straw," *Biochemical Engineering Journal*, vol. 49, no. 1, pp. 78–83, Mar. 2010, doi: 10.1016/j.bej.2009.11.013.
[263] S. M. Sidik, A. A. Jalil, S. Triwahyono, S. H. Adam, M. A. H. Satar, and B. H. Hameed, "Modified oil palm leaves adsorbent with enhanced hydrophobicity for crude oil removal," *Chemical Engineering Journal*, vol. 203, pp. 9–18, Sep. 2012, doi: 10.1016/j.cej.2012.06.132.
[264] A. Abbas, B. A. Abussaud, Ihsanullah, N. A. H. Al-Baghli, and H. H. Redhwi, "Adsorption of Toluene and Paraxylene from Aqueous Solution Using Pure and Iron Oxide Impregnated Carbon Nanotubes: Kinetics and Isotherms Study," *Bioinorganic Chemistry and Applications*, vol. 2017, pp. 1–11, 2017, doi: 10.1155/2017/2853925.
[265] J. Mohammed, N. S. Nasri, M. A. Ahmad Zaini, U. D. Hamza, and F. N. Ani, "Adsorption of benzene and toluene onto KOH activated coconut shell based carbon treated with NH3," *International Biodeterioration and Biodegradation*, vol. 102, pp. 245–255, Aug. 2015, doi: 10.1016/j.ibiod.2015.02.012.
[266] N. Al-Jammal *et al.*, "Functionalized carbon nanotubes for hydrocarbon removal from water," *Journal of Environmental Chemical Engineering*, vol. 8, no. 2, 2020, doi: 10.1016/j.jece.2019.103570.
[267] P. Adowei, E. Wariboko, and D. Markmanuel, "REMOVAL OF LOW CONCENTRATION OF KEROSENE FROM WATER USING NIPA PALM (NYPA FRUITICANS WURMB) FRUIT FIBRE," *International Journal of Research -GRANTHAALAYAH*, vol. 8, no. 6, pp. 1–9, Jun. 2020, doi: 10.29121/granthaalayah.v8.i6.2020.462.
[268] C. A. Franco, N. N. Nassar, and F. B. Cortés, "Removal of oil from oil-in-saltwater emulsions by adsorption onto nano-alumina functionalized with petroleum vacuum residue," *Journal of Colloid and Interface Science*, vol. 433, pp. 58–67, Nov. 2014, doi: 10.1016/j.jcis.2014.07.011.
[269] D. F. Santos, A. R. Chaves, and I. C. Ostroski, "Naphthenic acid removal in model and real aviation kerosene mixture," *Chemical Engineering Communications*, vol. 208, no. 10, pp. 1405–1418, 2021, doi: 10.1080/00986445.2020.1783539.
[270] M. Gao, Q. Ma, Q. Lin, J. Chang, and H. Ma, "Fabrication and adsorption properties of hybrid fly ash composites," *Applied Surface Science*, vol. 396, pp. 400–411, 2017, doi: 10.1016/j.apsusc.2016.10.167.
[271] H. I. Kelle, "Comparative analysis of removal of crude oil and some refined petroleum products from the environment using rice husk: Adsorption isotherm and kinetic studies," *Nigerian Journal of Basic and Applied Sciences*, vol. 26, no. 1, p. 1, 2019, doi: 10.4314/njbas.v26i1.1.

[272] E. M. Soliman, S. A. Ahmed, and A. A. Fadl, “Adsorptive removal of oil spill from sea water surface using magnetic wood sawdust as a novel nano-composite synthesized via microwave approach 03 Chemical Sciences 0306 Physical Chemistry (incl. Structural),” *Journal of Environmental Health Science and Engineering*, vol. 18, no. 1, pp. 79–90, 2020, doi: 10.1007/s40201-019-00440-4.

[273] C. R. Kennedy, S. Lin, and E. N. Jacobsen, “Die Kation-π-Wechselwirkung in der Katalyse mit niedermolekularen Verbindungen,” *Angewandte Chemie*, vol. 128, no. 41, pp. 12784–12814, Oct. 2016, doi: 10.1002/ange.201600547.

[274] B. Bina, M. M. Amin, A. Rashidi, and H. Pourzamani, “Benzene and toluene removal by carbon nanotubes fromaqueous solution,” *Archives of Environmental Protection*, vol. 38, no. 1, pp. 3–25, 2012, doi: 10.2478/v10265-012-0001-0.

[275] J. Hu, D. Shao, C. Chen, G. Sheng, X. Ren, and X. Wang, “Removal of 1-naphthylamine from aqueous solution by multiwall carbon nanotubes/iron oxides/cyclodextrin composite,” *Journal of Hazardous Materials*, vol. 185, no. 1, pp. 463–471, Jan. 2011, doi: 10.1016/j.jhazmat.2010.09.055.

Appendix A

Table 1 Spectral analysis data from the deconvolution of D- and G-bands and the calculated ratios. Ratio changes compared to the MWCNTs sample are displayed in brackets

Sample	Center	Area	Intensity	I_D/I_G	$I_D/I_{G'}$	$I_{G'}/I_D$	A_D/A_G	$A_D/A_{G'}$	$A_{G'}/A_D$
MWCNTs	1284	0.04722	0.001782	1.48	1.84	0.54	1.59	1.05	0.96
	1289	0.05887							
	1598	0.06684	0.001207						
	2561	0.10150	0.000862						
MWCNTs ox.	1289	0.06766	0.001419	1.44 (-0.04)	1.65 (-0.19)	0.61 (0.06)	1.48 (-0.11)	0.97 (-0.08)	1.03 (0.08)
	1289	0.03089							
	1599	0.06651	0.000988						
	2567	0.10176	0.000862						
Ce/MWCNTs	1289	0.06237	0.002172	1.60 (0.12)	2.74 (0.89)	0.37 (-0.18)	1.76 (0.17)	2.44 (1.39)	0.41 (-0.55)
	1289	0.07774							
	1599	0.07962	0.001361						
	2567	0.05748	0.000794						
V/MWCNTs	1289	0.04876	0.001454	1.40 (-0.08)	2.30 (0.46)	0.43 (-0.11)	1.40 (-0.18)	2.08 (1.03)	0.48 (-0.48)
	1289	0.07993							
	1600	0.09178	0.001041						
	2561	0.06200	0.000632						
CV:Ce/ MWCNTs	1289	0.06845	0.002304	1.78 (0.31)	2.65 (0.81)	0.38 (-0.17)	2.42 (0.84)	2.24 (1.19)	0.45 (-0.51)
	1289	0.09338							
	1598	0.06680	0.001291						
	2566	0.07237	0.000868						

Table 2 Mass loss data from the termoanalitical measurements

Sample	T start (°C)	T end (°C)	Mass loss step	Total mass loss	Residual mass	Estimated Ce-/V-oxide content (m/m%)
MWCNTs	21	190	0.15 mg (2.5 %)	5.28 mg (89.6 %)	0.614 mg (10.4 %)	n/a
	190	440	0.05 mg (0.8 %)			
	440	750	5.08 mg (86.2 %)			
	750	1016	0 mg (0 %)			
MWCNTs ox.	21	155	1.43 mg (20.1 %)	7.02 mg (98.5 %)	0.108 mg (1.5 %)	n/a
	155	366	1.32 mg (18.5 %)			
	366	500	0.32 mg (4.5 %)			
	500	730	3.84 mg (53.9 %)			
	730	1016	0.11 mg (1.5 %)			
Ce/MWCNTs	22	190	0.35 mg (5.1 %)	6.04 mg (86.6 %)	0.938 mg (13.4 %)	CeO_2: 11.9%
	190	360	0.33 mg (4.7 %)			
	360	485	0.49 mg (7 %)			
	485	700	4.86 mg (69.6 %)			
	700	1015	0.01 mg (0.2 %)			
V/MWCNTs	22	190	0.58 mg (8.4 %)	6.6 mg (94.8 %)	0.364 mg (5.2 %)	V_2O_5: 3.7%
	190	330	0.4 mg (5.7 %)			
	330	418	0.88 mg (12.6 %)			
	418	590	4.59 mg (65.8 %)			
	590	700	0.15 mg (2.1 %)			
	700	1015	0.01 mg (0.2 %)			
V:Ce/MWCNTs	21	190	0.52 mg (7.4 %)	6.21 mg (90.0 %)	0.694 mg (10.0 %)	CeO_2+V_2O_5: 8.5%
	190	316	0.25 mg (3.6 %)			
	316	422	1.02 mg (14.6 %)			
	422	545	3.42 mg (49.1 %)			
	545	700	1.01 mg (14.6 %)			
	700	1016	0.06 mg (0.8 %)			

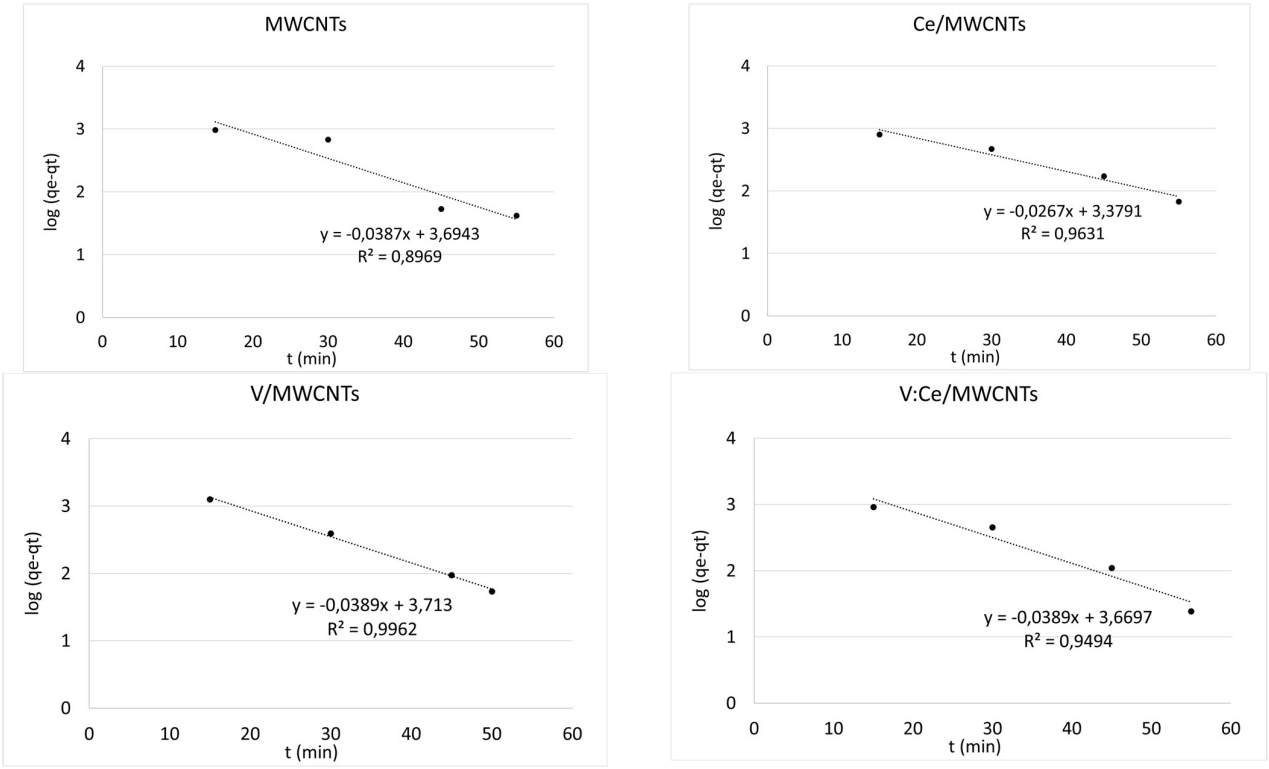

Figure 1 Pseudo-first order plot for kerosene adsorption onto metal oxide-modified MWCNTs

Appendix B

Publications related to dissertation:

1. Rasheed, R. T., Mansoor, H. S., Abdullah, T. A, Juzsakova, T., Al-Jammal, N., Salman, A. D., Rasha, R. Al-Shaikhly., Phuoc, Cuog Le., E. Domokos., Thaer, A. Abdulla. (2021). Synthesis, characterization of V_2O_5 nanoparticles and determination of catalase mimetic activity by new colorimetric method. Journal of Thermal Analysis and Calorimetry, 145(2), 297-307. **IF= 4.6.**

2. Abdullah T,A.; Juzsakova, T.; Rasheed, R.T.; Salman, A.D.; Adelikhah, M.; Le, P. C.; Igor, C. V_2O_5 nanoparticles for dyes removal from water. Chemistry Journal of Moldova, 2021, 16(2), 102-111. **IF= 1.09.**

3. Abdullah, T.A.; Juzsakova, T.; Rasheed, R.T.; Mallah, M.A.; Salman, A.D.; Cuong, L.P.; Jakab, M.; Zsirka, B.; Kułacz, K.; Sebestyén, V. V_2O_5, CeO_2 and Their MWCNTs Nanocomposites Modified for the Removal of Kerosene from Water. Nanomaterials 2022, 12, 189. https://doi.org/10.3390/nano12020189. **IF= 5.076.**

4. Abdullah T,A.; Juzsakova, T.; Mansoor, H.; , Salman, A.D.; Rasheed, R.T.; Abdulhadi, S.; Mallah, M.; Domokos, E.; Cuong, N. X.; Nadda, A. K.; Le, P. C.; Nguyen, D. D. Polyethylene over magnetite-multiwalled carbon nanotubes for kerosene removal from water. Chemosphere, 2022, 287, 132310. **IF= 7.086.**

5. Abdullah, T.A.; Juzsakova, T.; Rasheed, R.T.; Salman, A.D.; Sebestyen, V.; Domokos, E.; Sluser, B.; Cretescu, I. Polystyrene-Fe_3O_4-MWCNTs Nanocomposites for Toluene Removal from Water. Materials 2021, 14, 5503. **IF= 3.623.**

6. Abdullah T,A.; Juzsakova, T.; Le, P. C.; Kutacz. K.; , Salman, A.D.; Rasheed, R.T.; Mallah, M.; Varga, B.; Mansoor, H.; Mako, E.; Zsirka, B.; Chang, S. W.; Nguyen, D. D. Poly-NIPAM/Fe_3O_4/multiwalled carbon nanotube nanocomposites for kerosene removal from water. Environmental Pollution, 119372. https://doi.org/10.1016/j.envpol.2022.119372. **IF= 8.04.**

7. Abdullah, T. A., Juzsakova, T., Review: Functionalized multi-walled carbon nanotubes for oil spill cleanup from water. Clean Technologies and Environmental Policy, 1-23. **IF= 3.6.**

8. Al-Jammal, N., Abdullah, T. A., Juzsakova, T., Zsirka, B., Cretescu, I., Vágvölgyi, V., V. Sebestyéna., Cuong. Le Phuocd., Rashed, T. Rasheed., Domokos, E. (2020). Functionalized carbon nanotubes for hydrocarbon removal from water. Journal of Environmental Chemical Engineering, 8(2), 103570. **IF= 5.8.**